GEOPHYSICAL INVESTIGATION TO ASSESS GEOTHERMAL ENERGY POTENTIAL

SOCORRO PEAK, NEW MEXICO

Richard M. Baars

September, 2007

ABSTRACT

The Socorro Peak uplift in central New Mexico is the center of a local zone of high heat flow indicated by shallow thermal gradient wells that encountered heat flow as high as 490 mW/m^2 and temperatures of 43°C at 60 meters (m) depth. Aqueous geochemistry and mixing relationships in warm springs (32°C) suggest that high chloride concentrations at depth have temperatures of over 92°C. A variety of geochemical and geophysical studies, particularly magnetotelluric soundings and soil geochemistry profiling, have identified a drilling location in the Rio Grande basin near Wood's Tunnel on the east flank of Socorro Peak to target a >60°C geothermal reservoir at <1000 m depth. An exploration hole has been drilled to determine if a geothermal reservoir exists has sufficient temperature and capacity to provide direct use heating for the New Mexico Tech campus.

High-resolution magnetotelluric traverses, conducted at a 100-m station spacing, were employed to characterize the distribution of resistivity across the range bounding fault on the east side of the Socorro Peak uplift. One and two dimensional inversions of the data show a steeply dipping range-bounding fault juxtaposing resistive footwall Precambrian and Paleozoic rocks and Tertiary volcaniclastics against conductive hanging wall fanglomerates. Within the hangingwall block, the MT profile data identify a 400-m-thick aquitard that separates shallow aquifers from deeper target thermal waters. Other geophysical surveys were conducted to confirm the results of the magnetotellurics survey. Gravity data was modeled to verify Socorro Canyon fault characteristics. Additionally, a pilot study of remote sensed ASTER thermal images suggests that the Socorro Peak thermal feature can be identified from space. Further work with these images must be done to validate the detection of the thermal feature.

A choice of drilling target was based on a synthesis of thermal gradient data, the geophysical and geochemical information (Owens, 2007), geologic structure, hydrologic models, and economic factors. The slimhole well was drilled on the Wood's Tunnel mine portal pad west of the Socorro Canyon fault near the area of highest measured heat flow, and near the intersection of the Socorro caldera fracture system, a transverse shear zone, and the Rio Grande rift bounding fault, and close to the New Mexico Tech campus. Fluid leakage up or across the range front fault system is a likely host for deep >65°C thermal waters. The borehole will penetrate both the faulted structural conduit as well as permeable sediments below the aquitard within the hanging wall block to evaluate multiple hypotheses for the source of the heat flow anomaly.

TABLE OF CONTENTS

Page

LIST OF FIGURES

LIST OF FIGURES

This Thesis is accepted on behalf of the faculty
of the Institute by the following committee:

Academic Adviser

Research Advisor

David I. Norman

Committee Member

Committee Member

Committee Member

8-5-07

Date

I release this document to New Mexico Institute of Mining and Technology

8-5-07

Students Signature

Date

INTRODUCTION

The Socorro geothermal area is located in central New Mexico, within the Rio Grande Rift (Figure 1.). The geothermal area has been of interest for many years; the presence of the Socorro Warm Springs provided the original evidence of a localized geothermal heat system in the Socorro, New Mexico, area. Prior research has been conducted in an attempt to evaluate geothermal potential in the Socorro, region. The localized geothermal area has been defined by a series of shallow, temperature-gradient drill holes around the Socorro Peak mountain block (Reiter and Smith, 1977; Sanford, 1977; Reiter, 1986). Temperature-gradient measurements in the Socorro Peak mountain block were found to be considerably higher than basin-gradient temperatures (Barroll and Reiter, 1989; Reiter and Smith, 1977; Sanford, 1977) with heat-flow measurements as high as 490 milliWatts per meter squared (mW/m^2) located in the Wood's Tunnel temperature-gradient hole. The basin heat-flow values to the west of Socorro Peak in the La Jencia Basin range from 34–62 mW/m^2 with an average heat-flow value of approximately 45 mW/m^2. The Rio Grande Basin to the east of Socorro Peak in the Rio Grande rift has heat-flow values ranging from 75–100 mW/m^2 with an average heat-flow value of 95 mW/m^2 (Barroll 1990). The Socorro Peak geothermal area exhibits considerably higher heat-flow values than both the Rio Grande and La Jencia basins providing a geothermal exploration target at Socorro Peak.

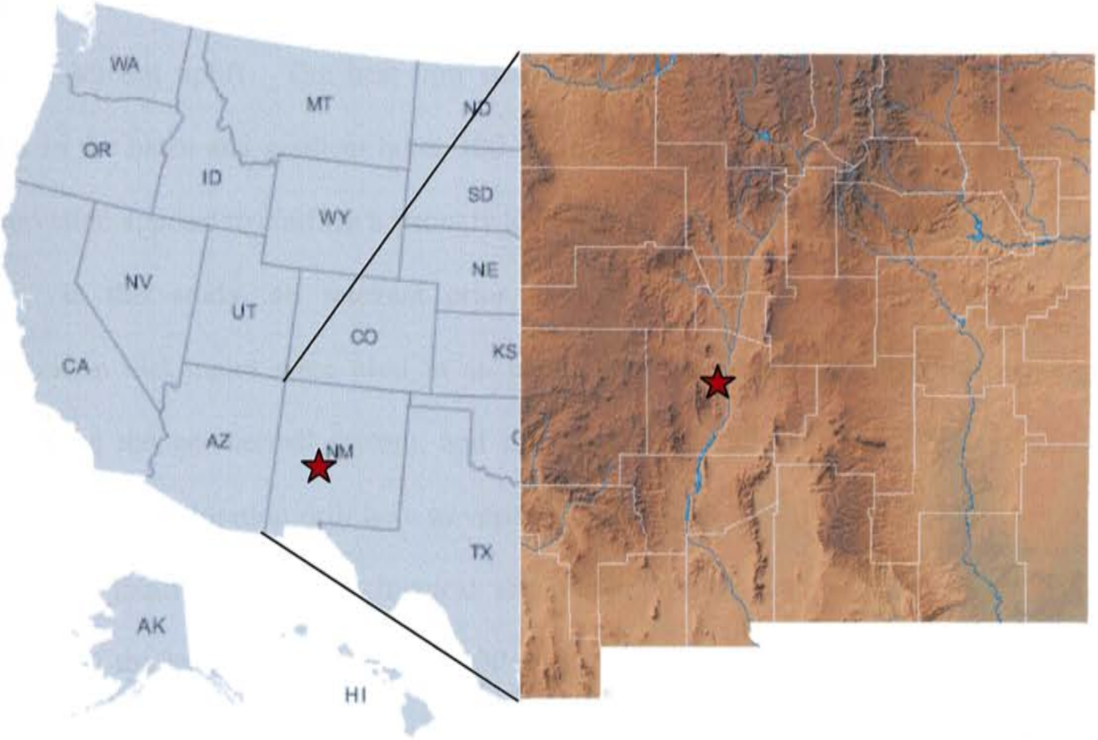

Figure 1. Location Map of Socorro, New Mexico.

Prior work has been done to attempt to identify and understand the interaction among the ground water sources of this geothermal system with respect to the hydrology of Socorro warm springs (Chamberlin, 1999). Work by multiple parties (Chamberlin, 1999; Barroll, 1989) concluded that a complex geothermal system exists. Deep circulating recharge originating in the La Jencia Basin is speculated to be heated within the deep crust; from there, it is then forced through the Socorro Peak mountain block, heating the mountain block by a combination of advection and conduction. The exact transport mechanism for the thermal fluids is not known, but is speculated to be a combination of fault and fracture permeability through the Socorro Peak basement rock material. Thermal anomalies are very localized and adjacent to or within the Socorro Peak basement uplift. The heat-flow data show significant change between gradient holes in the basin and gradient holes 100 m to 150 m away in the mountain block; this observation appears to confirm a strongly localized thermal regime (Barroll, 1989).

In this study, all relevant prior work was compiled and new geophysical exploration techniques were used in an attempt to characterize the geologic structure controlling the geothermal system, and also to inform a decision on where to drill a 1000-m-deep exploration drill hole to verify geothermal fluids at depth. This study was conducted jointly with a geochemical exploration project with similar objectives of identifying the best location for the 1000-m-deep exploration drill hole (Owens, 2007). New data will also be collected to compliment existing work, magnetotellurics, surface magnetics, gravity compilation, and thermal imagery.

New software (WinGLink®) to analyze existing data and to process the new magnetotelluric (MT) data was used to establish a more detailed conceptual subsurface model on the Rio Grande side of Socorro Peak. The MT data provide a more complete image of the subsurface and assist in further understanding of the subsurface geometry and lithology. The MT data provide subsurface evidence that there were no apparent step-down-style fault blocks within the upper kilometer (km) of the subsurface, no clay alteration confining areas, and largely confirm the existing geologic model using resistivity to provide an image of the lithologic strata at depth.

PRIOR WORK: SOCORRO GEOTHERMAL SYSTEM

Multiple studies have been conducted in this area with application to the geothermal problem. Modeling and temperature log analysis studies were conducted by Barroll (1989). Barroll's work synthesized previous work conducted by Sanford (1977) and Reiter and Smith (1977), both presenting temperature logs from industry temperature drill holes as well as holes drilled and measured during individual studies. High temperature gradients were calculated in thermal profile holes drilled along the east side of the Socorro Peak mountain block. Reiter and Smith (1977) drilled a gradient hole in the rear of Wood's Tunnel Mine, collared 128 m below land surface and then drilled and extended to a total depth of 195 m below land surface (Figures 2 and 3.). Thermal conductivity was measured on core samples and the heat-flow value of 490 mW/m^2 was calculated from the borehole temperature gradient, identifying a very localized zone of extremely elevated heat flow in the Socorro Peak mountain block. Sanford (1977) identified other areas of elevated heat flows in the Blue Canyon area and presented other temperature gradients surrounding the Socorro Peak mountain block. Both Sanford (1977) and Reiter and Smith (1977) appear to agree that the elevated heat flow was located in material within or immediately adjacent to the Socorro Peak mountain block. Barroll (1989), in accordance with Reiter and Smith (1977), and Sanford (1977)

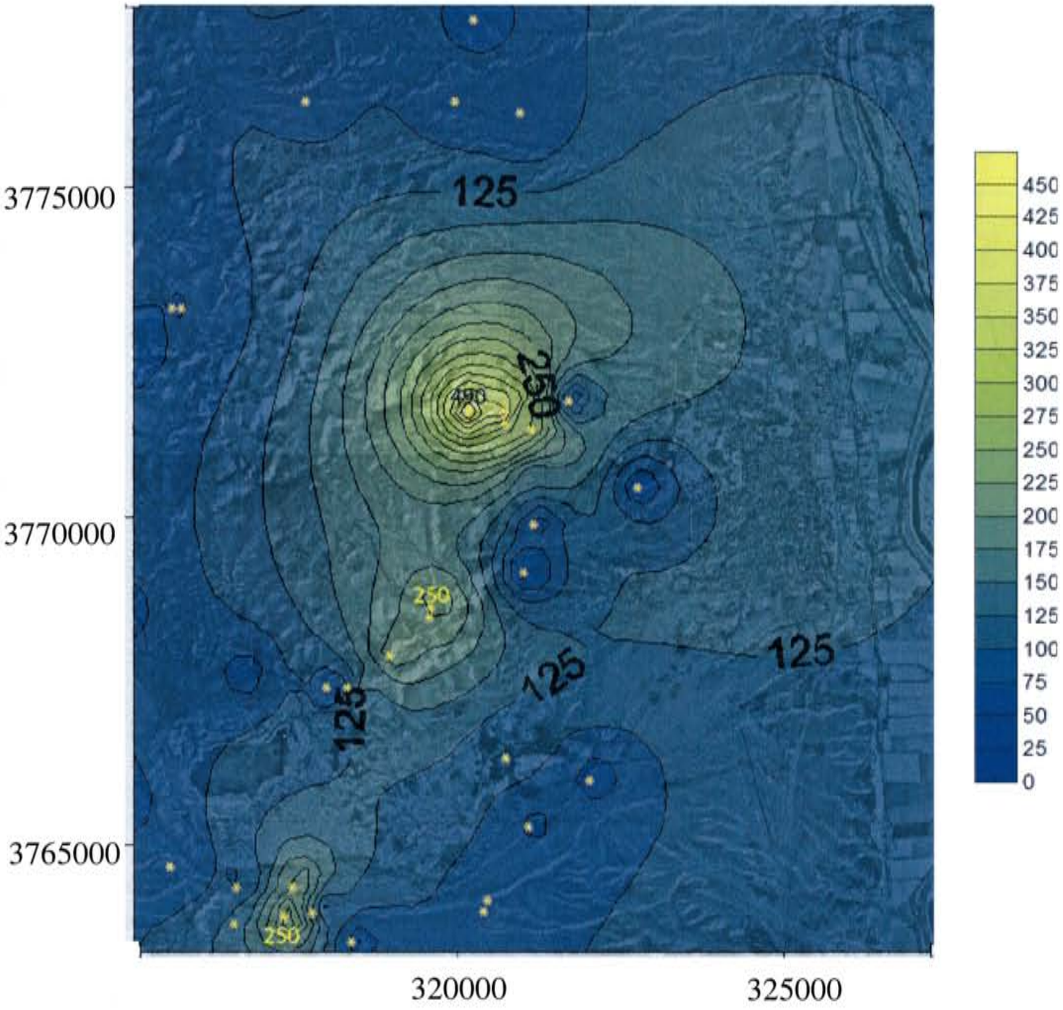

Figure 2. Heat flow contour map, data from Barroll and Reiter (1989). Wood's Tunnel has highest heat flow of 490 mW/m^2 with other heat flow wells marked with yellow star. Units in meters.

concur that the thermal gradients within the basins on either side of Socorro Peak are much lower (approximately 20°C–60°C per kilometer), due to shallow groundwater flow from north to south which masks the signature in both basins.

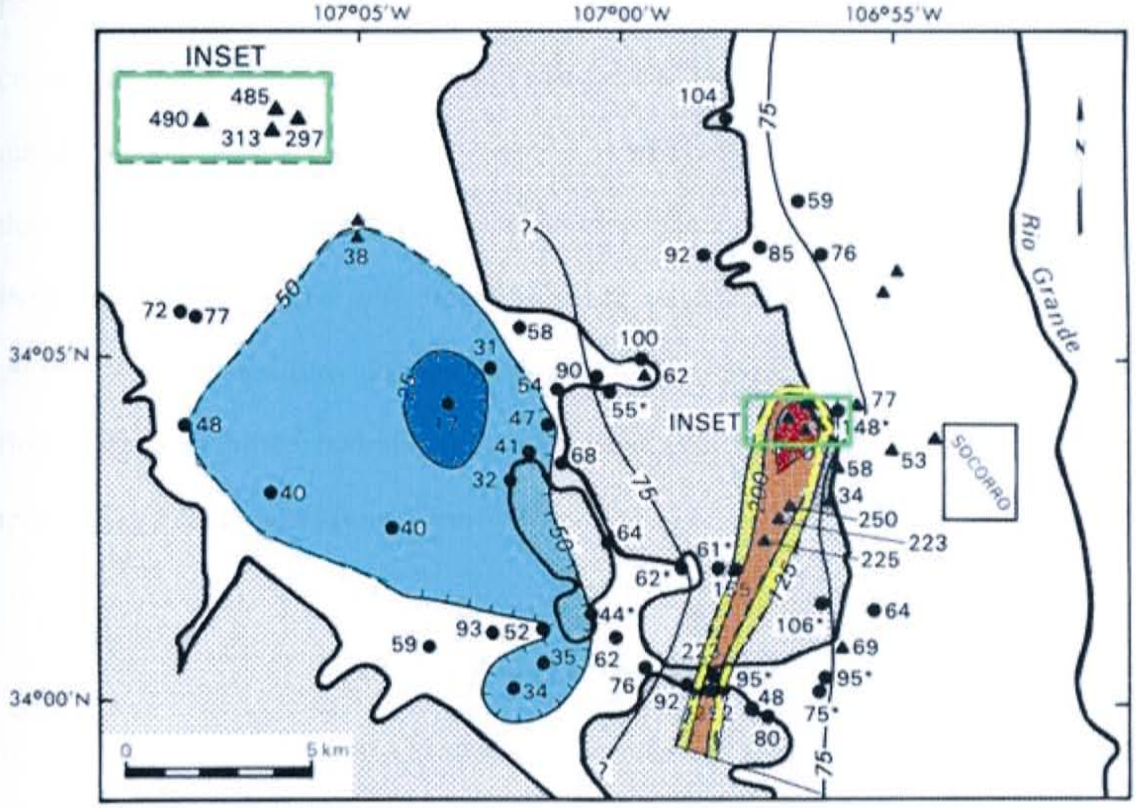

Figure 3. Heat flow contour map modified from Barroll and Reiter (1990). Heat flow is given in mW/m^2. Note magnified inset of Wood's Tunnel area.

Barroll (1989) and Reiter and Smith (1977) suggest the possibility that groundwater flow through the Socorro Peak mountain block is responsible for advection of heat creating both a concentrated heat flow in some areas (mountain block) and suppressing heat flow in other areas such as the basin.

Barroll (1990) building on prior work, performed a series of finite-difference fluid and heat advection models. Barroll modeled hydraulic head and constrained the models with heat balance parameters. Barroll concluded that heat does not appear to originate from an anomalous source in the subsurface (such as magma body), but from deep, circulating fluids swept down deep in the La Jencia Basin trapped under thick claystone materials and heated at depth. Once heated it is advectively circulated and forced to rise through the fractured Precambrian and volcanic mountain block material of Socorro Peak. Barroll concluded with finite-difference models that the combination of deep circulating fluids and flow through basement strata produce reasonable models of heat flow with appropriate hydrologic barriers conducting heated fluids to the surface relatively matching flows from Socorro Warm Springs.

Geology and Hydrogeology

The geology of Socorro Peak and the surrounding area of interest is complex both stratigraphically and structurally (Figure 4.). The area of Socorro Peak has experienced multiple volcanic intrusions and cauldron collapses of the Oligocene Datil-Mogollon volcanic field, later followed by uplift, rifting, and filling of the Rio Grande Basin (Chamberlin, 1999). The basic lithology of the rift valley is a sequence of Quaternary sediments deposited as uplift and rifting occurred in the Socorro area intermixed with seven or more episodes of magmatism associated with the Datil-Mogollon volcanic field.

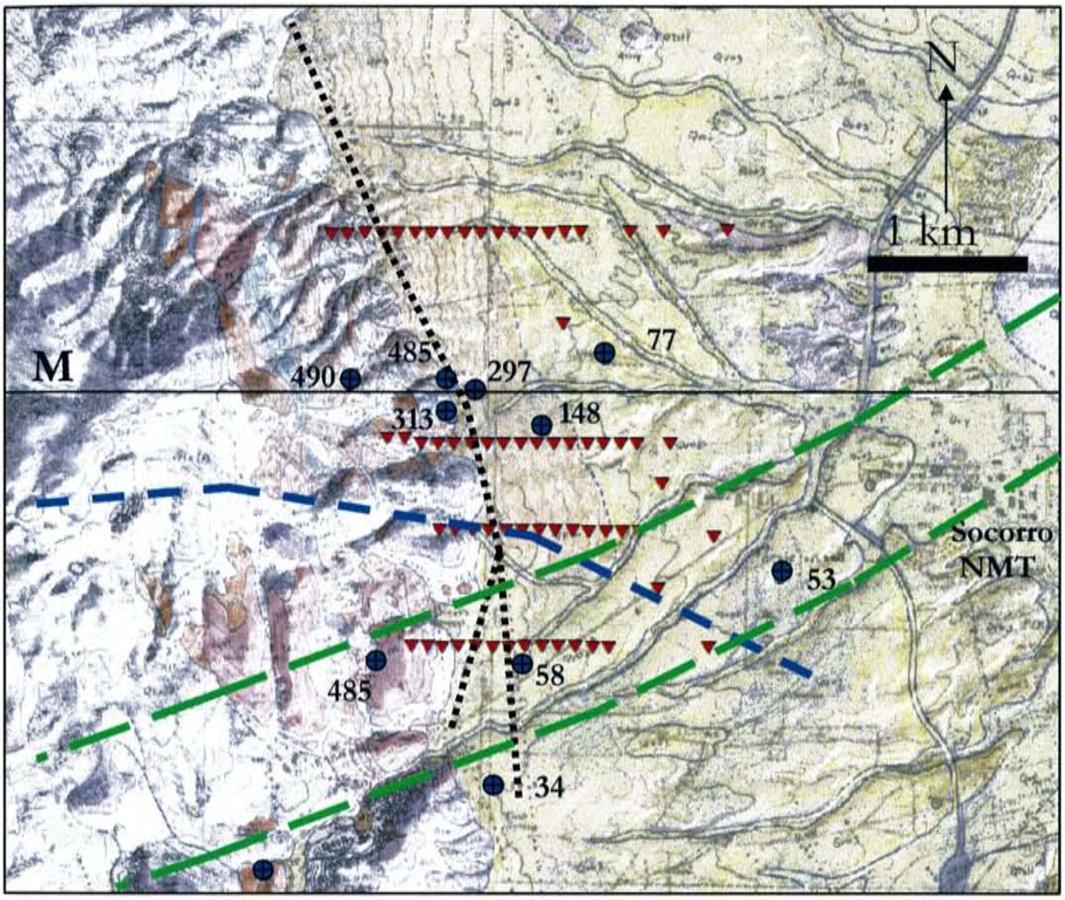

Figure 4. Major structural features of the Socorro Peak Complex: the blue dashed line is the approximate structural location of the Socorro cauldron boundary, the finer dashed line is the range bounding fault, and the large green dashed line is the approximate location of the transverse shear zone (Chapin, 1979). Blue circles represent thermal gradient wells with corresponding heat flow value (mW/m^2), red triangles represent station locations for MT profiles. Geologic map adapted from Chamberlin, 1999.

The lithology of the Socorro Peak is heterogeneous due to multiple magmatic events and episodes of rifting, tilting, uplift, and erosion. However, the lithology can be broken down into a simplified stratigraphic series. For a more detailed description of rock type and lithology, see Chamberlin et al. (1999) and Chapin (1978).

The oldest lithologic member is the Precambrian and Paleozoic mountain block. The Precambrian rocks consist of mostly igneous and metamorphic rock microcrystalline arkosic quartzite that is exposed on Socorro Peak due to more than 1000 m of offset on the Socorro Canyon fault on the west side of the Rio Grande Rift. The Paleozoic rocks consist of resistant limestones, sandstones, and shales of Mississippian and Pennsylvanian age. The Precambrian and Paleozoic formations have little to no matrix permeability but may have extensive fracture permeability (Personal communication with R. Chamberlin, 2006). These units compose the majority of the Socorro mountain block and underlying material.

Above the Precambrian and Paleozoic mountain block is a complex series of early-Tertiary volcanics consisting of ash-flow tuffs, andesite, basaltic-andesite lavas, landslide deposits, rhyolitic domes, and conglomerates associated with multiple eruptions in the Datil-Mogollon volcanic field (Chapin et al. 1978). The thickness and lateral extent of the volcanics is extremely variable but Chamberlin et al. (2004) speculate that they may be as much as 3000 m thick near the eruptive centers. The Tertiary volcanics range considerably in type as well as location.

Above the Tertiary volcanics is the Lower Popotosa formation, a well indurated silicified conglomerate. The Lower Popotosa is described (Chamberlin, 1999) as being composed of mudflow deposits, fanglomerates, and lacuastrine siltstone and mudstones. The Lower Popotosa can range in thickness from 600 m to 2000 m. It is capped by the thick Upper Popotosa clay playa and underlain by several packages of volcanic tuffs, andesites, and ash flow tuff materials. The Lower Popotosa is a target for drilling as it is a brittle conglomerate.

The playa lake and Popotosa basin deposition were, however, interrupted on multiple occasions; resurgent volcanism intruded into the area once again with the uplift of domes. It was during this time that ancient geothermal systems were speculated to be at their peak (Barroll, 1979 and Chapin, 1978) based on rock geochemistry of the Lower Popotosa. By the late Tertiary, the Popotosa Basin was then stretched and uplifted by block faulting, with Socorro Peak and the Lemitar mountains rising from the middle of the basin as an intra-graben horst block exposing Precambrian rock, with sediments eroding into the basins, thickening the playa deposits, and creating a thick, clay hydrologic boundary that significantly affected the flow of the modern hydrologic system.

Above the lower Popotosa is a Tertiary clay-rich playa deposit (Upper Popotosa) which is thought to be the primary aquitard for the Socorro geothermal system (Chapin et al. 1978). The Upper Popotosa is described as a gypsiferous playa claystone and mudstone with interbedded basalt flows (Chapin et al. 1978). This formation is largely buried by landslide and colluvium deposits. The Upper Popotosa ranges in thickness and lateral extent as it is mixed with Quaternary fanglomerates. The clay playa Popotosa ranges in thickness from 200 m to 1000 m. During the early Tertiary, the Socorro

Cauldron and the Datil-Mogollon volcanic field produced voluminous volcanic ash. Upon the completion of volcanism, large cauldron drop-down structures were filled with thick layers of volcanic material, while outside of the cauldron boundaries, volcanic deposits are relatively thin in comparison. During the Miocene, cauldron volcanism subsided and a large sedimentary basin formed in the area with the deepest part of the basin located near Socorro Peak. The Upper Popotosa thins from north to south in the Rio Grande rift basin as seen in deposits in the northern Lemitar Mountains to the Chupadera Mountains to the south.

Above the Upper Popotosa is the youngest unit, a series of Quaternary valley fill alluvial deposits including alluvial fans, piedmont slopes, terraces, colluvium, playa, landslide, and fluvial materials. These deposits range greatly in thickness from meters to hundreds of meters. These upper Quaternary materials may also be interbedded with basalt flows to the south of Socorro Peak associated with the Sedillo Hill basalt flows—the last event of volcanism within this area.

Socorro Peak is structurally complicated as well; the Socorro Cauldron, a nearly circular 20-km-diameter structure, is located adjacent to the steep cliff-forming outcrops of the Popotosa conglomerate just slightly south of the main peak. The cauldron is a key structural feature in the area and is a considerable source for the majority of the magmatic material. The Socorro Cauldron is the farthest northeast extent of the Datil-Mogollon volcanic field. Multiple episodes of volcanism in the area have transformed the skyline as silicic domes and flows form the major topographic features of Socorro Peak. Rhyolitic and rhyodacitic domes and flows blanket thick playa deposits in the area to the north and west. The most recent volcanic events consist of venting and ruptures of basalt flows emplaced from west to east around the current Grefco Perlite Mine at 5.3 million years (Chamberlin, 1999).

Socorro Peak has another key structural feature that complicates the mountain block as well. The Morenci lineament is a transverse shear zone trending northeast-southwest intersecting the peak near the cauldron margin. This shear zone is a key accommodation zone between two trends of rotating fault blocks and faulting for the Rio Grande Rift zone. To the north, the dip of the Lemitar Mountains is to the west and down-faulted to the east. To the south of the shear zone, the Chupadera Mountain blocks are dipping to the east and down-faulted to the west (Chapin et al. 1978). This reversal in dip direction can only be accomplished with considerable fracturing and faulting of the near-surface brittle mountain blocks, and extensive fracturing and faulting of the Precambrian and Paleozoic basement materials in a zone approximately 1.5 km wide. Coincidentally, this transverse shear zone intersects Socorro Peak and the Socorro Cauldron margin in approximately the same location on Socorro Peak. This intersection area has two naturally flowing warm springs (Socorro and Sedillo) and one man-made spring (Cook) issuing from the base of the mountain (Hall, 1963; White, 1992). It is suggested by Chapin et al. (1978) that the shear zone and the Socorro Cauldron intersection provide an area of fracture permeability for the flow of springs and possible geothermal waters. The Morenci lineament also appears to be a major control on magmatism in the area. The Datil-Mogollon volcanic field and its seven, eastern, overlapping and nested cauldron margins, and multiple domes and flows lie directly on the lineament or directly adjacent to the structure (Chapin et al. 1978).

The hydrogeology of the area is equally complicated as is the geology. Socorro is located in the semi-arid southwestern United States only receiving 15 to 25 centimeters (cm) of precipitation per year. The majority of this precipitation comes from late-summer thunderstorms. However, the Magdalena Mountains receive an order of magnitude more precipitation and act as the primary source for groundwater recharge in this area (Anderholm, 1987). The hydrologic flow has been studied by multiple researchers for various reasons, and all have reached similar conclusions (Barroll, 1989; Mailloux, 1999; Gross and Wilcox, 1983) (see Figures 5 and 6).

The basic flow direction of the La Jencia Basin is from west to east with 80%–95% of recharge being focused within the Magdalena Mountains and roughly 5%–20% of recharge occurring in the Lemitar Mountains and Socorro Peak (Mailloux et al. 1999). Flow direction in the Rio Grande Basin is, however, from north to south. The interaction between geology and heat input play a significant part in the resultant effluence from Socorro Springs. Multiple hydrologic models indicate recharge in the Magdalena

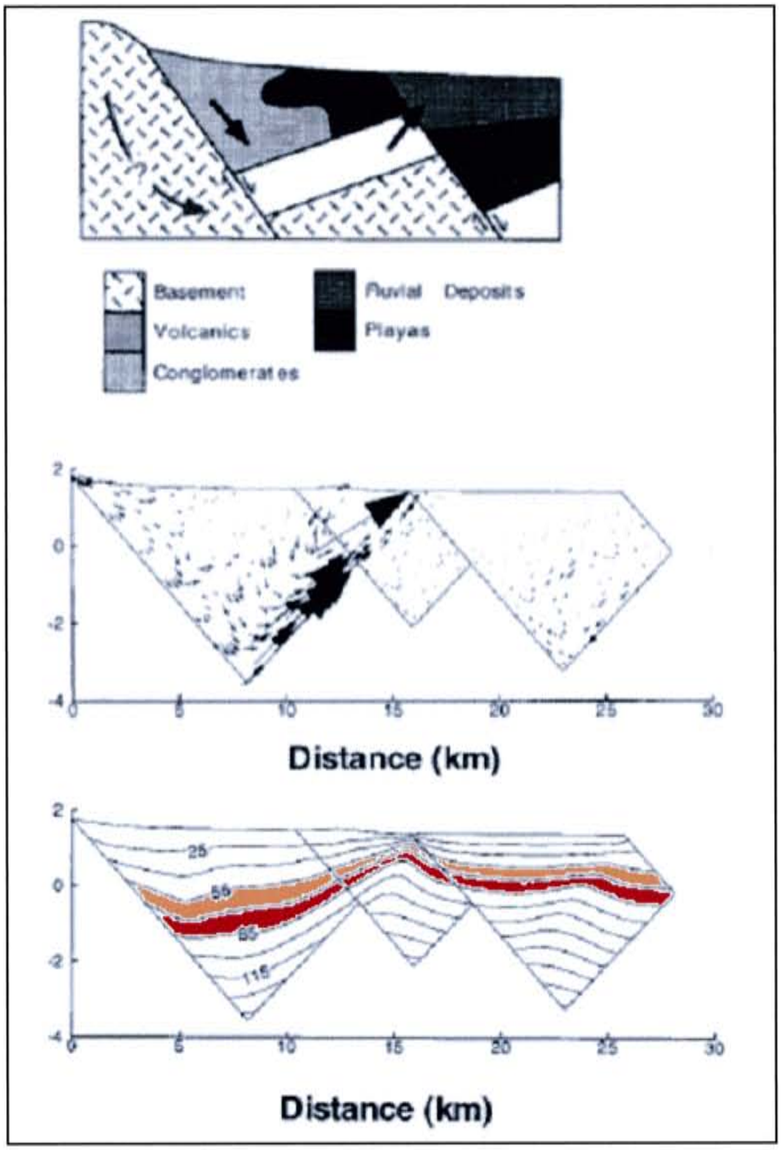

Figure 5. Conceptual flow and model results from Mailloux et al. (1999). Top panel represents recharge of water at Magdelena mountain front, flow through deep basin and basement near-surface, and discharge zone at Socorro peak area. This model represents the north flank of the Socorro geothermal target area. Middle panel is cross sectional flow velocity from model result, which matches surface heat flow, showing large basement and fractured rock flows coming to the surface in the warm springs and surrounding geothermal target area. Bottom panel shows isotherms from model results.

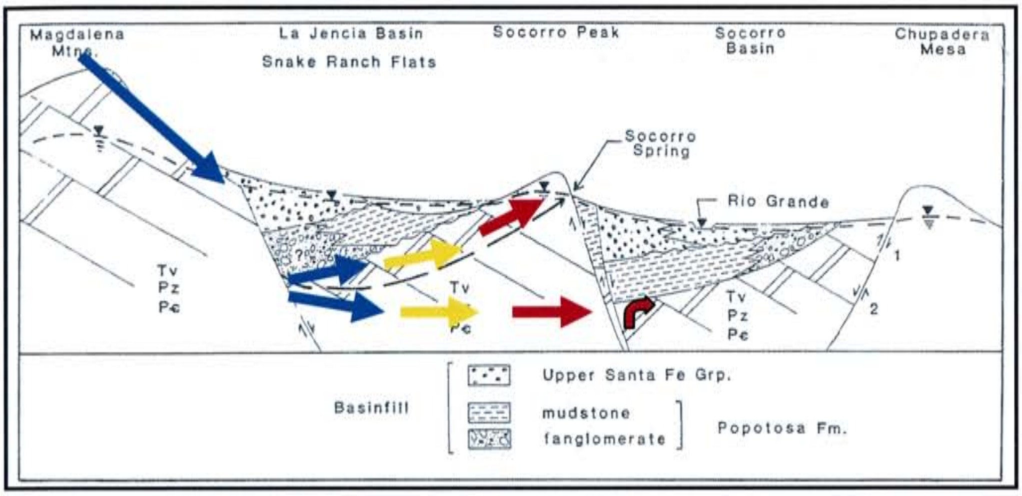

Figure 6. Conceptual hydrologic model adapted from Gross and Wilcox (1983). Recharge shown with large blue arrow located in the Magdalena Mountains with deep flow and heating occurring through Socorro Peak mountain block.

Mountains with meteoric waters penetrating the permeable sediments and traveling to depth within the La Jencia Basin. The depth of this traveling water is, however, not precisely constrained, as most wells in the La Jencia Basin only penetrate up to an average of 100 m for irrigation and livestock purposes. Once in the subsurface alluvium, the meteoric fluids may become trapped under several confining geologic barriers, primarily the Popotosa playa deposits and claystones, and are forced to flow to depth through the conglomerates, volcanic tuffs, and fractured basement material. Once at depth, the waters are heated through interaction with the bedrock, and forced to rise to the surface beneath Socorro Peak through fracture permeability. Once heated, the deep circulated fluids mix with fresh meteoric fluids by 5%–20% of total spring flow and issue from exposed volcaniclastic sediments intermixed with Popotosa Playa deposits (Gross and Wilcox, 1983; Barroll and Reiter, 1989). It is speculated by Barroll and Reiter (1989) and Gross and Wilcox (1983) that the ascending heated spring water is forced to flow between two juxtaposed playa deposits through significant fracture permeability in the Lower Popotosa formation. However, the majority of the recharge from the Magdalena Mountains does not flow from Socorro Springs but is unaccounted for at depth.

Initial Hydrothermal Conceptual Model

The heat flow in and around Socorro Peak and the adjacent La Jencia Basin and Rio Grande Basin has been studied by many of the same workers, and a more in-depth description of heat flow data can be found in work by Barroll and Reiter (1989), Sanford (1977). The combination of the heat-flow data, geologic mapping and interpretation, and hydrologic modeling suggest an initial, conceptual geothermal model of this area. Heat-flow data were collected over the majority of the Socorro Peak area and consist of roughly 63 temperature gradient wells varying in depth from 60 m to 610 m with an average depth of approximately 180 m (Figure 3.). (Barroll and Reiter, 1989; Sanford, 1977; Reiter and Smith, 1977). Heat-flow calculations were made from the temperature-gradient holes as well as temperature conductivity measurements and some observations were published by Barroll and Reiter (1989).

Thermal gradient data in La Jencia Basin show relatively low background gradients. Heat-flow values were lower than expected (recharge blocks heat from being transported to the surface, or that some flow system below the Popotosa claystone was masking heat flow to the surface. The exact reason for the lower-than-normal heat-flow values is not known but hypothesized by Barroll and Reiter (1989) to be a combination of the recharge and the deep flowing aquifers trapped below the Popotosa claystone.

Review of the thermal-gradient data highlighted a second area of interest: the Socorro Peak mountain block. Heat-flow data indicate that Socorro Peak, and specifically the Socorro Peak mountain block and Blue Canyon, has a very localized and elevated temperature gradient associated with shallower volcanics and outcropping aquifer units of the Lower Popotosa (Figure 4.). This localized gradient is restricted to the Socorro Peak mountain block, as elevated heat-flow is not observed in either the La Jencia Basin or the Rio Grande Basin. Heat-flow data near the city of Socorro appears to have normal values for the Rio Grande Rift (approximately 75–90 mW/m^2) right up to the range bounding Socorro Canyon fault on average, less than 50 mW/m^2) in that the area (Figures 2 and 3.), indicating that water, where the heat-flow values increase significantly (approximately 100–490 mW/m^2), with the Wood's Tunnels heat-flow value of 490 mW/m^2 being the highest value observed. Other nearby wells also exhibited heat flow several times greater than Rio Grande Rift values. The Wood's Tunnel temperature-gradient hole was drilled into fractured Precambrian rock. The total distance between the highest observed heat flow values at Wood's Tunnel and the lowest in La Jencia Basin is less than 10 km and less than a few kilometers from average Rio Grande heat flow values, indicating a relatively localized heat source in the upper crust.

The initial hydrothermal model therefore indicates a complex system with recharge from the La Jencia Basin traveling to depth and becoming trapped under Upper Popotosa claystone, until it reaches depths where it is heated and advectively rises through Tertiary volcanics and Lower Popotosa conglomerates through fracture permeability beneath the Socorro Peak. Some thermal fluids then mix with meteoric fluids and issue from the Socorro Springs at the surface.

Past Geophysical Studies

Several geophysical studies have been conducted on the Rio Grande rift and adjacent areas. These studies range from deep seismic reflection work performed by COCORP in the late 1970s (Brown, 1980) to detailed gravity studies used to infer basin fill depth and shape (Keller, 1983), with further work using MT transects crossing the region in attempts to define basin features. Several more studies have been conducted in this region using geophysical techniques to provide basin geometry and properties (New Mexico Geological Society Field Guide, 1983); however, none of these studies were targeted at exploring the geothermal potential or located near Socorro and the surrounding area. Highlights of the pertinent studies will be presented as background information with new work added appropriately.

CURRENT WORK: RESULTS

Gravity

The Socorro area and adjacent La Jencia Basin currently have a database of over 600 Bouguer-corrected gravity stations collected by A. Sanford (Figures 7 and 8.). The most current gravity data set was provided by A. Sanford (personal communication, 2005) with additional stations added after the publication of Sanford (1968), and is included as Appendix C. The gravity data set published by R. Anderson (1953) is based on a subset of the entire data set and uses curve fitting to approximate a basin depth in the Rio Grande Valley. Work later conducted by Sanford (1968) showed curve-fitting models for cross sections from the La Jencia Basin through Socorro Peak and into the Rio Grande Basin. He concluded that Basin-and–Range, horst-and-graben style of faulting and basin structure match relative values observed in the processed gravity data.

The gravity data were entered into a spreadsheet; their location coordinates were then converted to NAD 1927 UTM Coordinates from latitude and longitude, so that various mapping and modeling programs such as ArcGIS and WinGLink® could be used. WinGLink® is a geophysical modeling and mapping program which was primarily used to process and invert the MT data (see next section). WinGLink®, in addition to the MT package, has a gravity-forward modeling and processing module used to process the primary area of interest for the sake of this exploration project. A cross section of gravity

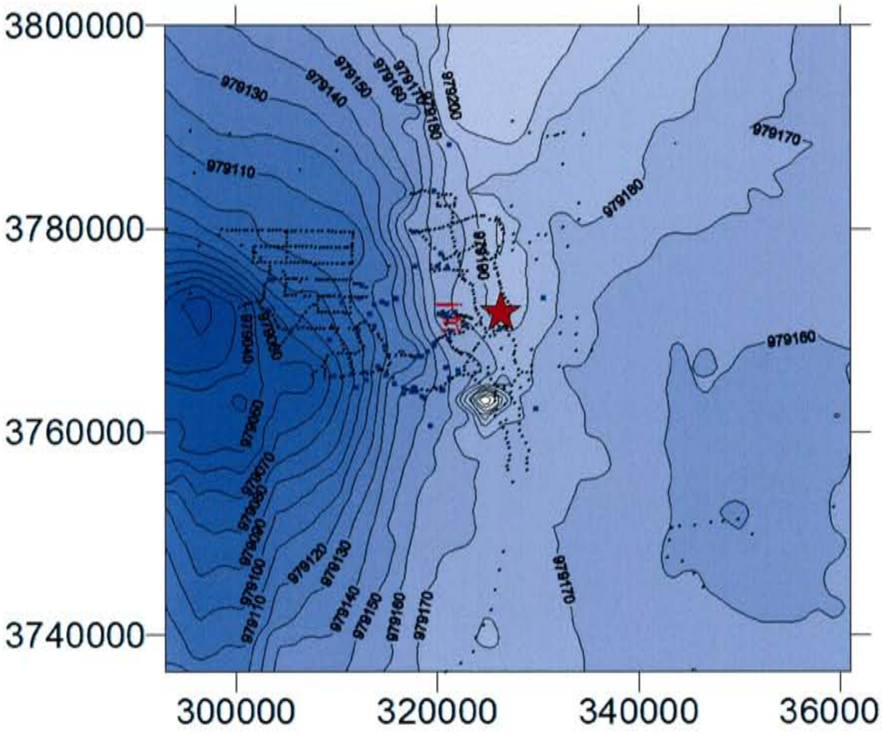

Figure 7. Gravity station map from all compiled data (black dots) (Sanford, 1968; A. Sanford, personal communication). Contours of observed gravity readings. Darker colors represent gravity lows and lighter colors represent observed gravity highs. Red triangles represent stations on MT profile lines. Socorro, NM represented by star. UTM coordinates unit meters.

data was taken in the area of Wood's Tunnel and, more specifically, along Magnetotelluric Line #2. Using the observed gravity data supplied by Sanford, a much more detailed forward model could be constructed using the most current geological data (Figure 9.) and the processed MT data to create a realistic forward model. Density values were taken from

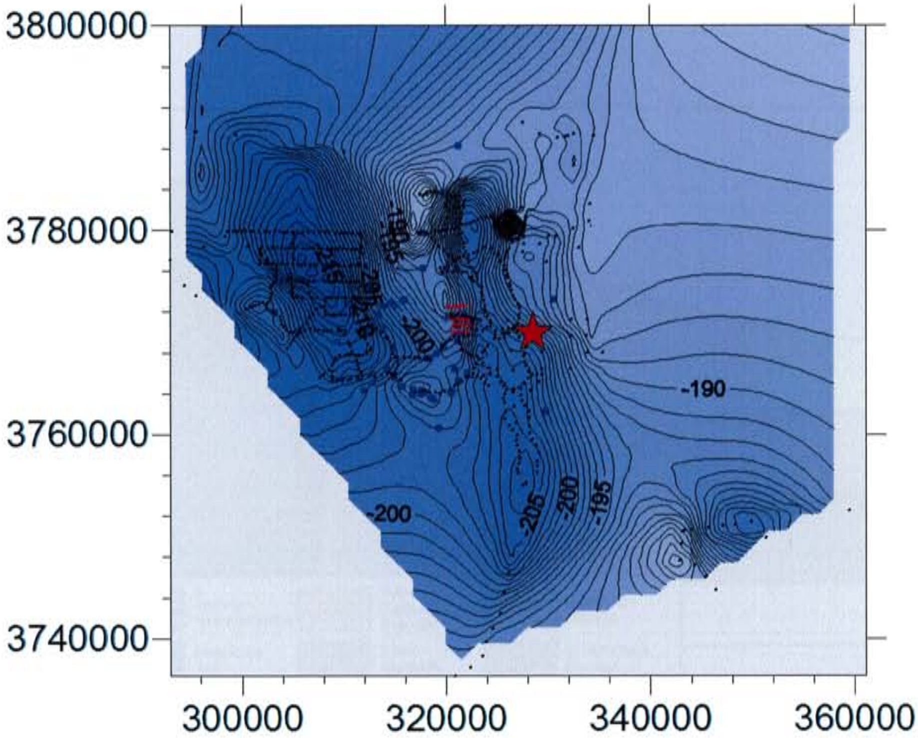

Figure 8. Bouguer anomaly contour map with symbols as in Figure 7. UTM coordinates unit meters.

Sanford, (1968). Sanford sampled the geologic column throughout the area. Where rock types were not detailed in Sanford's data, an average rock density was used (Telford et al. 1990).

The method of forward modeling the gravity data with the knowledge of the MT data and detailed geologic cross sections (Chamberlin, 1989) allowed for a relatively detailed model. Using resistivity and estimating rock types, a reasonable model of the

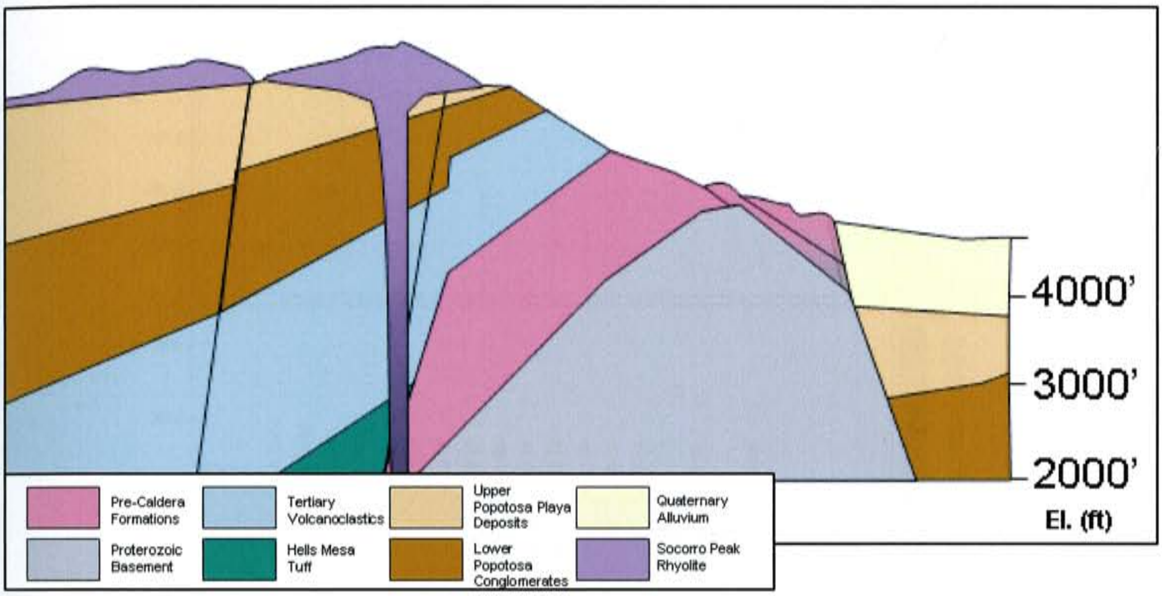

Figure 9. Geologic cross section through Wood's Tunnel area and MT profile 2. Simplified cross section from Chamberlin (1999).

subsurface could be constructed based on measured rock densities where possible, and average densities when needed. The simplified forward model can be seen below (Figure 10.) with the generalized geologic cross section and the MT data.

Results of the forward models show a reasonable fit to the data. The use of the MT sections and the geologic cross sections allow for a relatively accurate means of placing boundaries for geologic units as well as structural features such as the Socorro Canyon fault. The results of the forward models suggest that the geologic cross sections

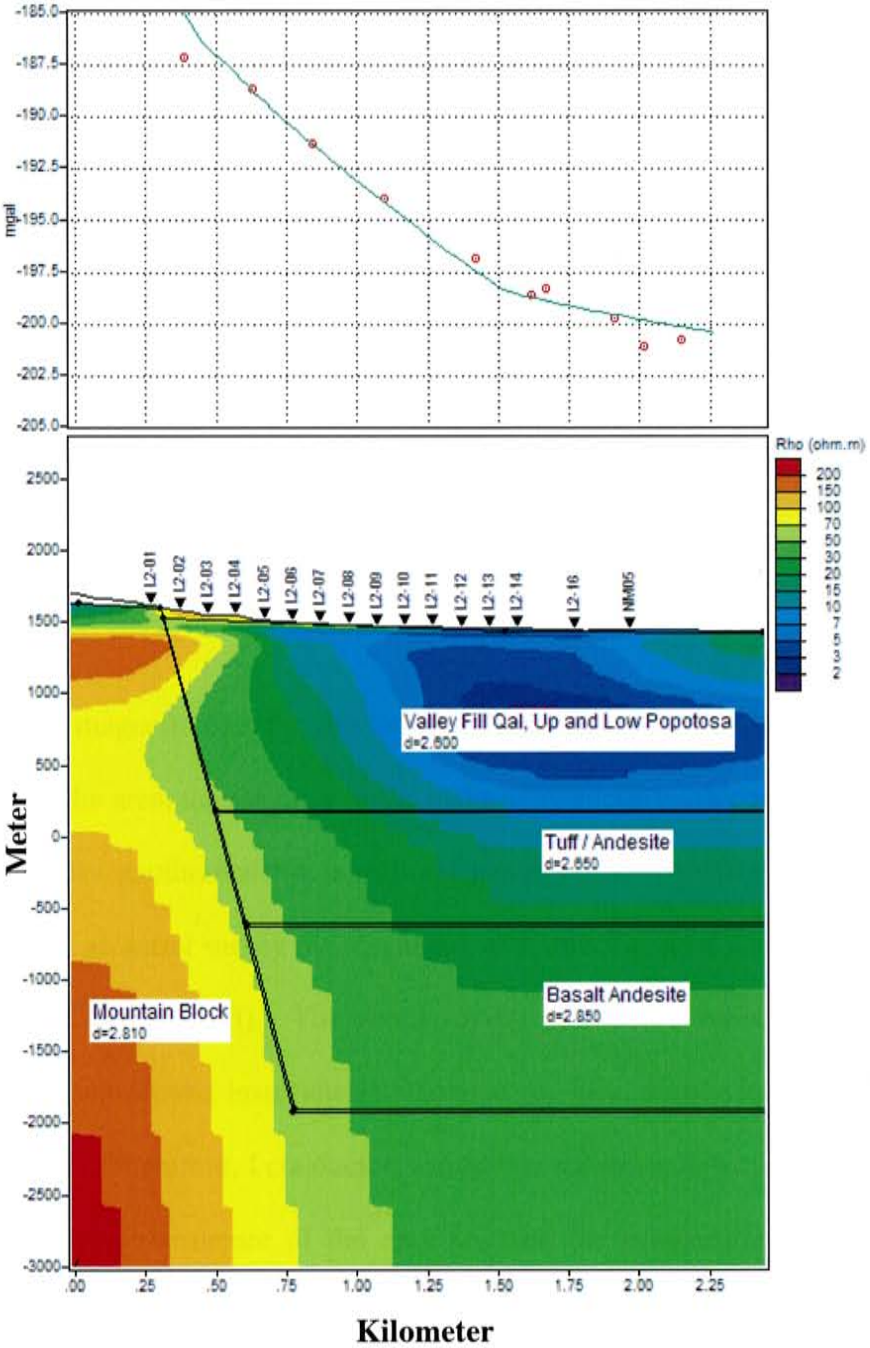

Figure 10. Simplified forward model of gravity along MT profile 2. Colored contours are the MT 2D resistivity profile with gravity results and curve fit above for Bouguer anomaly values. Density in grams*cm^{-3}.

of the Socorro Peak area are consistent with observed gravity data, which do not show any anomalies or unsuspected subsurface features such as buried down faulted high-density basement blocks.

Magnetic Field Data

Magnetic data were collected over the geothermal target area west of the town of Socorro and adjacent to Socorro Peak. The magnetic survey was conducted along the eastern flank of Socorro Peak and extended out onto the alluvial fans towards the east (Figure 11.).

Detailed magnetic data for the Socorro Peak region is very limited. Unlike the gravity data for the area, the majority of the historic magnetic work conducted was during the exploration for geothermal fluids, oil and gas in the late 1970s to the 1980s. This specific area had an aerial survey for magnetics with minor ground surveys conducted for other reasons (Cordell, 1983). The aerial survey provided a basis for understanding regional trends, but proved insufficiently detailed for local geophysical characterization of the subsurface. Therefore, I conducted a magnetic survey in an attempt to shed further light on the geologic structure of the area targeted for geothermal exploration. The purpose of the magnetic survey was initially to locate the buried Socorro Canyon fault as

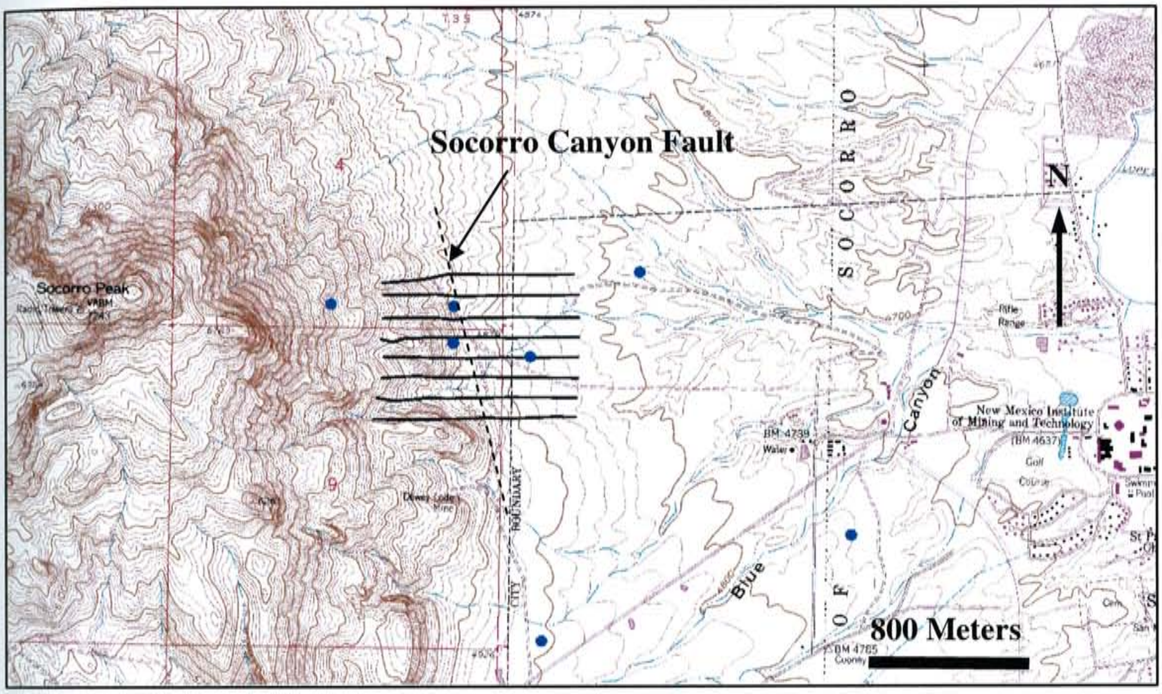

Figure 11. Location of magnetic traverses overlain on the Socorro quadrangle map. Blue dots represent thermal gradient wells with Woods Tunnel well to the farthest left.

precisely as possible for mapping and later decision making for drilling purposes. With the use of a Cesium vapor magnetometer (Geometrics G-858) and a hand-held global positioning system (GPS), profiles were acquired perpendicular to the buried Socorro Canyon fault (Figure 11.). The initial results of a magnetic reconnaissance survey showed that the Socorro Canyon fault did not yield any obvious anomalies, so more detailed mapping of the geothermal target area was undertaken. Through a series of several transects, a drift-corrected magnetic intensity map of the geothermal target area was generated (Figure 12.).

The data was initially drift-corrected and survey corrected using Magmap2000® software. The data was then upward continued using MagPick® software.

The final magnetic data for the geothermal target area proved to be of very little use. Besides minor surface anomalies, such as metal fence posts or bundles of fencing wire, and the surface outcrops of crystalline rock, the magnetic survey does not appear to provide information of use in detecting subsurface features, such as in locating the buried Socorro Canyon fault. I interpreted that the surface alluvium's magnetic signature is high and variable enough that, once the survey moved away from a known outcrop out onto alluvium, any changes in rock type at depth became unnoticeable. The results of the magnetics survey did not yield structural information in the fault as expected, but rather a gradual gradient with high readings near surface outcrops to lower readings due to the thickening valley fill alluvium. The occasional metallic object would create a very strong shallow dipole as seen in Figure 13. Such metallic surface objects included metal T-post fence posts, old fencing wire, culverts, pieces of cable, and various small pieces metal debris. In an attempt to remove the surface signatures, an upward continuation was applied to the data (see Figures 14, 15, 16, and 17.). The results of the upward continuation show a very subdued change in contours uncharacteristic with a normal fault with bedrock to the west and valley fill to the east.

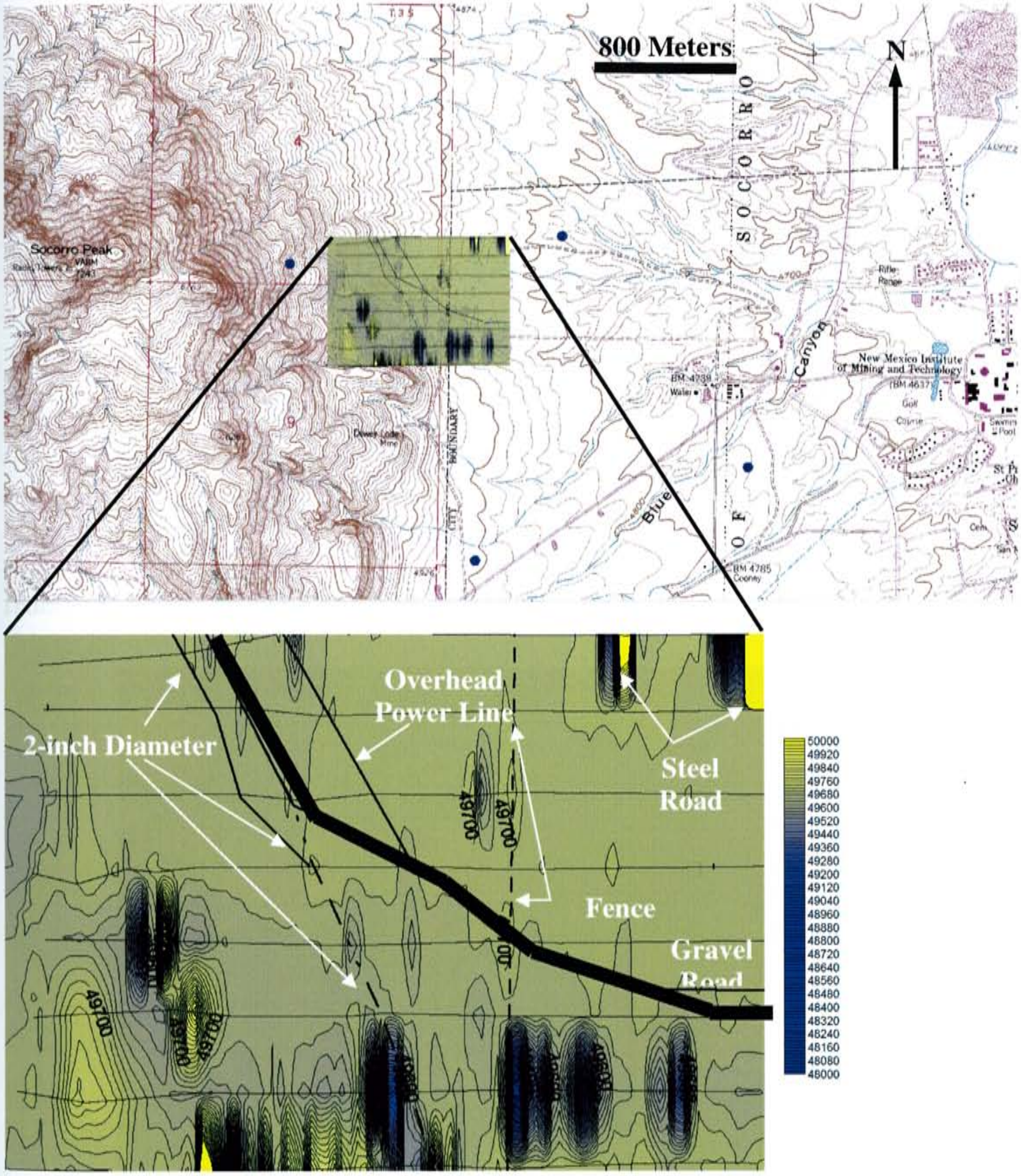

Figure 12. Magnetic intensity map (nano-tesla) showing known objects causing large anomalies. Wood's Tunnel road is passing through the middle of this area with EMRTC's West Road to the east just outside of this image.

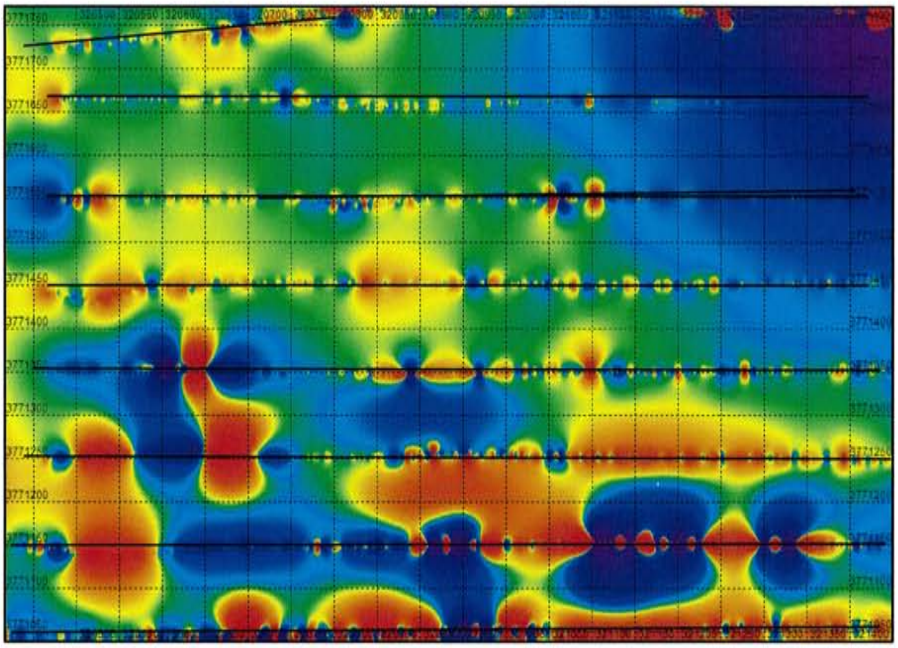

Figure 13. Original magnetic intensity data with no upward continuation. Output from MagPick Software 50-m × 50-m grid. Contours of nano-tesla.

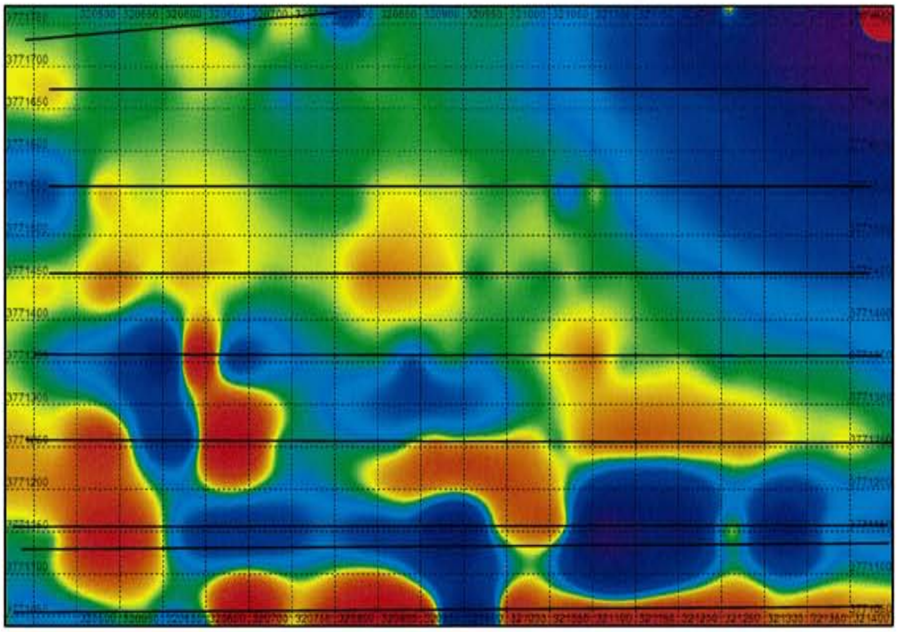

Figure 14. Magnetic intensity data with an upward continuation of 25 m. Output from MagPick Software 50-m × 50-m grid. Contours of nano-tesla.

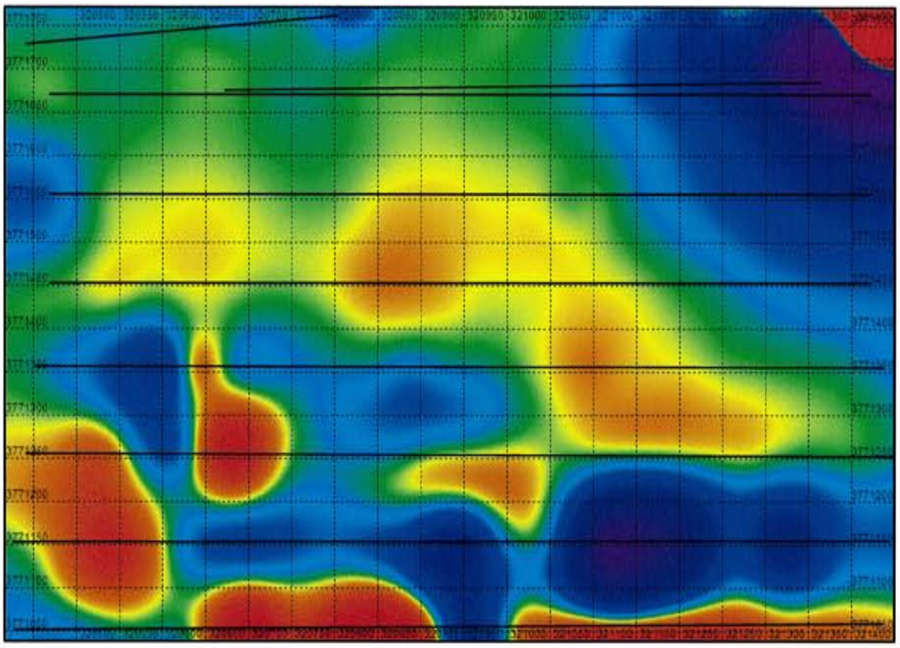

Figure 15. Magnetic intensity data with an upward continuation of 50 m. Output from MagPick Software 50-m × 50-m grid. Contours of nano-tesla.

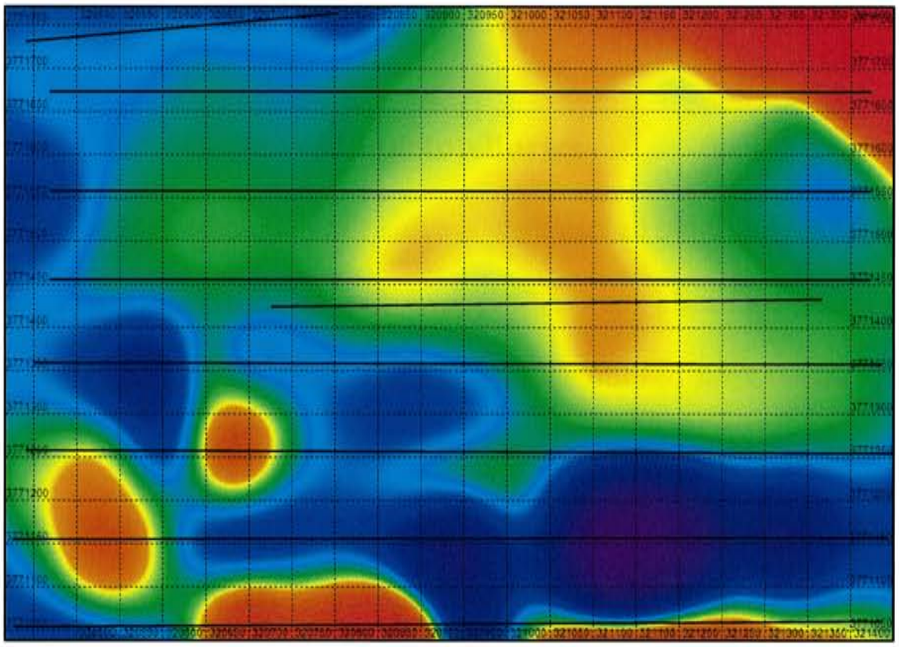

Figure 16. Magnetic intensity data with an upward continuation of 75 m. Output from MagPick Software 50-m × 50-m grid. Contours of nano-tesla.

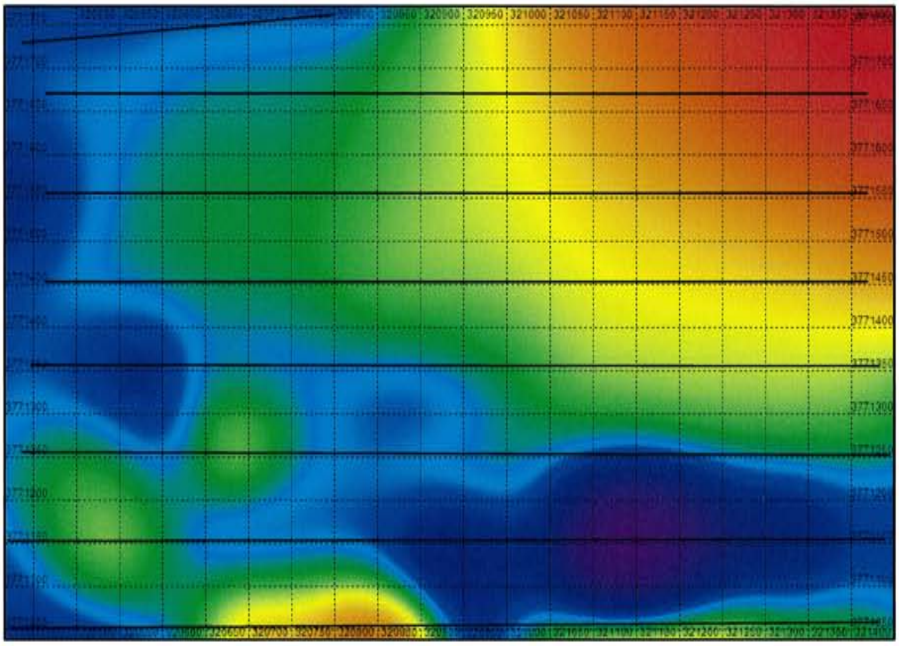

Figure 17. Magnetic intensity data with an upward continuation of 100 m. Output from MagPick Software 50-m × 50-m grid. Contours of nano-tesla.

Magnetotellurics

A series of high-resolution MT surveys were carried out in July 2005 by Quantec Geosciences. Four lines with an east-west profile were placed perpendicular to the Socorro Canyon fault (Figure 18.). The MT profiles utilized the Quantec Geosciences Titan 24 set up with additional stand-alone MT stations added to the east end of the profiles to extend the profile farther into the valley. Both magnetic and electrical field data were collected. The Titan 24 collection system was set up in a roughly linear east-

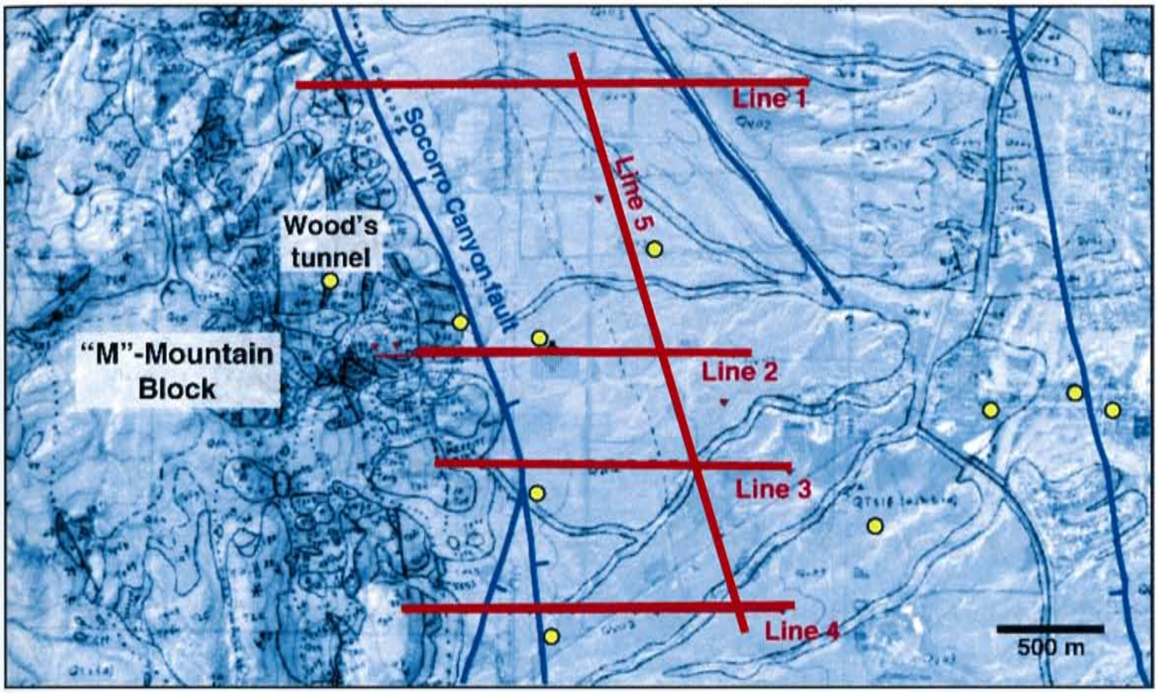

Figure 18. Location map of MT survey profiles and sounding stations, overlain on mapped geology of Chamberlain (1999). Mapped normal faults are shown in blue. Yellow circles are selected geothermal gradient wells of Barroll and Reiter (1990). Red lines are magnetotelluric profiles collected in July, 2005; line numbers correspond to Figures 21 through 25.

west configuration with 100-meter spacing between stations (Figure 18.). Four profiles were intended to target the Socorro Canyon fault as well as intersect areas of interest such as the Woods Tunnel area and regions to the north and south.

MT Theory

The magnetotelluric method is made possible due to natural low frequency magnetotelluric fields fluctuating and penetrating the earth (Reynolds, 1997). These magnetotelluric fields travel through the Earth passing through resistive and conductive materials creating telluric currents. Two sources of magnetotelluric fields are worth mentioning, first source is solar winds colliding with the Earths magnetic field providing low frequency sources of .0005 – 1 Hz. While the second source of atmospheric lightening generates frequencies of 1 – 400 Hz (Reynolds, 1997). A frequency range worth noting from .1 – 1 Hz is problematic and naturally weak and prone to noise.

The magnetotelluric method measures the electric and magnetic wave components of time variant fields to invert for resistivity correlating to depth. The basic MT method measures the secondary electric field generated by the time variable telluric currents (Sheriff, 1989). Two pairs of orthogonal electrodes are used to measure potential gradients which are characteristic of local geology and resistivity structures. In conjunction with the orthogonal surface electrodes the magnetic field must be independently measured with magnetic coils in an orthogonal orientation for X, Y, and Z. A total of six parameters are measured per individual sounding; the electric field in the X direction (E_X), the electric field in the Y direction (E_Y), the magnetic field in the X direction (H_X), the magnetic field in the Y direction (H_Y), the magnetic field in the Z direction (H_Z), and time (Sheriff, 1989). While collecting electromagnetic data for the area interest an additional MT station or remote reference station must be setup to simultaneously collect data for the same time series collected by the mobile surveying station. The purpose of the remote reference station is provide as noise free set of continuous data to correct and normalize the mobile MT stations data against. If located correctly the remote reference station will collect noise free data that can be used to correlate and correct for noise introduced by miscellaneous noise or other interferences common to this modern world. The remote reference station is to be located kilometers away from the survey area preferably away from any manmade electromagnetic sources while avoiding complex resistivity structures. The purpose being to collect as noise free data as possible over as homogenous geologic structure as possible.

Once data is collected with adequate sampling for longer period data, the data are Fourier transformed and stacked till adequate signal-to-noise ratios are obtained. A ratio of the electric field to the magnetic field is used to calculate a tensor impedance at discrete frequencies from which an apparent resistivity is determined. Polarizing the collected major fields, the apparent resistivity is calculated in two directions with major and minor axes generating an ellipse or polar diagram (Sheriff, 1989). The apparent resistivities are separated into two distinct modes parallel and perpendicular to strike. The transverse electric (TE) mode represents apparent resistivity parallel to strike. The transverse magnetic (TM) mode represents apparent resistivity perpendicular to strike. The transverse electric mode is generally simpler to interpret in a layer Earth model, but both modes require numeric modeling to resolve resistivity (Sheriff, 1989). A third invariant mode can be used to model geometric mean of the ρ_{XY} and ρ_{YX} data.

Assuming the remote reference location measures electrically uniform conditions, the resulting collected data would be equal in both E_X and E_Y resulting in a circular polar diagram with a unit radius. In the real world case the remote reference station would more likely record data that would produce an ellipse. The remote reference station ellipsoid is then mathematically manipulated to conform to the ideal unit circle. The same mathematical function is then used to manipulate the station survey data correcting for electric noise and time variant fields (Reynolds, 1998). The resulting polar diagram represents the distortion due to sub-surface targets and the multi-dimensional complexity of the telluric anomaly.

The next step involves numeric modeling converting the apparent resistivities as a function of frequency to resistivity as a function of depth. Correlation of the resulting resistivities with appropriate geologic structures is important at this time to verify quality of the data. Occam's inversions were used to model MT sounding data to smoothed resistivities. Knowledge of the area being modeled is needed so that modeled resistivity can be justified for corresponding geology. Interpretation of the modeled resistivities must then be corrected for topography and near surface conductors (Sheriff, 1989).

Magnetotellurics is a useful technique for geothermal exploration due to the fact that geothermal systems naturally create recognizable resistivity structures. MT uses natural electromagnetic fields that penetrate to multiple kilometers into the Earth with the limitation of weaker signal in the .1 – 1 Hz frequency range. This natural ability to penetrate the Earth and produce resistivity data make MT an ideal tool for mapping conductive clay caps and alterations associated with hydrothermal systems (Wright et al. 1985).

This is a brief description of magnetotelluric theory and method, a considerable wealth of knowledge and modern MT detail can be found by Vozoff (1991) and Wanamaker (2004) as well several sources of historic development of MT methods to date.

MT Field Methods

The MT survey was designed to image the structure of the Socorro Peak foothills, the dip and location of the Socorro Canyon fault, the hydrologic features and stratigraphy of the downthrown block, the rift basin stratigraphy, and any subsurface alteration associated with geothermal processes.

The MT data quality was high except for some stations closer to the town of Socorro, which were distorted by noise in the longer period readings. MT lines 1–4 from north to south were situated such that the west end of the profile would be on the lower flanks of Socorro Peak and the east end would terminate in the valley with the stand-alone MT stations providing additional coverage into the valley (Figure 18.). In addition to the profile extensions, the stand-alone MT stations were used to collect data in between the profiles such that a north-south profile could be created. In addition to the

MT survey lines, a continuously running base station was established across the Rio Grande River at a remote ranch location approximately 10 km away. The site was previously used as a remote MT location by P.Wannemaker (Wannemaker, 2004) and found to be a good remote reference location. The base station is located in a remote area such that urban electromagnetic noise is minimized providing the cleanest possible data which was then later used to process profile lines against. The original data was collected and processed by Quantec Geophysics and delivered as an .EDI file compatible with WinGLink® software. The MT data was qualitatively analyzed station by station and extraneous points were removed when deemed necessary to maintain the fit of the curve for the remainder of the inversion. The few data points that were removed were consistently located in the longer period data corresponding to depths greater then needed for this project (Personal communication W. Cumming 2006). A one-dimensional (1D) and two-dimensional (2D) inversion of the data was generated for each station, which was later used to produce the resistivity profiles for the four east-west profiles and the single north-south profile.

The MT field setup was laid out perpendicular to the Socorro Canyon fault with the west end of the MT line terminating in the foothills of Socorro peak. Through personal communication with Quantec Geosciences and in accordance with multiple published exploration methods (Morrison & Nichols, 1997; and Wannamaker (as well as others), a 100-m electrode spacing was determined to be sufficient for imaging shallow subsurface features. Using Quantec Geosciences equipment an extensive 24 station orthogonal array was deployed (Figure 19.). Data collection equipment was used to alternately wire potential and current electrodes along the array with a magnetometer station located at the east end of the array. Once the array was placed in the ground, electrodes buried, and data collection boxes wired a collecting station was established at the east end of the line, generally where a vehicle could be driven to the array. The array was then tested to verify proper wiring and function of data collection boxes. Once it was determined that all parts were collecting and transferring data, the official survey was ready to begin. Data collection times for the Titan 24 array were determined by Quantec operator based on collecting an adequate number of samples per period. Typical survey times lasted between 4-8 hours, depending on difficulties with batteries along the array. Excessive summer temperatures appeared to cause some of the older batteries to fail such that they would have to be replaced along the array before sampling could continue. Once adequate data was collected the raw information was refined and quality checked by Quantec Geosciences, and processed to an .EDI file format which could then be used by WinGLink software. Data was collected from 0.1 hertz (Hz) to 10 kHz frequency or 0.0001 seconds to 10 seconds period with the Titan 24 array.

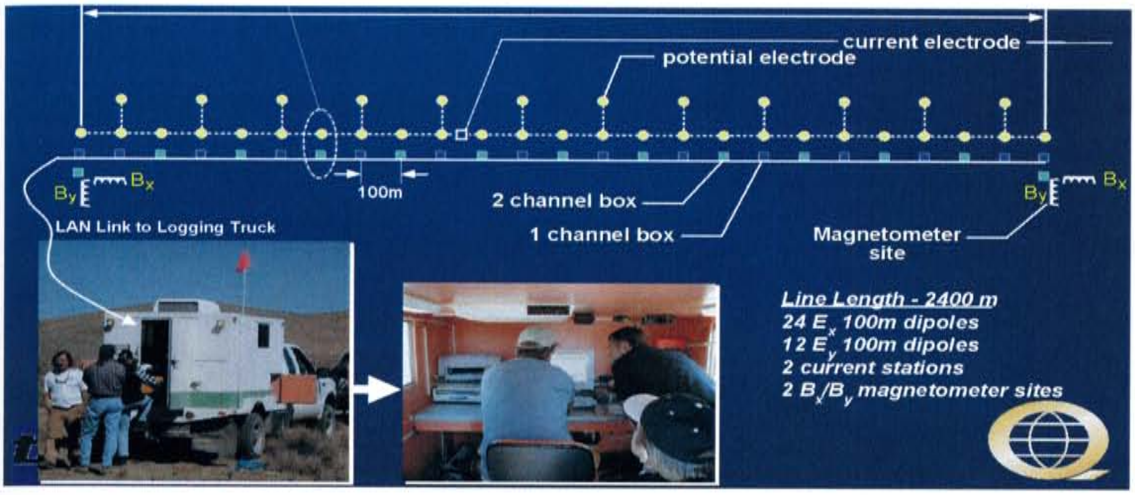

Figure 19. Quantec Geophysics Titan 24 MT layout. This layout was used in lines 1–4 for this survey with stand alone MT stations in combination with the Titan 24 lines to create line 5. Graphic supplied by Quantec Geosciences (personal communication, W. Doerner).

The stand alone MT stations used to augment the Titan 24 array are a more traditional setup, with 100-m-long orthogonal electrodes arranged in north-south and east-west directions, with an individual set of magnetometers all wired into a single data collector. The individual MT station was then allowed to collect data for a 24-hour period. Data was collected for 0.01 Hz to 100 Hz frequency range or 0.01 seconds to 100-second periods with the stand alone MT stations.

A common concern with MT is the quality of the data recorded. During the collection process, several errors can be introduced into the data in the form of electromagnetic disturbances and steep topographic elevation changes. These distortions manifest themselves into the data in the form of "statics," or static shifts of the data lateral offsets for the same reading (Orange, 1989). Sources of error could be as simple as urban electromagnetic disturbances such as power lines, radio equipment, and vehicular movement around magnetic coils. Steep topographic changes and large subsurface changes in resistivity can also introduce error into the data (Jiracek, 1990). Another tool to aid in the deciphering and qualitative analysis of the MT data is polar diagrams. These three-dimensional (3D) representations of the resistivity tensor give a graphical display of the degree of three-dimensional distortion in the data. Polar plots are generated at varying periods throughout each individual MT station (Figure 20.). The MT data collected for these four east-west profiles consistently show low distortion at shorter periods with increasing three-dimensional distortion at longer periods.

Due to the high quality of the data collected by Quantec Geophysics, the data set was nearly free of statics and no static corrections were applied (Personal communication, W. Cumming, 2005). Careful consideration was taken in laying out the MT lines such that topographic changes would be minimized, although topography could possibly cause a minor galvanic error in the data at the west end of the MT profiles (Jiracek, 1990). Topographic error was deemed minor and not corrected for (Personal communication, W. Cumming, 2005). The MT inversion data was contoured using the elevation measured from individual stations on a 100-m spacing. TM mode was emphasized when fitting the data minimizing any statics due to minor changes in

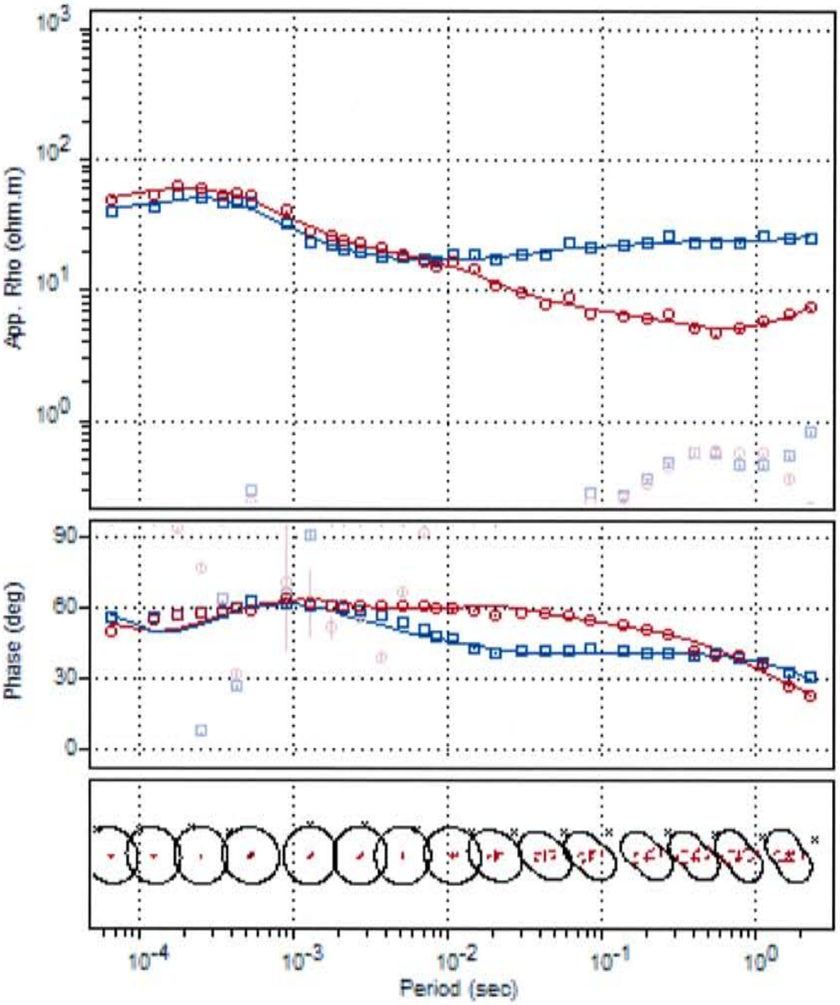

Figure 20. Sample MT sounding with curve fit lines for model, Line 1 Station 4. Red TE (XY) and Blue TM (YX) symbols represent actual data collected, red and blue lines represent model curve fit. Upper graph is apparent resistivity (faded symbols are the original data before rotation to a true East-West profile). Middle graph is phase of collected data, with lines representing model fit to phase. Lower graph shows polar diagrams for each appropriate period of collected data. Polar diagrams show complexity of the data in the case of this figure, the data becomes more complex at longer periods (right side of graph) deviating from the unit circle as described in MT theory section. All model fits can be found in Appendix B.

topography (Personal communication, W. Cumming, 2005). To truly correct all statics, Time Domain Electromagnetic (TDEM) data should have been collected per individual station. The TDEM data would provide a resistivity value from which the TM or TE curve could be shifted to appropriately to resolve statics. Procedurally correcting for statics would involve resolving TDEM soundings to acquire an observed value. The MT apparent resistivity curves could then be shifted to correspond to the TDEM resistivity value therefore eliminating any static shift (WinGLink processing manual, 2007 citing work by Sternberg, 1988 and Pellerin, 1990). Since TDEM was not collected for this survey no direct static corrections have been made.

Using WinGLink® software, 1D and 2D resistivity processing was used to prepare five cross sections. Four east-west trending cross sections were generated along the MT surface profiles, with an additional north-south trending cross section parallel to strike (Figure 18.).

These 1D inversions compute the 1D, or "sounding," resistivity structure beneath each individual station along the line. Results are plotted side-by-side then simply contoured to produce the appearance of a 2D resistivity pseudosection. These 1D inversions are susceptible to the effects of resistivity structure variations not aligned directly below the stations; however, they are not susceptible to lateral smoothing effects of 2D inversion algorithms and regularization. Hence, the 1D inversions are useful for their greater resolution of the shallow structure such as the uppermost 100 500 m below the surface based on distance between stations. Conversely, the 2D inversions tend to resolve resistivity structures much deeper (500 to 3000 m) by using surrounding stations along each line in the inversion process (personal communication, W. Cumming, 2006). The algorithms that invert for structure in this 2D method may smear shallow structure laterally, but do a better job of correctly placing larger-scale zones of conductivity and resistivity at depth (personal communication W. Cummings, 2006). Hence, these 2D sections are more useful for the interpretation of larger scale structures beyond 500 m below the surface.

The stitched 1D Occam inversions, or 1D inversions, of the invariant mode MT data and the 2D inversions showed similar results in the upper 1500 m. Invariant mode is used for modeling 1D data such that the MT tensors are jointly modeled instead of emphasizing TM mode or TE mode individually. For 2D inversions, it was initially assumed that the Titan 24 profiles were ideal dip profiles and the MT data were rotated numerically to the profile direction (Figures 21, 22, 23, 24, and 25.). Subsequent 2D inversions were also based on TE and TM mode, but all of the resultant profiles 1D and 2D correlate resistivity structures similarly. TE and TM pseudo-sections for the individual MT lines can be found in Appendix A (Figures 33, 34, 35, 36, and 37.). Pseudo-sections are a profile displaying the apparent resistivity values per mode (TE or TM) versus period to display lateral variation along the profile.

Results

Results of the data collected on each line are shown in both 1D and 2D inversions (Figure 21, 22, 23, 24, and 25.). Profiles for each line are shown for below with a 1:1 scale. Profiles show resistivity structure to a depth of 1.25 km. Depth must be calculated from the collected time series data. MT sounding depth is based on the exponential decay of electromagnetic as they diffuse into a material. The skin depth relationship dictates that for a given sounding period depth is dependant on the average conductivity of the material over a uniform half space. The skin depth relationship is defined by the following Equation 1.1.

$$p(T) = (T/\pi\mu\sigma)^{1/2} \qquad \text{(Eqn. 1.1)}$$

Where $p(T)$ is the electromagnetic skin depth in meters for a given period T, μ is magnetic permeability, and σ is the average conductivity of penetrated material (Simpson, 2005).

Lines 1–4 all cross the main Socorro Canyon range-bounding fault in the western third of the lines and sample areas on both the west (footwall) side as well as the east, or

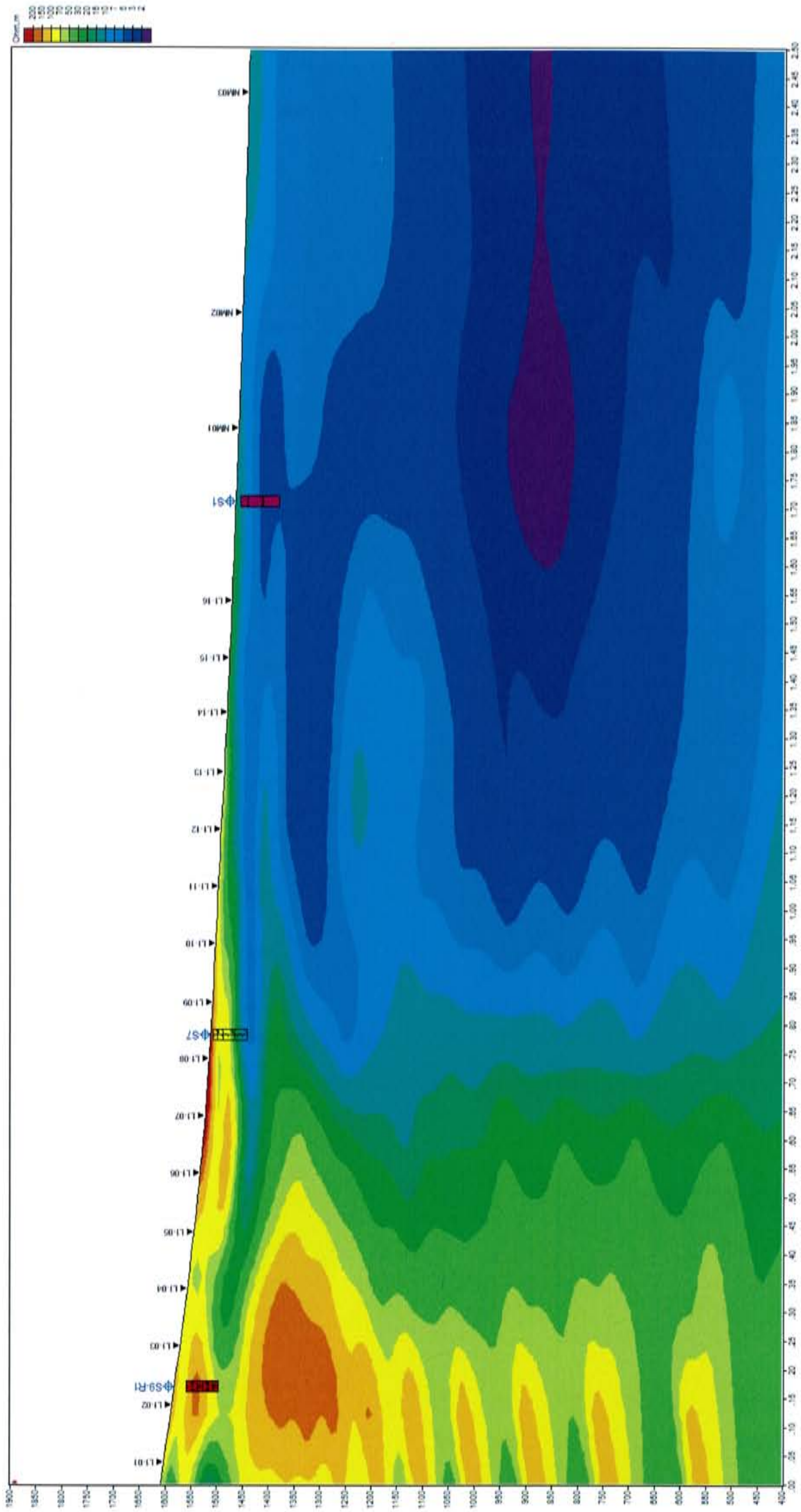

Figure 21A. MT survey data on Line 1. 1D inversion of data.

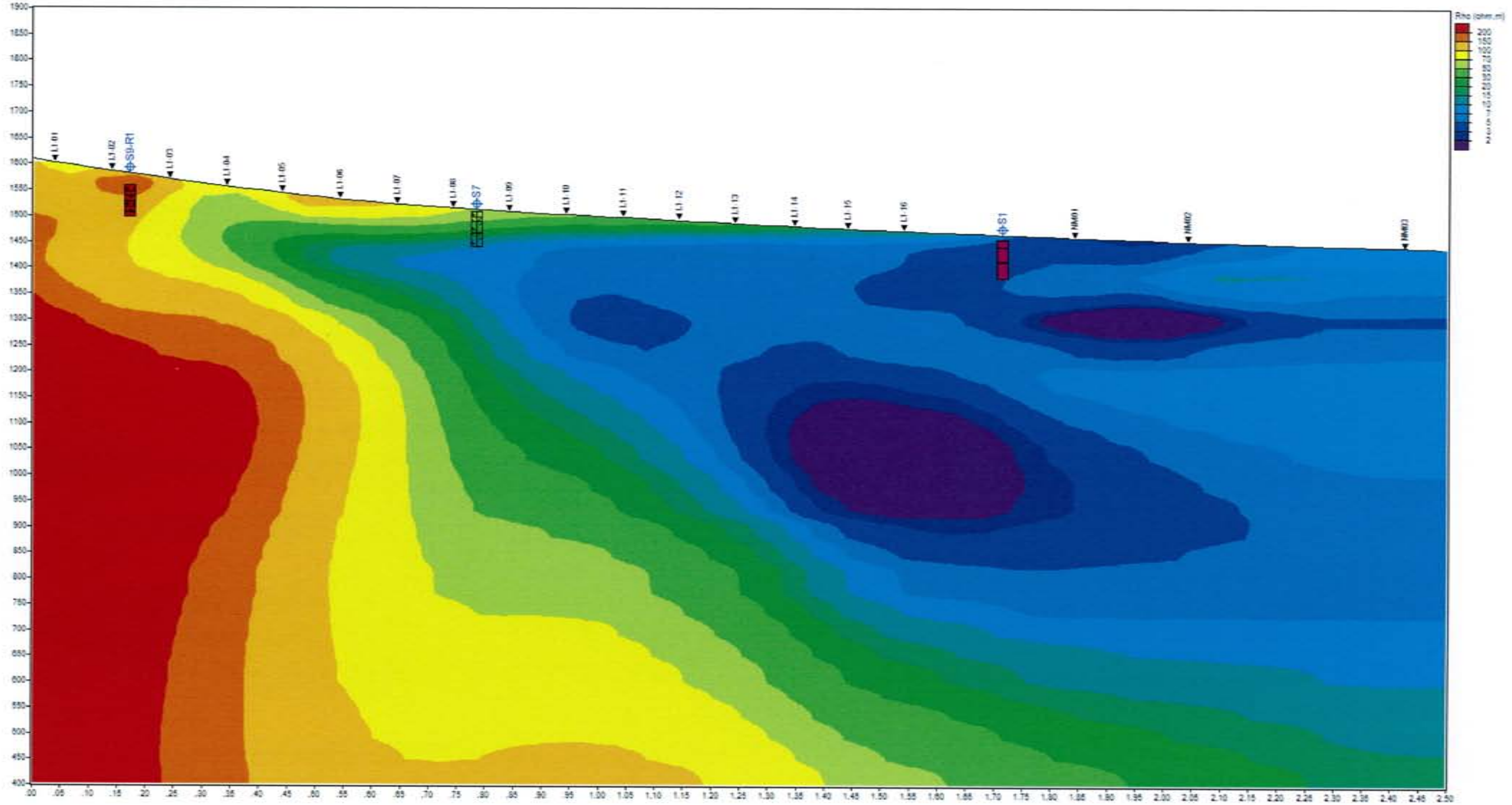

Figure 21B. MT survey data on Line 1. 2D inversion of data. Color scale is resistivity in Ohm-m. Vertical scale is elevation above sea level in meters.

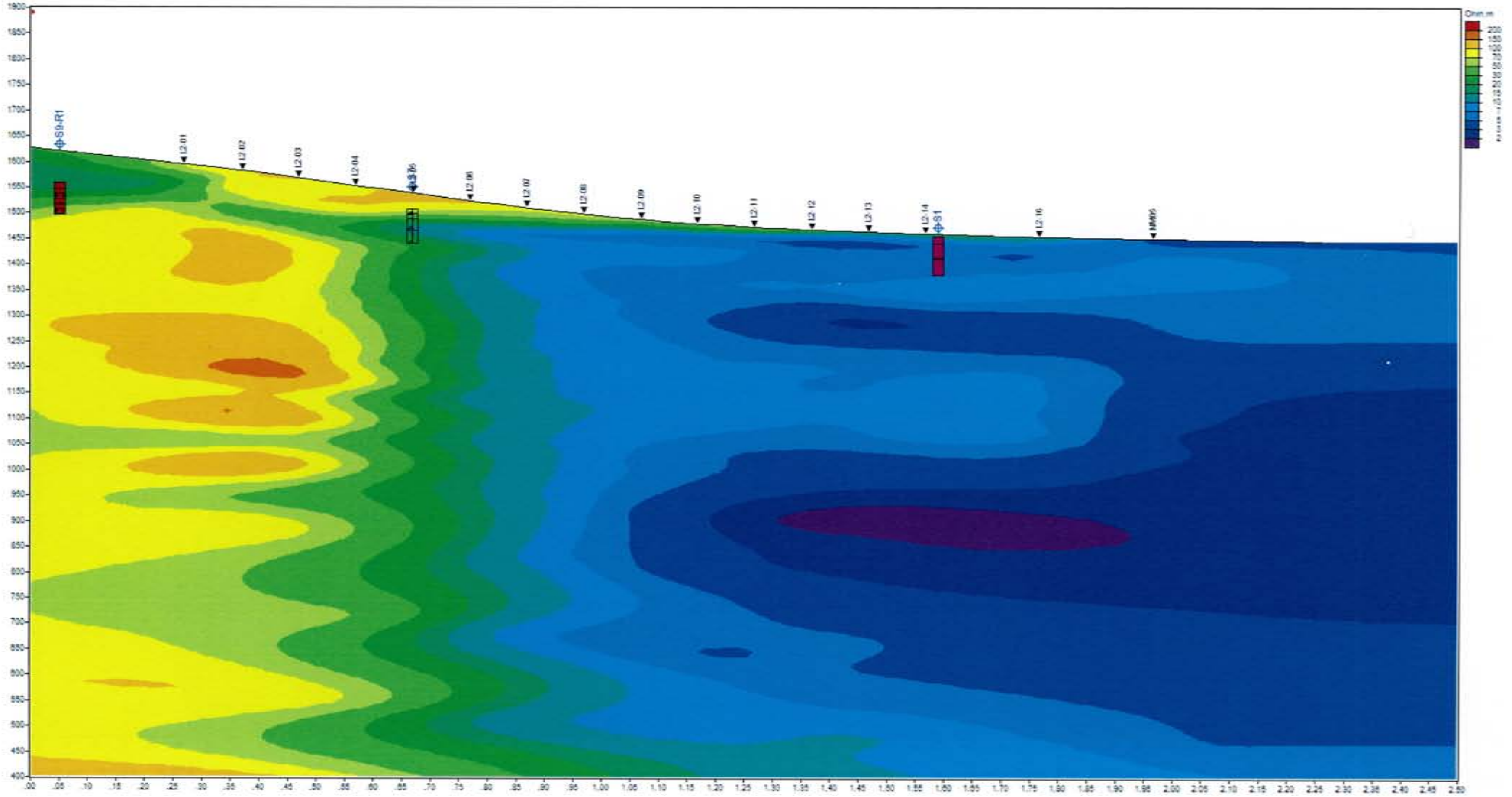

Figure 22A. MT survey data on Line 2. 1D inversion of data.

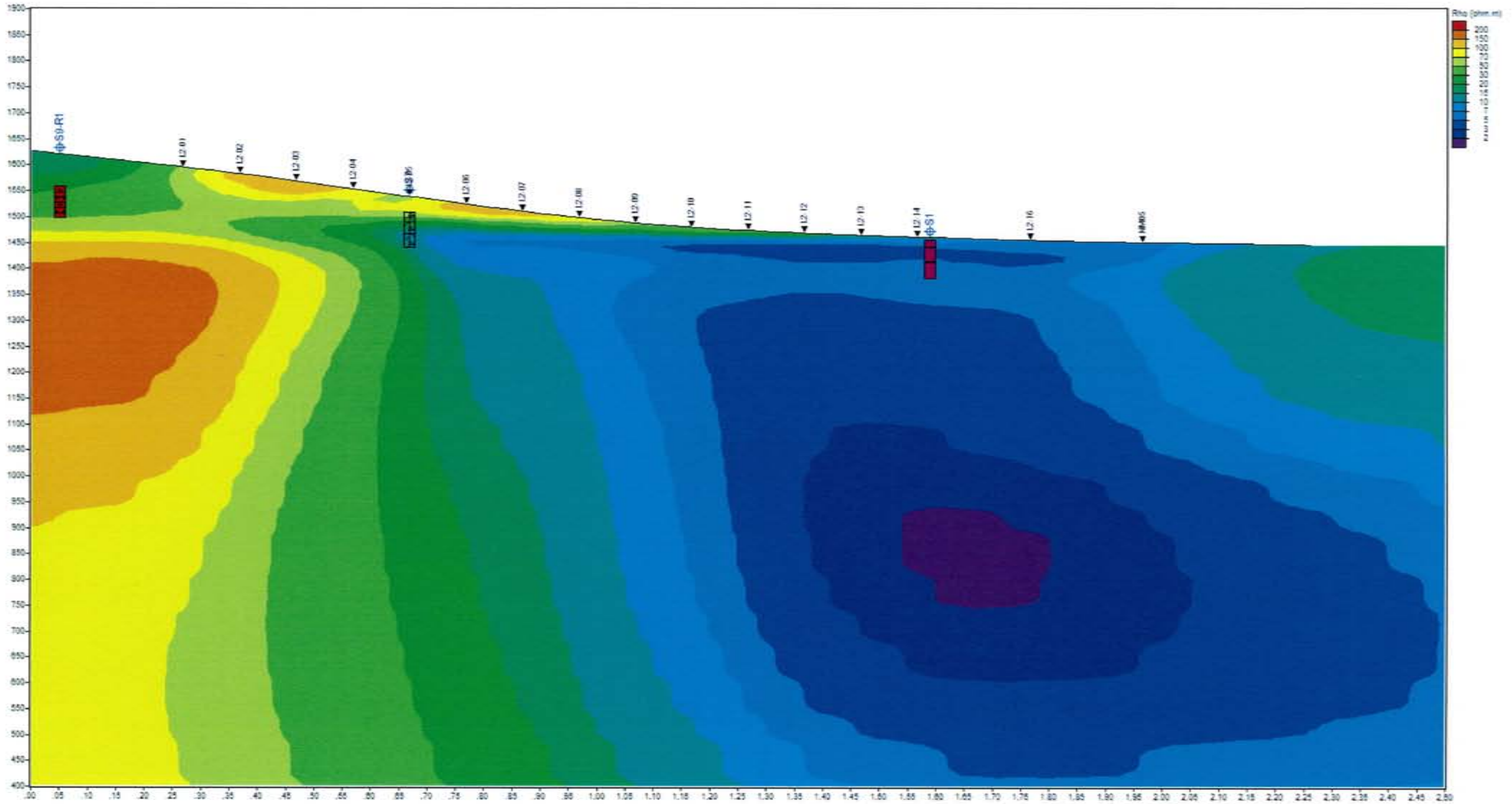

Figure 22B. MT survey data on Line 2. 2D inversion of data. Color scale is resistivity in Ohm-m. Vertical scale is elevation above sea level in meters.

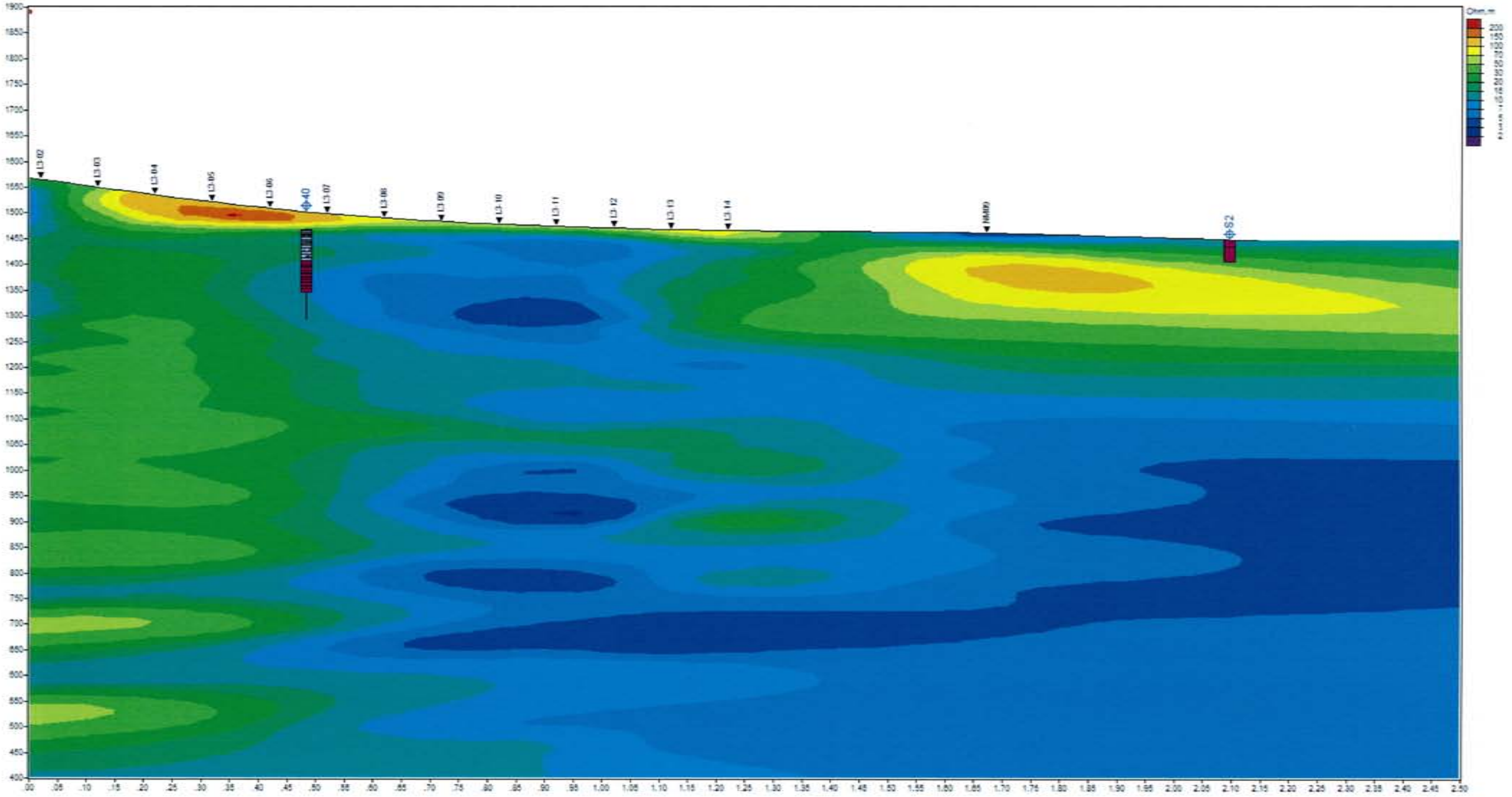

Figure 23A. MT survey data on Line 3. 1D inversion of data.

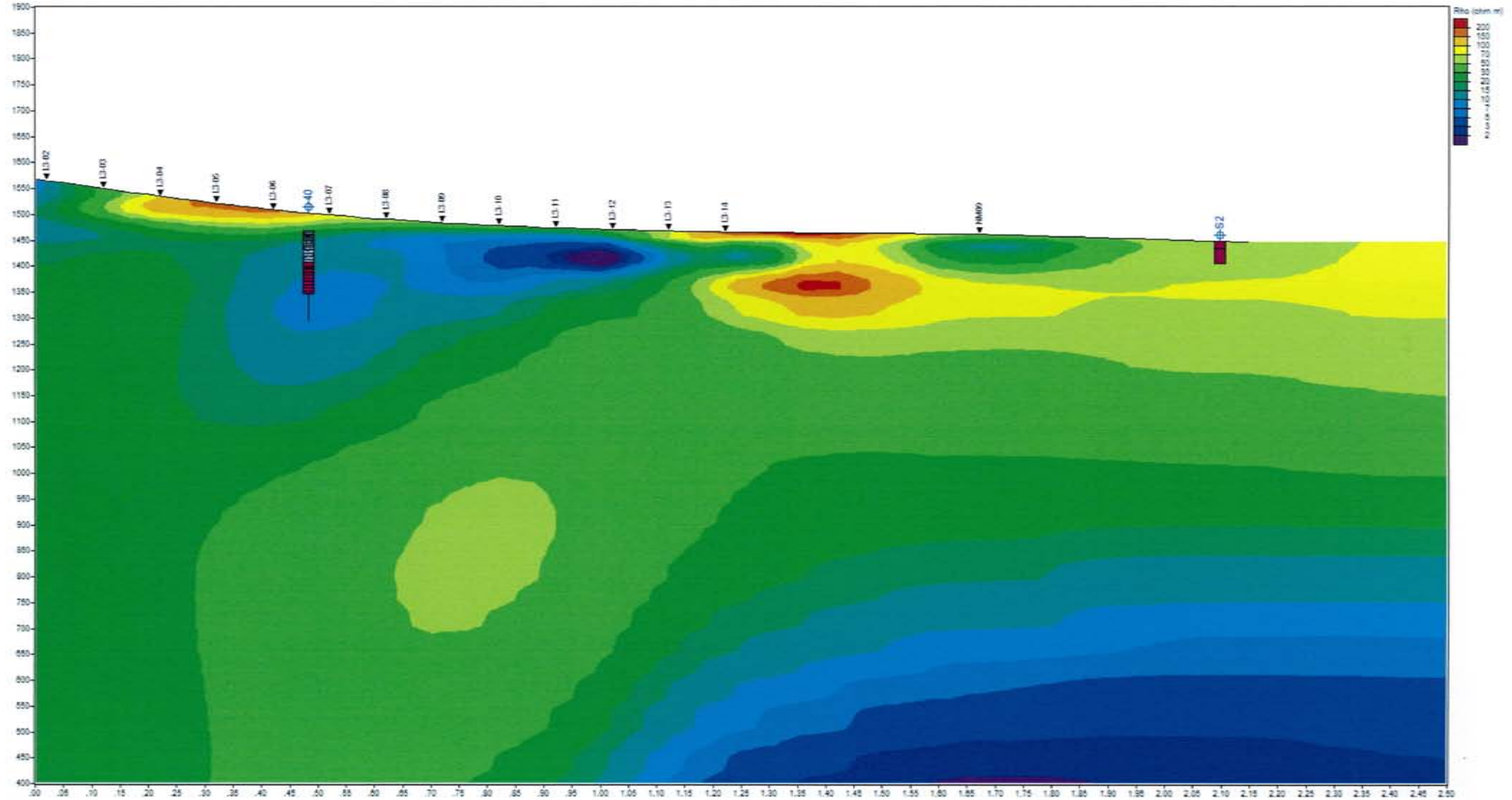

Figure 23B. MT survey data on Line 3. 2D inversion of data. Color scale is resistivity in Ohm-m. Vertical scale is elevation above sea level in meters.

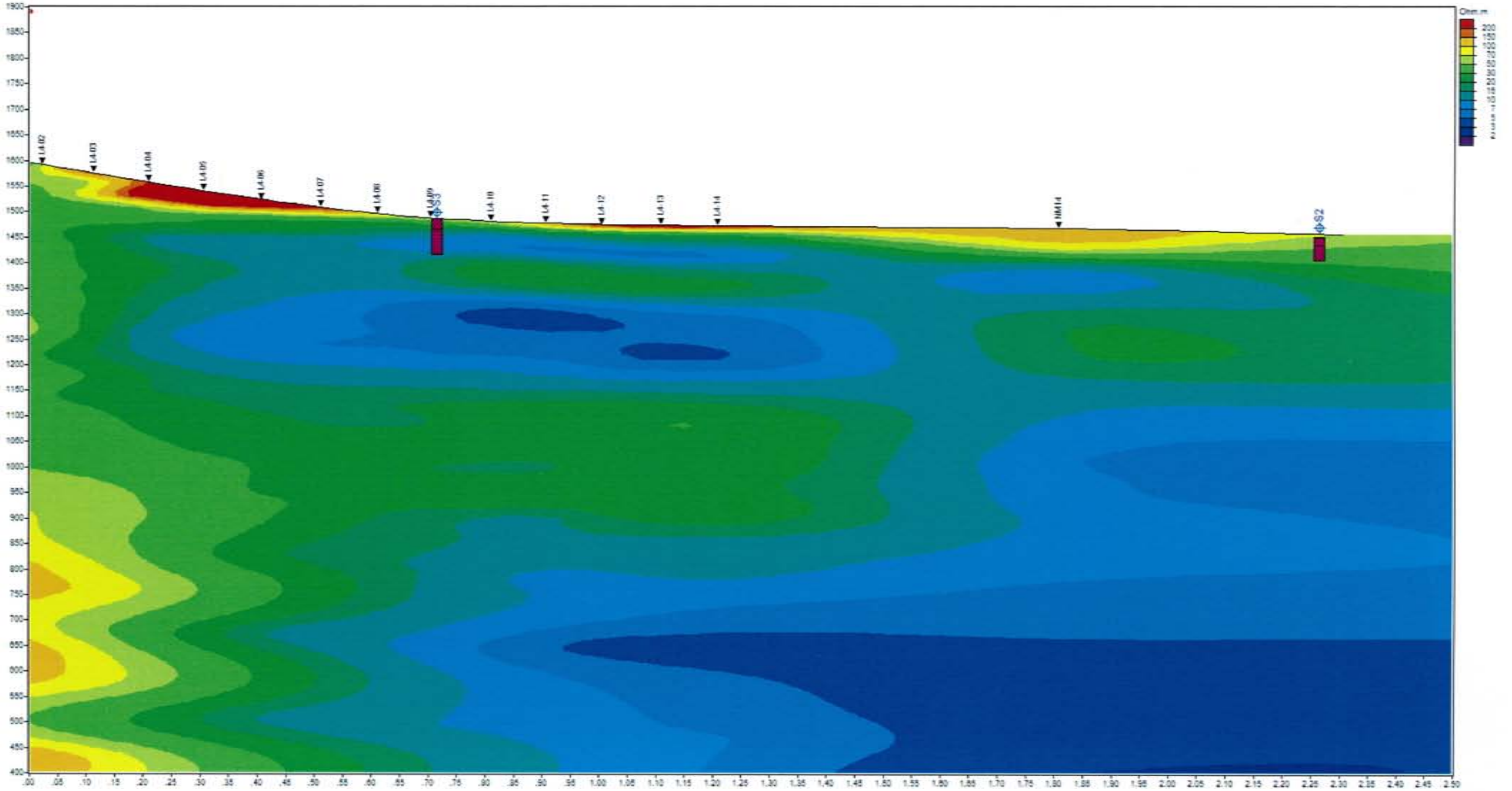

Figure 24A. MT survey data on Line 4. 1D inversion of data.

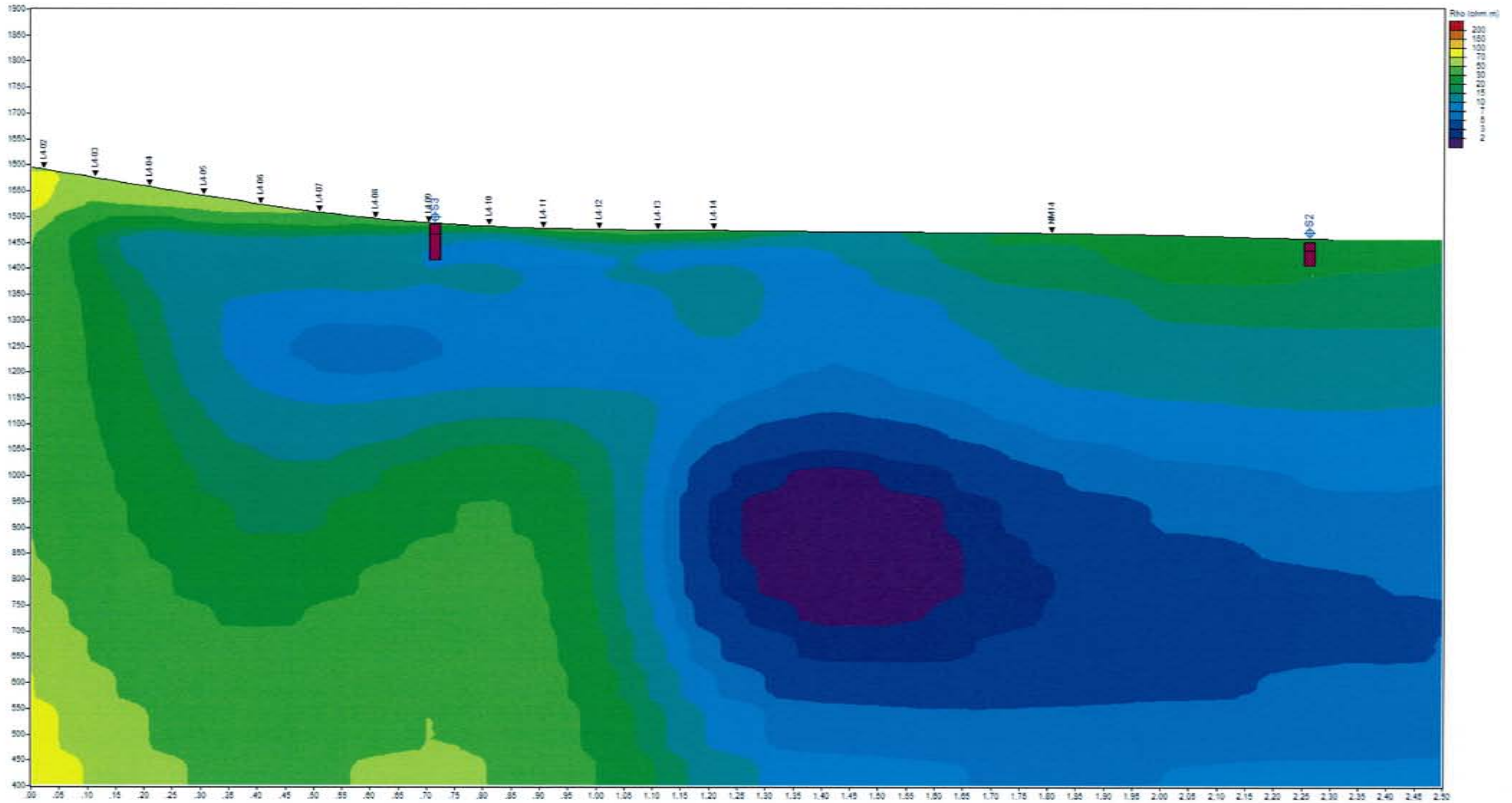

Figure 24B. MT survey data on Line 4. 2D inversion of data. Color scale is resistivity in Ohm-m. Vertical scale is elevation above sea level in meters.

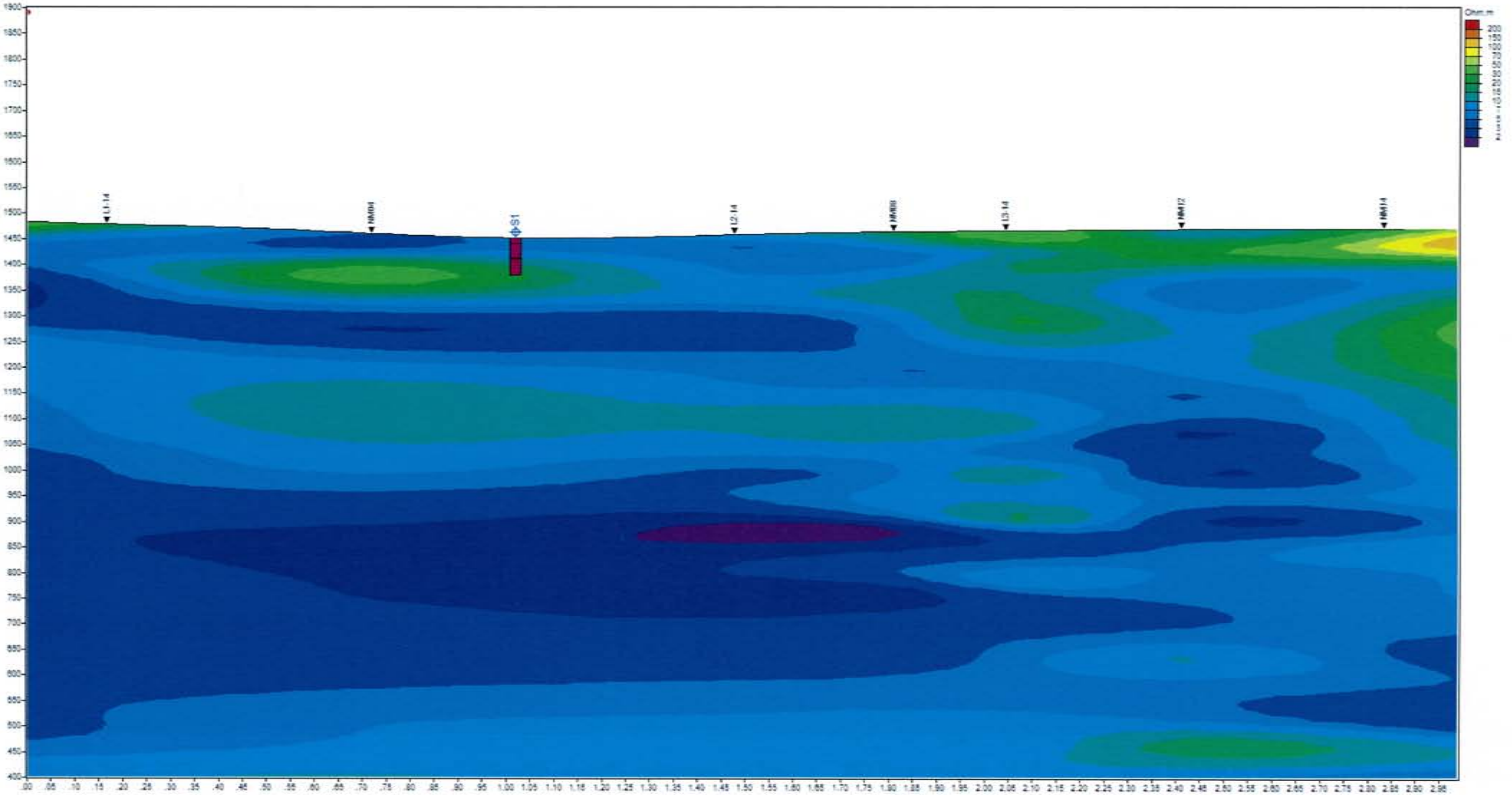

Figure 25A. MT survey data on Line 5 (North-south composite line). 1D inversion of data.

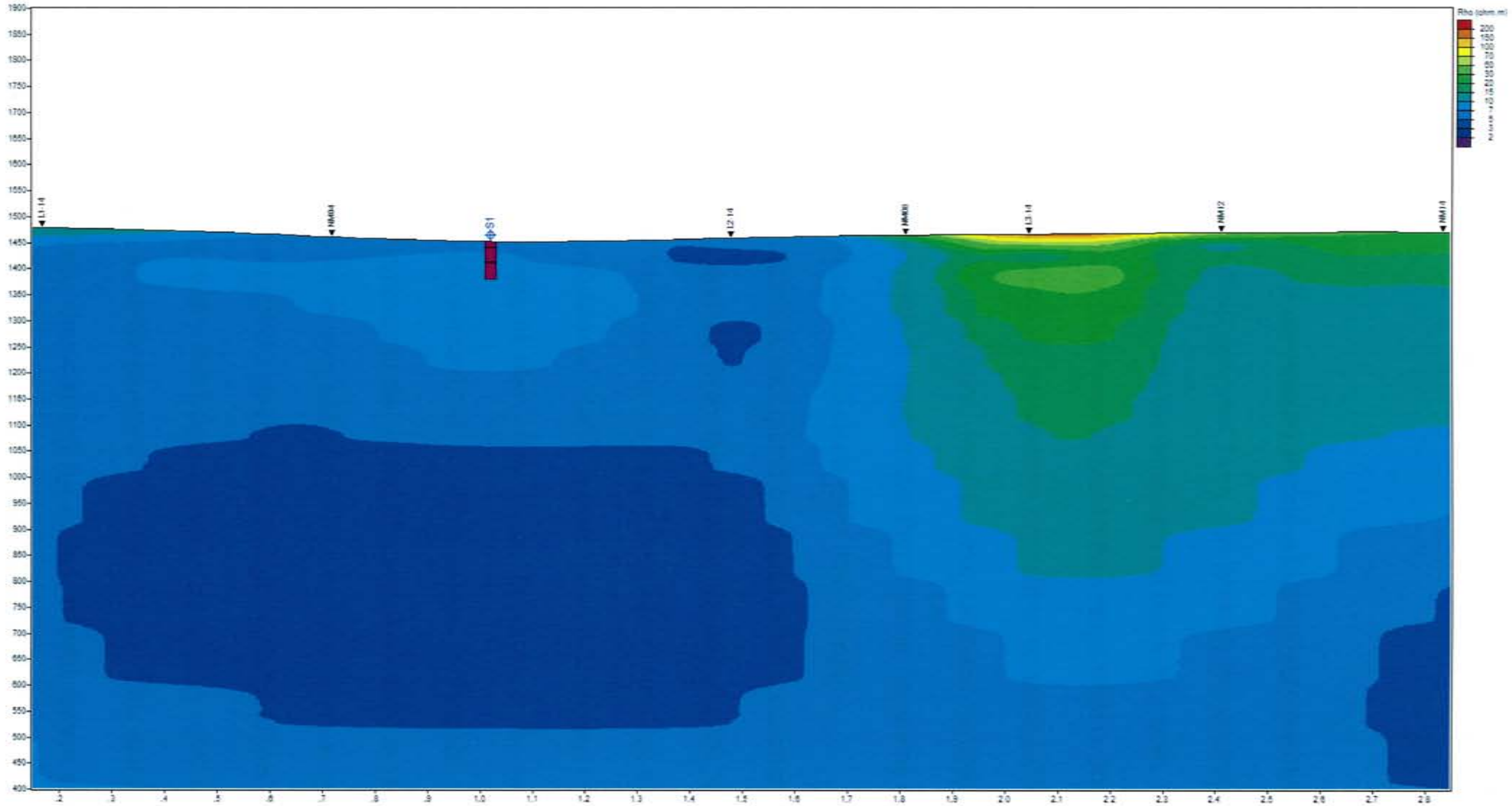

Figure 25B. MT survey data on Line 5 (North-south composite line). 2D inversion of data. Color scale is resistivity in Ohm-m. Vertical scale is elevation above sea level in meters.

hanging wall, side. Line 5 is a north-south section which roughly parallels the Socorro Canyon fault, tying into all four east-west lines. In general, the contrast between the footwall block of greater resistivity and the hanging wall block of greater conductivity is clearly imaged in all four lines. The footwall resistivities range from 0–300 Ohm-meters (Ohm-m), consistent with relatively conductive crystalline or meta-sedimentary rock, perhaps heavily fractured, mineralized locally, and saturated hydrothermal fluids (Telford, 1990). Field observations suggest the Precambrian basement and Paleozoic section of carbonates and siliciclastic sediments meet this description.

The hanging wall block was anticipated to consist of an accumulation of alluvial sediment and debris flows derived from the adjacent mountain uplift, unsaturated to depths of 50 to 100 m, and underlain by the Upper Popotosa Formation, a more lithified unit consisting of fluvial and alluvial clastic sediments with abundant volcanic ash or debris, and significant amounts of clay. The Upper Popotosa is the unit thought to represent the confining layer (aquitard) for the flow system feeding the warm Socorro Springs complex several kilometers to the south. At a site about 1500 m south of Line 4, and in a similar position to the eastern end of that line, an exploratory water supply well was drilled to a depth of 366 m, and a clayey layer thought to be the Upper Popotosa was encountered at 357 m. Regionally, the Upper Popotosa is typically ~300 m in thickness (Chapin et al., 1979; R. Chamberlin, personal communication). This unit is underlain in turn by the Lower Popotosa, characterized by coarse alluvial debris and ignimbrite deposits related to the eruptions of the Socorro Caldera. High permeability in this unit is thought to form the aquifer system hosting the flow feeding the warm springs.

The hanging wall side of the surface fault trace (approximately eastern half of each Figures 21 to 24.) is generally characterized by resistivities below 10 to 15 Ohm-m, and ranging as low as 1 to 2 Ohm-m. These conductive zones are heterogeneously distributed spatially. On Figures 21, 22, and 24, a zone of greatest conductivity is clearly imaged. The depth to the peak value of conductivity is shallowest on Line 1 (about 400 m), and seems to deepen in Figures 22 and 24. On Figure 23, the footwall zone appears to be less conductive than on the other three lines. This is apparent on the north-south composite profile Figure 25. It is not clear whether Figure 23 is in a location of different lithology or structure, or if another reasons accounts for this difference. However, Figure 23 is located just east and down slope of the largest historical mine working on the mountain block, and perhaps the alluvial history of this profile differs due to being down slope from a significant mineral deposit.

We interpreted the high conductivity zone in Figures 21, 22, and 24 (and apparent in Figure 25) as the signature of a deep aquifer system, never drilled for water supply or other reasons. It is likely to be either the Upper Popotosa clay-rich and saturated unit (the confining layer) or, equally likely based on its depth, conductivity associated with the Lower Popotosa aquifer unit. The conductivities are low enough to represent a zone of significant connectivity of water-bearing pores or fractures, though the salinity of any such fluid and the clay content are unknowns that could strongly affect conductivity. However, the correlation to the nearby recent city well, and other known geology, suggests that the interpretation that this zone corresponds to the permeable intervals in the Popotosa Formation is at least plausible.

The footwall or western side of Figures 21 to 24 is characterized by resistivity values in the 70–300 ohm-meter range. The more resistive zones are interpreted to be the mountain block on the western portions of the profiles. Figures 21 and 22 are positioned farther west then Figures 23 and 24 allowing for Figures 21 and 22 to show more of the footwall mountain block shown with red to yellow contours. Figures 23 and 24 are situated near the edge of the footwall of the mountain block but do not have enough station profile coverage to resolve data for the mountain block but cover the Socorro Canyon fault as planned in the survey. Coverage at the far west ends of Figures 21 and 22 shows a circular pattern indicating that data is there for interpretation but more data the west would be needed to smooth the model and make a nicer figure. With prior knowledge of the geology in the area a discrepancy arises. The mountain block is composed of multiple rock types ranging from limestones to arkosic quartzites with the PreCambrian basement being the later in the area of Wood's tunnel (Witcher and Owens, 2007). Common resistivity values for clean quartzites range from 10 to 12×10^8 ohm-m with resistivities for general metamorphic rocks ranging from 100 to 10^8 ohm-m with the majority of resistivities at the higher end of the range (Telford, 1990). Drilling results

(Witcher and Owens, 2007) indicate that the recovered quartzite within the core was highly fractured with considerably altered. So the resistivity values in Figures 21 and 22 are still within the range of resistivity values for a quartzite basement. Further results from drilling indicated a shallow water table within the footwall of the mountain block. Upon testing of water samples recovered post drilling the water was found to be brackish further confirming that lower resistivity values are possible for the footwall material. Aqueous geochemistry is currently being conducted with results to be published at a later time. The resistivity values shown for the mountain block can be justified by highly fractured altered arkosic quartzites below the water table saturated in brackish fluids.

The MT profiles also indicate the Socorro Canyon fault doesn't have a buried step down fault block within the upper two kilometers of crust as indicated in some un-constrained cross sections (Chamberlin, 1999, Gross and Wilcox, 1983). Although Figures 21 to 25 show the upper 1.25 km of material, there is no indication of a down thrown fault block beyond 1.25 km depth.

Remote Sensing

During the course of this exploration work, a pilot study of thermal anomalies detected by satellite-based infrared Advanced Spaceborne Thermal Emission and Reflection Radiometer (ASTER) images was conducted over the Socorro Peak area (Table 1). The ASTER images are a basic level 2 brightness temperature at sensor image without multiple band data (NASA Jet Propulsion Laboratory website, 2007). Initial examination of these images using ESRI ArcGIS software indicated that the Socorro Peak heat flow anomaly is recognizable in a database of images spanning 4 years. The ASTER images have been analyzed, and a relatively consistent correlation between the known areas of elevated heat flow within the mountain block and the corresponding ASTER image suggests that the geothermal anomaly has been detected (Figures 26 and 27.).

The database of ASTER images were individually examined to remove images that were obstructed by cloud cover or wind streaks, both common weather effects.

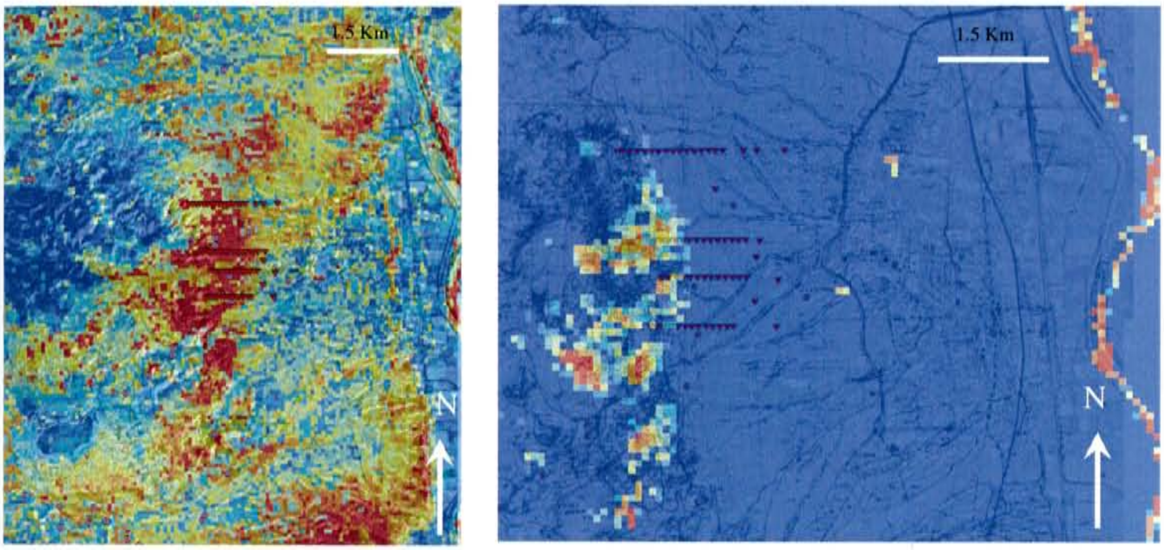

Figure 26. Sample ASTER image with false color values (left). Red pixels are 25°C warmer then background values, yellow are 10–15°C higher then background values, and blue and light blue pixels are 5–10°C higher than background temperatures. Pixels are 90-m × 90-m square. Notice Socorro Peak's east and south east flank appears to be hotter as does the Rio Grande River to the east. The triangles are the MT profile lines and the city of Socorro can be seen between the mountain and river. Background is a geologic map adapted from Chamberlin (1999). Night image taken on 3-3-2005, 5:22:59 UTC.

Images were then adjusted to optimize contrast to verify a consistent localized warm spot. Further analysis was conducted to verify that the warm spot was visible in both the night images as well as the day time images. The localized anomalies were typically more prominent in night time images than day time images; however both day and night images verify a visible warm spot. Individual pixel values were examined to confirm feasible temperature ranges. I concluded that Socorro peak has a visible warm spot on the east facing side of the mountain.

The history of using remote sensing to explore for geothermal systems has been fraught with technological and environmental problems which continue to make work and breakthroughs in this field challenging. Further work is needed to validate this observation from ASTER images. Further work needs to verify reflectivity of Socorro Peak and approximate an albedo for the rock types. Work is needed to analyze vegetation, absorptivity of the rock type, approximate thermal inertia, thermal capacity, elevation correction, and other remote sensing constraints prior to making a conclusion with confidence that is a true surface representation of geothermal heat using ASTER imagery. Validation of the ASTER images could, however, prove to be one of the most rewarding aspects of this work. My preliminary conclusion is that the ASTER heat flow anomaly appears to have a very strong signature, and therefore there is real potential for thermal imagery to be used to identify geothermal systems. The ASTER images tend to

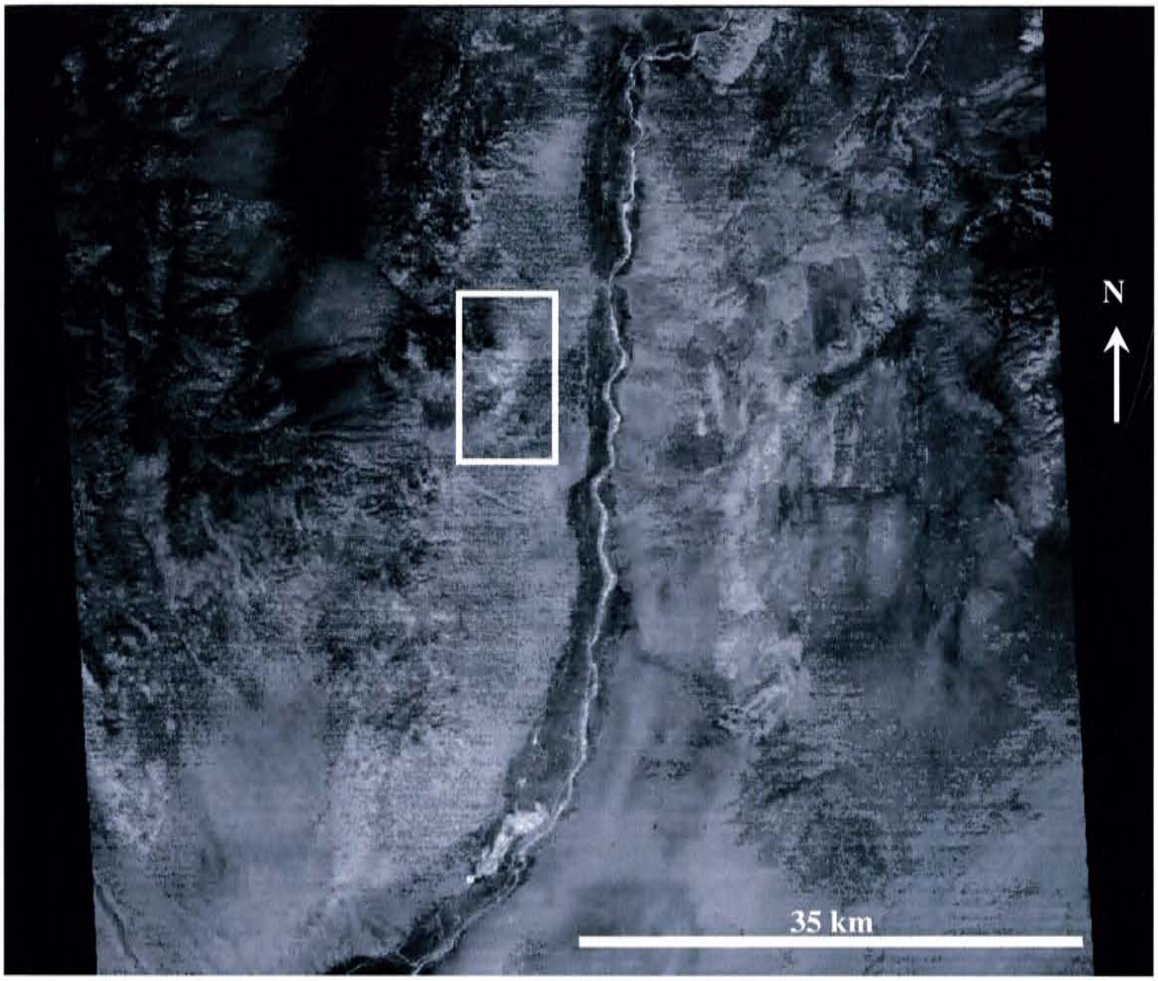

Figure 27. Sample ASTER image of Socorro, NM in original black white format. Night image taken on 3-3-2004, 5:22:59 UTC. Bright pixels represent higher temperatures. Rio Grande River can be seen running north to south with Bosque Del Apache showing up with bright ponds to the south. Socorro peak is highlighted with rectangle. Pixels are 90-m × 90-m square.

	All Images	Usable Images
Day	41	3
Night	78	28
Total	119	31

Year	#of Images
2000	10
2001	33
2002	45
2003	12
2004	18
2005	1
Total	119

Table 1. Tabulation of ASTER thermal image database. Significant number of day time images were unusable due to obstructed views due to weather or the target area is partially obstructed.

correspond nicely to the heat flow contour map further proving that the ASTER images have a very high potential (Figure 28.).

Preliminary results of the ASTER data indicate a images have temperature differences between 5°C to 25°C between hotspots and background valley temperatures. Further work needs to be completed to statistically quantify the relevance of the current thermal images. If found to be worth while as currently expected, requests for multi-channel imagery could be purchased and a full evaluation of a geothermal surface expression could be pursued.

Conceptual Model

The purpose of this work was to conduct a geophysical analysis of the known geothermal anomaly to define subsurface structure, aiding in the targeting of an exploration drill

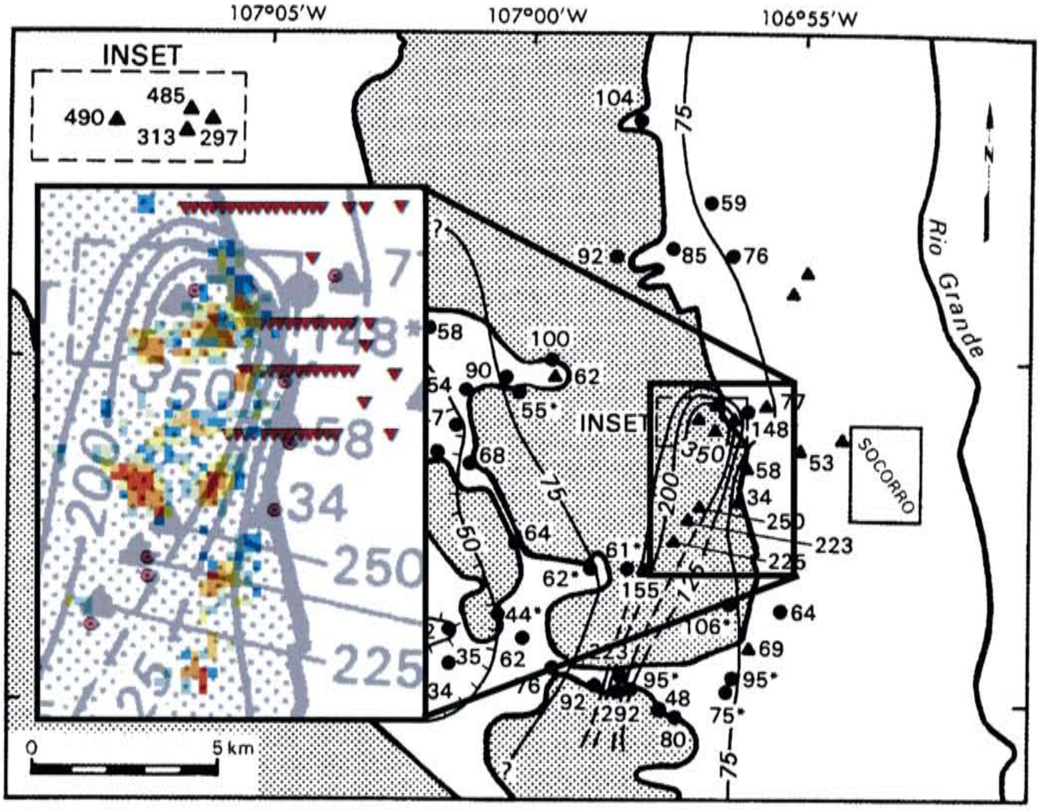

Figure 28. ASTER image of Socorro, NM highest temperature pixels from Figure 26 overlain on Barroll heat flow contour map. Red pixels are 25°C warmer then background values, yellow are 10–15°C higher then background values, and blue and light blue pixels are 5–10°C higher than background temperatures. Red triangles are MT stations along profiles 1–4. Color pixels are 90-m × 90-m square. Minor translational errors are present when scaling non-digital maps into digital form.

hole. The magnetotellurics, gravity, magnetic, and remote sensing analysis all contribute new information to the previously known heat flow and hydrologic models (Barroll and Reiter 1990, Mailloux et al. 1999). The geophysical work answered several questions about the subsurface in the region of interest. First, the gravity work confirmed that the

Socorro Canyon fault has considerable offset of 1000 or more meters with no identifiable step down sub-blocks, based on modeling of data collected by A. Sanford (Appendix C) and (Figure 10.). The magnetic work was inconclusive, because the surface alluvial material largely obscures any subsurface signature of the Socorro Canyon fault. The magnetotelluric data provided the most insight into the subsurface surrounding the geothermal area of interest. The MT data shows that there was no sign of a buried shallow geothermal feature in this area: no sign of clay alteration or sharp resistivity contrasts found with other geothermal systems as described by Wright et al. (1985) and Pellerin et al. (1995). However, the MT confirms that the west side of the Rio Grande Valley is a deep horst and graben valley. Interpretation of the MT data confirm that hydrological flow models (Barroll and Reiter 1990, Mailloux et al. 1999) appear to be feasible, with lower than expected resistivity values for crystalline basement rocks, suggesting a large degree of fracturing and saturation. Further interpretation of the MT data identifies large conductive deep lying zones within the valley. These conductive zones most likely represent the lower Popotosa aquifer unit.

The profile resistivity ranges from 1 ohm-m (blue) to 200 ohm-m (red). Resistivity of 1 to 15 ohm-m (blue to light blue) is correlated to the Popotosa and similar clay-rich zones, or possibly warm aquifers, on the east end of the profiles. The 20 to 200 ohm-m (green to red) zone is correlated with the porous altered volcanics and crystalline rocks in the mountain block on the western end of the profiles. Between these and in the basin, there is a zone of intermediate 5–15 ohm-m (light blue to green) resistivity that probably consists of coarse alluvial material. These resistivity patterns correlate closely with the existing geologic model of the region. (Figure 29.).

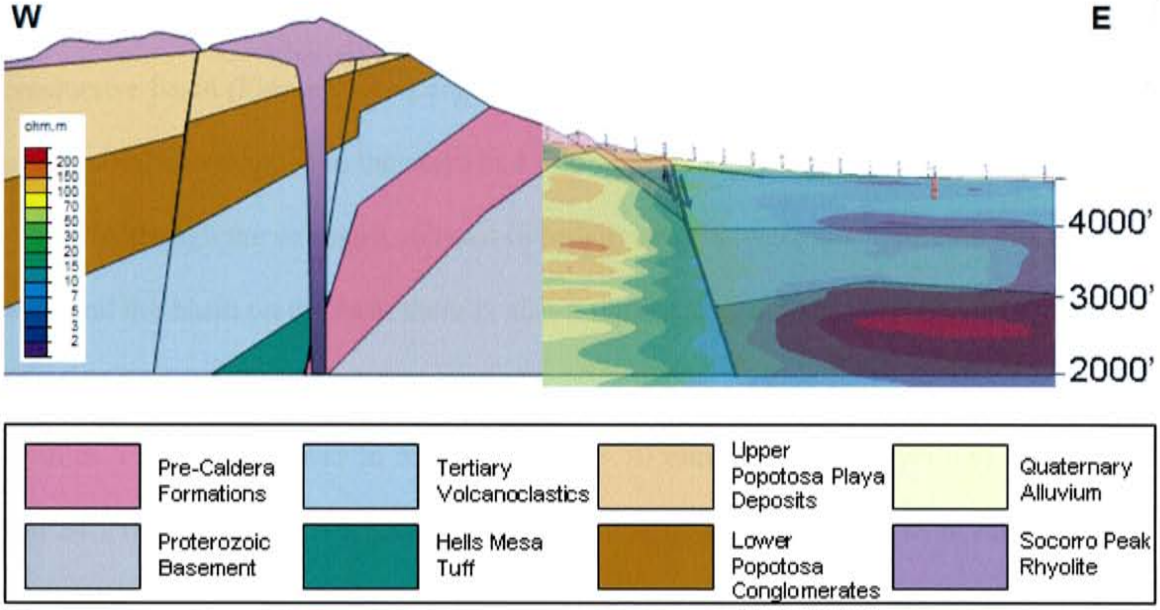

Figure 29. Simplified geologic cross section from Chamberlin (1999), with 40°C and 60°C temperature gradient lines. MT line 2 (1D) is overlain showing reasonable match to Socorro Canyon Fault and subsurface lithology of the valley. Elevation units of feet.

The geology of the sub-basin is poorly constrained below approximately 300 meters. The deepest well in the area reached a depth of only 310 meters, just penetrating the upper contact of the Upper Popotosa clay playa aquitard. This clay unit is correlated with the 300 or more meters thick, low resistivity unit with a top imaged at about 300-m depth in profiles 1, 2, 3, and 4 (Figures 21, 22, 23, and 24.). No buried bedrock blocks are imaged in the upper 1500 m of the basin east of Socorro Canyon fault trace.

The Socorro Canyon fault that bounds the western edge of the basin in all the sections is interpreted to lie within the intermediate resistivity transition zone of conductive down-faulted coarse alluvium between the resistive mountain block and the conductive basin (Figure 21.). Large fanglomerate facies formed during periods of rapid uplift have been mapped to the north and south of this area.

Although the strongest contrast in resistivity is between the mountain block on the west and the basin on the east, there is also a significant gradient in resistivity from north to south (Figure 25.). The interpreted volcanics below 700+ m depth on the west end of Profiles 3 and 4 are lower in resistivity, 15 to 70 ohm-m (green to yellow) (Figures 23 and 24.), than the 70 to 200 ohm-m (yellow to red) crystalline intrusives in Profiles 1 and 2 (Figure 21 and 22.). These patterns are consistent with the caldera rim between Profiles 3 and 4 that elevates the resistive mountain block to the north. The north to south resistivity patterns in the basin are consistent with the expected thinning of the Upper Popotosa clay playa from north to south (Chamberlin 1999).

A conceptual analysis of the Socorro Peak geothermal system has been developed based on available heat flow data, hydrologic and geologic models, and with the addition of new geophysical and geochemical data. Like other Basin and Range style systems, the Rio Grande rift has created an asymmetrical tilt and uplift of a basement fault block with adjacent half grabens, such that fluid in the recharge area of the Magdalena Mountains can travel deep into the basin subsurface eventually getting trapped under thick Upper Popotosa aquitard materials. The fluids are then heated and forced to travel through the Socorro Peak mountain block along fracture and matrix permeability. These heated fluids are manifested as mixed warms springs flowing from the uplifted fractured volcaniclastics to the south of the target area; however, it is speculated that deeper and presumably higher temperature advective fluids are flowing into a confined aquifer within the downthrown block capped by Popotosa playa sediments.

Drilling

Upon careful consideration, a drill site was targeted for Wood's Tunnel pad. This location was determined due to the historically high heat flow concentration, the placement on the footwall side of the Socorro Canyon fault providing access to the fractured basement rock.

Drilling commenced in November 2006. Core was intermittently recovered to a depth of 73.15 m (240 ft) where, due to complications with equipment and conditions, drilling ceased (Table 2). Drilling began in mine tailings from the Wood's Tunnel prospect then transitioned to surface alluvium, succeeded downhole by faulted and mixed mountain debris, a mixture of large intact faulted wedges of Madera limestone and the Sandia formation with thick layers of fault gouge and rubble intermixed. The exploration hole eventually terminated in Precambrian quartzite at a depth of 73.15 m (240 ft). The last 14.3 m (47 ft) consisted of fractured Precambrian quartzite, exhibiting fracture apertures on average of 1 cm with quartz mineralization as well as interbeds of unconsolidated pebble conglomerate and kaolinite alteration (Witcher and Owens, 2007). A static water level was measured at a depth of 67 m (220 ft) with open formation exposed in the bottom 12.2 m (40 ft) of the hole. Permeability is primarily believed to be from extensive fracturing and course matrix of the Precambrian rock, although reservoir properties have not been determined at this time.

The exploration hole NMT-4-67T, similar to the Socorro Springs (32°C to 34°C), contained warm water at very shallow depth (Barroll, 1990) (Figures 30 and 31.). A bottom hole temperature of 33.5°C was measured at a depth of 73.15 m (240 ft) in the slim hole. This translates into a temperature of 65°C at a depth of approximately 228.6 m (750 ft) (65°C is a target temperature for a closed loop heating system) (Owens and Witcher 2007). At this time, the hole has not been logged for resistivity or other common downhole logging methods. This temperature is considerably warmer than the average ground water temperature of 16°C to 21°C for the Rio Grande valley and 15°–18°C for La Jencia Basin to the west (Barroll, 1990).

Table 2. Summary Geologic Log from Owens and Witcher (2007)

From	**To**	**FORMATION**
M	**M**	**Lithology, unit, age, structure**
0	14.6	mine dump tailings
14.6	30.9	mixed lithology alluvium/colluvium, poor formation returns
		Quaternary alluvium
30.9	46.9	interbedded shale, limestone, and silicified limestone, mostly
		fractured, **Pennsylvanian Madera Formation**
46.9	51.2	fractured gray silicified limestone, **Pennsylvanian Madera Formation**
51.2	53	mostly brown clay with black mineralized vein, possible fault zone
		Pennsylvanian Sandia Formation
53	54.6	coarse pebbly silicified sandstone, mostly fractured or brecciated
		Pennsylvanian Sandia Formation
54.6	54.8	dark blue gray clay, **Pennsylvanian Sandia Formation**
54.8	58.8	coarse pebbly silicified sandstone, mostly fractured or brecciated
		Pennsylvanian Sandia Formation
58.8	73.1	Brecciated jasperiod and fine crystalline quartzite, mixed fault zone(s)
		Pennsylvanian Sandia Formation, Precambrian metasediment

The fluid flow from this exploration hole appears to be largely from fracture and matrix permeability. This conclusion is based on recovered core with open fracture apertures and silica infilling in minor fractures, cracks, and voids. During drilling, it was a very difficult task to keep circulation of the drilling fluids as the fractures transported the drilling muds away (Witcher and Owens, 2007). No further work has been conducted to determine aquifer properties to date (pump test). At this time (April 2007), the exploration hole is being considered for a continuation of drilling to a depth of 750 ft to 800 ft and completion as a production well pending favorable results of temperature and fluid resource at depth.

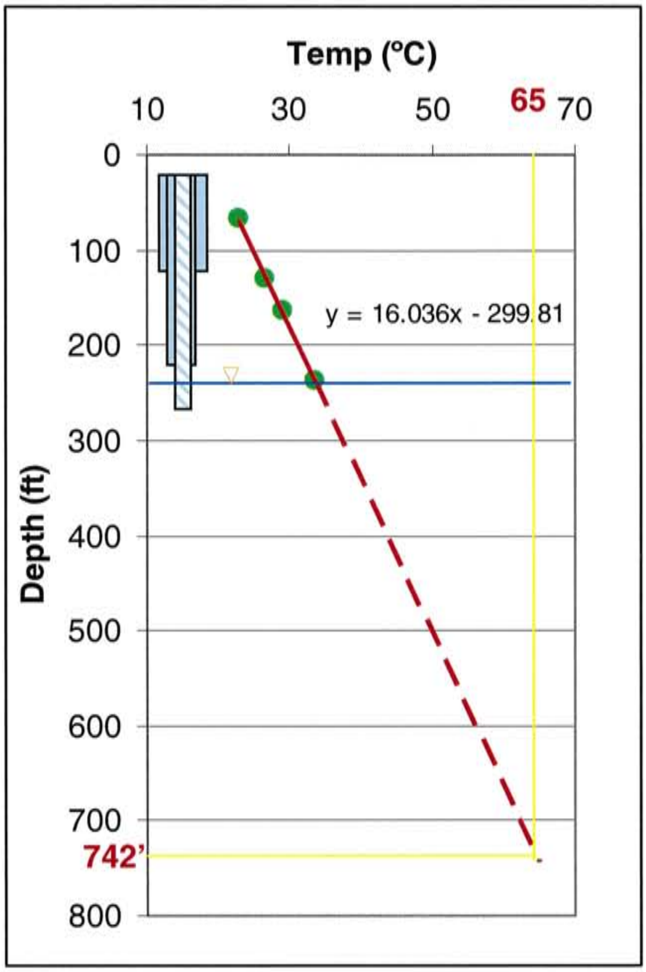

Figure 30. **Temperature profile of completed well. Solid red line represents actual thermal profile; dashed red line represents projected thermal profile to 226 m (742 ft), static water table at 67 m (220 ft) from Witcher and Owens (2007).**

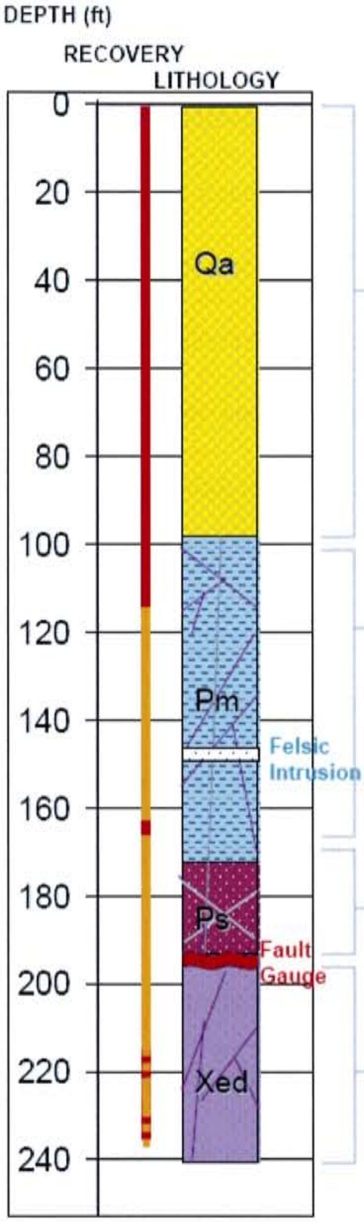

Colluvium: unconsolidated colluvial fill; boulders of various composition (silicified limestone, volcanic, sandstone)

Pennsylvanian Madera: Brecciated to silicified limestone, vuggy with sandstone interbeds, fossils identified. Easily fractured, indurated with clay alteration; quartz hydrothermal mineralization in veins

Pennsylvanian Sandia: Coarse-to-medium grained arkosic quartz arenite with limonitic coating. Mottled clay matrix along fractures with kalolinite and/or sericite clay and unconsolidated pebbly conglomerate interbeds. Heavily fractured with quartz mineralization along fractures.

Precambrian Fm: Below fault, unit is a microcrystalline, well silicified arkosic quartzite with interbeds of unconsolidated pebble conglomerate and kalolinite alteration. Vein aperture increases to 1cm ave. Continued quartz mineralization observed in veins, limonitic mineral coating with clay vein fill.

Figure 31. Lithologic log for exploration hole NMT-4-67T. Red in the recovery column represents no recovery of core, log then developed from drill cuttings (Witcher and Owens, 2007).

CONCLUSIONS

Magnetotelluric surveys along with other geophysical techniques have enabled a much broader and more detailed subsurface picture of the range bounding fault west of the town of Socorro, New Mexico. The data collected and profiles generated provide a greater insight into the electromagnetic nature of the basin margin and also provide sight into the Popotosa aquifer and Upper Popotosa aquitard providing previously unknown extents and structures above and below. The MT profile and forward model of the gravity data provided more insight into the shape of the Socorro Canyon fault and the previously unconfirmed absence of a smaller step down fault buried at depth. Such step-down faults have been found using MT exploration methods and also provide geothermal trapping mechanisms and drilling targets. Coso geothermal field in California is an example of such a system (Wanamaker, 2004). Geophysical modeling and geochemical analysis (Hill, 2006 and Owens, 2007) have aided in providing a drilling target for geothermal fluids at Socorro Peak. A detailed fence diagram of the MT data provide a three dimensional image of the basin and its placement in relation to Socorro peak mountain block (Figure 32.).

Drilling has confirmed that the Precambrian basement rocks of Socorro Peak are highly fractured and saturated confirming a lower resistivity then expected for Precambrian basement rock in this area. Drilling also concluded that brackish thermal

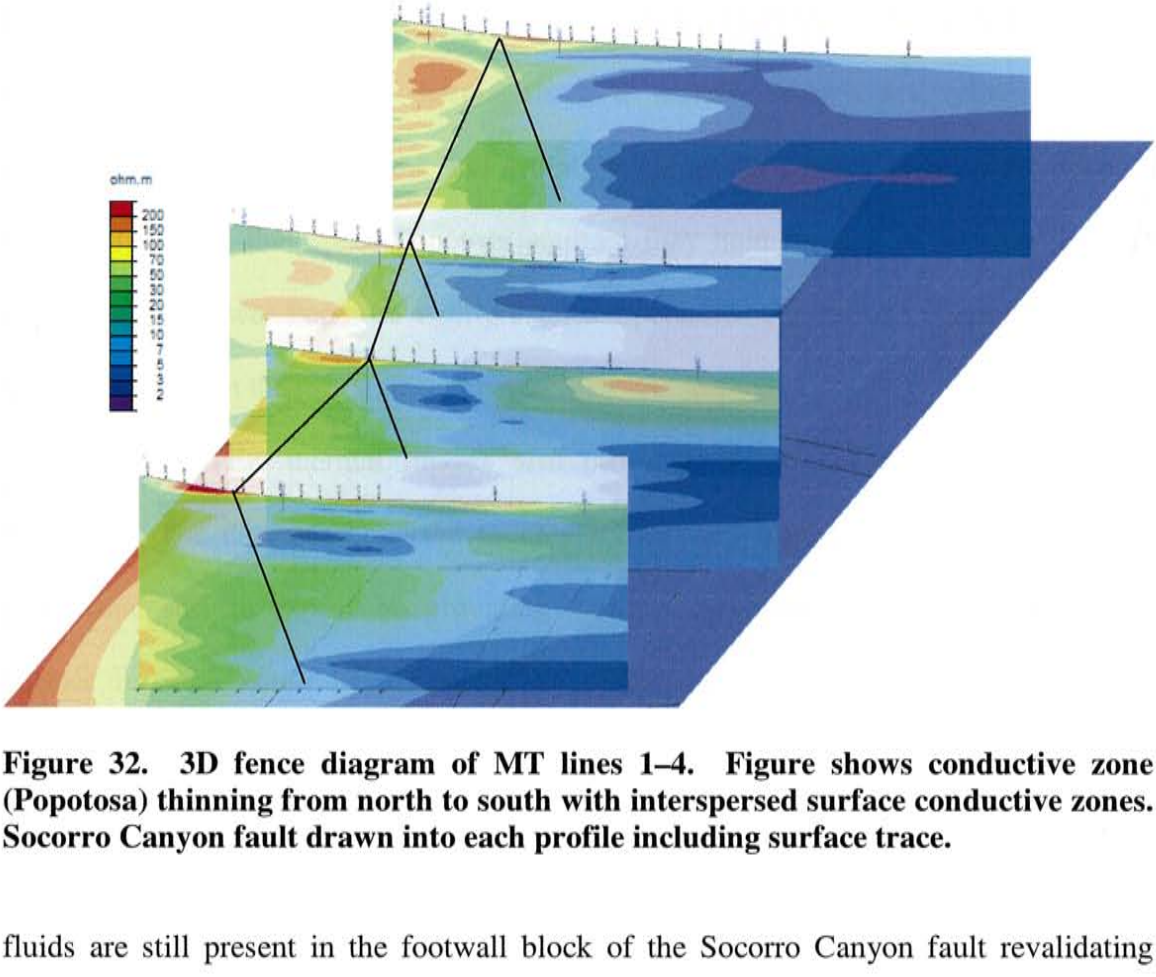

Figure 32. 3D fence diagram of MT lines 1–4. Figure shows conductive zone (Popotosa) thinning from north to south with interspersed surface conductive zones. Socorro Canyon fault drawn into each profile including surface trace.

fluids are still present in the footwall block of the Socorro Canyon fault revalidating previous work by Barroll and Reiter (1990) and others confirming that the heat flow is still present and the Socorro Canyon fault is a boundary for thermal fluid flow. The MT lower then normal resistivity values for the quartzite mountain block coincide with a footwall that is highly fractured and saturated with hydrothermal fluids. It is unconfirmed the extent that the Socorro Canyon fault plays as a thermal fluid flow barrier. The hydrologic models by Mailloux, Gross and Wilcox, and others suggest an unknown communication of basin volumes of fluids traveling to depth in La Jencia Basin, mixing and being heated in the Socorro Peak mountain block and with the only known surface expression of thermal fluids at surface being a few relatively small flowing spring. Continued work and drilling to target the contact between the Socorro Canyon fault and the Upper Popotosa aquitard may hold the key to possible thermal aquifer in the Lower Popotosa with greater temperatures and greater volumes of fluids unaccounted for in the recharge zone.

The ASTER thermal images also prove to be an exciting and worthwhile endeavor. The database collected to date shows very high potential for mapping a geothermal surface expression providing multiple constraints are correctly modeled. Further research could be conducted by purchasing multi-channel thermal images pending preliminary examination of current images. Thermal imagery has been used in many scientific fields from volcanology to natural disaster monitoring an application to geothermal exploration could be a advance for the scientific community and New Mexico Tech.

REFERENCES

Anderholm, S. K., 1983, Hydrogeology of the Socorro and La Jencia basins, Socorro county, New Mexico, Field Conf. Guideb. N. M. Geol. Soc.,34, 303–310.

Anderholm, S.K., 1987, Hydrogeology of the Socorro and La Jencia basins, Socorro County, New Mexico: U.S.G.S. Water Resource Investigations Report 84-4342.

Anderson, R.C., 1955, A gravity survey of the Rio Grande trough near Socorro, New Mexico, Am. Geophys. Union Trans., v. 36, p. 144-148.

Baars, R. M., Owens, L., Tobin, H., Norman, D. I., Cumming, W., and Hill, G. T., 2006, Exploration and targeting of the Socorro, NM direct use geothermal exploration well, a GRED III project: Proceedings, 31st Workshop on Geothermal Reservoir Engineering, Stanford University, SGP-TR-179.

Barroll, M.W., 1989, Analysis of the Socorro hydro-geothermal system, central New Mexico [Masters Thesis]: New Mexico Institute of Mining and Technology, 239 p.

Barroll, M.W. and Reiter,M. 1990, Analysis of the Socorro Hydrogeothermal system: Central New Mexico: J. Geophys. Res., v. 95, p. 21,949-21,963.

Barroll, M.W., 1995, Hydrothermal investigation of the Bosque del Apache, New Mexico: New Mexico Geology, v. 17, p. 1-17.

Brown, L.D et Al, (1980), Deep structure of the Rio Grande rift from seismic reflection profiling: Journal of Geophysical Research, Vol. 85, NO. B9, p. 4773-4800, September 10, 1980.

Chamberlin, R.M., 1999, Preliminary geologic map of the Socorro quadrangle, Socorro County, New Mexico: New Mexico Bureau of Geology and Mineral Resources: Open-file Digital Map Series OF-DM-34, p. 46 (scale 1:24,000).

Chamberlin, R.M., McIntosh, W.C., Eggleston, T.L., ^{40}Ar/^{39}Ar geochronology and eruptive history of eastern sector of the Oligocene Socorro caldera, central Rio Grande rift, New Mexico: New Mexico Bureau of Geology and Mineral Resources: Bulletin 160, 2004.

Chapin, C.E., A.R. Sanford, D.W. White, R.M. Chamberlin, G.R. Osburn, 1979. Geologic Investigation of the Socorro Geothermal Area (N.M. Bur. Mines and Min. Res. Rpt. NMERDI 2-65-2301), 70 p.

Chapin, C.E., R.M. Chamberlin, G.R. Osburn, D.W. White, and A.R. Sanford, 1978, Exploration framework of the Socorro Geothermal Area, New Mexico: Field Guide to

Selected Cauldrons and Mining Districts of the Datil-Mogollon Volcanic Field, Spec. Publi. N.M. Geol. Soc., v. 7, p. 114-129.

Chapin, C.E. 1989. Volcanism Along the Socorro Accommodation Zone, Rio Grande Rift, New Mexico. p.46-57. In C.E. Chapin and J. Zidek (ed.): Field Excursions to Volcanic Terrains in the Western United States, v. 1, N.M. Bur. Mines and Min. Res.

Cordell, L., Composite Residual Total Intensity Aeromagnetic Map of the Socorro Region, New Mexico. U.S. Geological Survey NOAA scientific map series republished: Socorro Region II, New Mexico Geological Society 34th Annual Field Conference. p. 97.

Gross, G.W. and Wilcox R., 1983, Groundwater Circulation in the Socorro Geothermal Area: NMGS Guidebook, 34th Field Conference. p. 311-318.

Hall, F.R., 1963, Springs in the vicinity of Socorro, New Mexico, -in Socorro Region: New Mexico Geol. Soc. Guidebook, 14th Field Conf., p. 160-179.

Hill, G., Norman, D.I., Owens, L.B., 2006, Surface Geochemistry in Exploration for a Buried Geothermal System, Socorro, New Mexico: Proceedings 31st Workshop on Geothermal Reservoir Engineering, Standford University.

Holmes, C.R., 1963, Tritium studies, Socorro springs: New Mexico Geological Society Guidebook 14.

Jiracek, G.R., 1990, Near-surface and topographic distortions in electromagnetic induction: Surveys in Geophysics 11: 163-203.

Keller, G.R. and Cordell, L., 1983, Bouguer gravity anomaly map of New Mexico: National Geophysical Data Center, NOAA in press.

Mailloux, B. J., Person, M., Kelley, S., Dunbar, N., Cather, S., Strayer, L., and Hudleston, P., 1999, Tectonic controls on the hydrogeology of the Rio Grande rift New Mexico: Water Resources Research, v. 35, no. 9, p. 2641-2659.

Morgan, P. et al, 1981, A Groundwater Convection Model for Rio Grande Rift Geothermal Resources: Trans. Geothermal Resour. Counc., v. 5, p. 193-196.

Morrison, H.F., Nichols, E.A., 1997, Mineral Exploration with Natuarl Electromagnetic Fields: Proceedings of Exploration 97: 4th Decennial International Conference on Mineral Exploration, paper 68, p. 527-538.

NASA Jet Propulsion Laboratory., 2007, ASTER Imagery Site, Retrieved 5/2007, from http://asterweb.jpl.nasa.gov/

Pellerin, L. and Hohmann, G.W., 1990, Transient electromagnetic inversion: a remedy for magnetotelluric static shifts: Geophysics, 55, p. 1242-1250.

Pellerin, L., Johnston, J.M., Hohmann, G.W., 1995, A numerical evaluation og electromagnetic methods in geothermal exploration: Geophysics, Vol 61, No. 1, p. 121-130

Reiter, M. and Smith, R., 1977, Subsurface Temperature Data in the Socorro Peak KGRA, New Mexico: Geothermal Energy Magazine, v. 5, p. 37-42.

Reiter, M., Shearer, C.L., Edwards, C.L., 1978, Geothermal Anomalies along the Rio Grande rift in New Mexico: Geology, v. 6, p. 85-88.

Reiter, M. 2005, Possible Ambiguities in Subsurface Temperature Logs: Consideration of Ground-water Flow and Ground Surface Temperature Change: Pure and Applied Geophysics, v. 162, p. 343-355.

Reiter, M., 2005, Subsurface temperatures and crustal strength changes within the seismogenic layer at Arroyo del Coyote in the Socorro seismic area, central Rio Grande rift, New Mexico: GSA Bulletin, v. 177, p. 307-318.

Reynolds, J.M., 1998, An Introduction to Applied and Environmental Geophysics, John Wiley and Sons Inc.

Sanford, A.R., 1968, Gravity Survey in Central Socorro County, New Mexico: SBMMR Circlular 91.

Sanford, A.R., 1977, Temperature gradient and heat-flow measurements in the Socorro, New Mexico area, 1965-1968: New Mexico Institute of Mining and Technology, Geoscience Dept. Open-File Rep. 15, 19p.

Sanford, A. R., et al., 1977a, Geophysical evidence for a magma body in the crust in the vicinity of Socorro, NM: Am. Geophys. Union Monograph 20, p. 385-403.

Simpson, F. and Bahr, K., 2005, Practical Magnetotellurics, Cambridge: Cambridge University Press.

Sternberg, B.K., Washburne, J.C., and Pellerin, L., 1988, Correction for the static shift in magnetotellurics using transient electromagnetic soundings: Geophysics, 53, p. 1459-1468.

Summers, W.K., 1976, Catalog of Thermal Waters in New Mexico: New Mexico Bureau of Mines and Mineral Resources Hydrologic Report 4. p. 44-51.

Telford, W.M., Geldart, L.P., Sheriff, R.E., and Keys, D.A. (1990) Applied Geophysics, 2nd edn. Cambridge: Cambridge University Press.

Vozoff, K. 1991, The magnetotelluric method, in Nabighian, M.N., Ed., Electromagnetic method in applied geophysics, Vol II: Soc. Expl. Geophysics., p. 641-771

Wannamaker, P.E., 2004, Magnetotelluric surveying and monitoring at the Coso geothermal area, California, in support of the enhanced geothermal systems concept: surveying parameter and initial results: Proceedings, 29th Workshop on Geothermal Reservoir Engineering, Stanford University, SGP-TR-175.

Witcher, J.C., 1988, Geothermal resources of southwestern New Mexico and southeastern Arizona: Field Conf. Guideb. N.M. ~1. Soc., 39, p. 191-197.

Witcher, J., Owens, L., 2007, GRED III Drilling of New Mexico Tech Well NMT-4-67T, Socorro, NM, US Dept of Energy contract DE-FG36-04GO14342 Phase II Drilling Report, p. 20.

Wright, P.M., Ward, S.H., Ross, H.P. and West, R.C., 1985, State of the art geophysical exploration for geothermal resources, Geophysics, 50, 2666-2696.

Orange, A.S., 1989, Magnetotelluric exploration for hydrocarbons: Proceedings of the IEEE, Vol. 77, No. 2, February 1989.

APPENDIX A. 2D MT TE and TM Pseudosections, resistivity profile, and phase profile.

A.

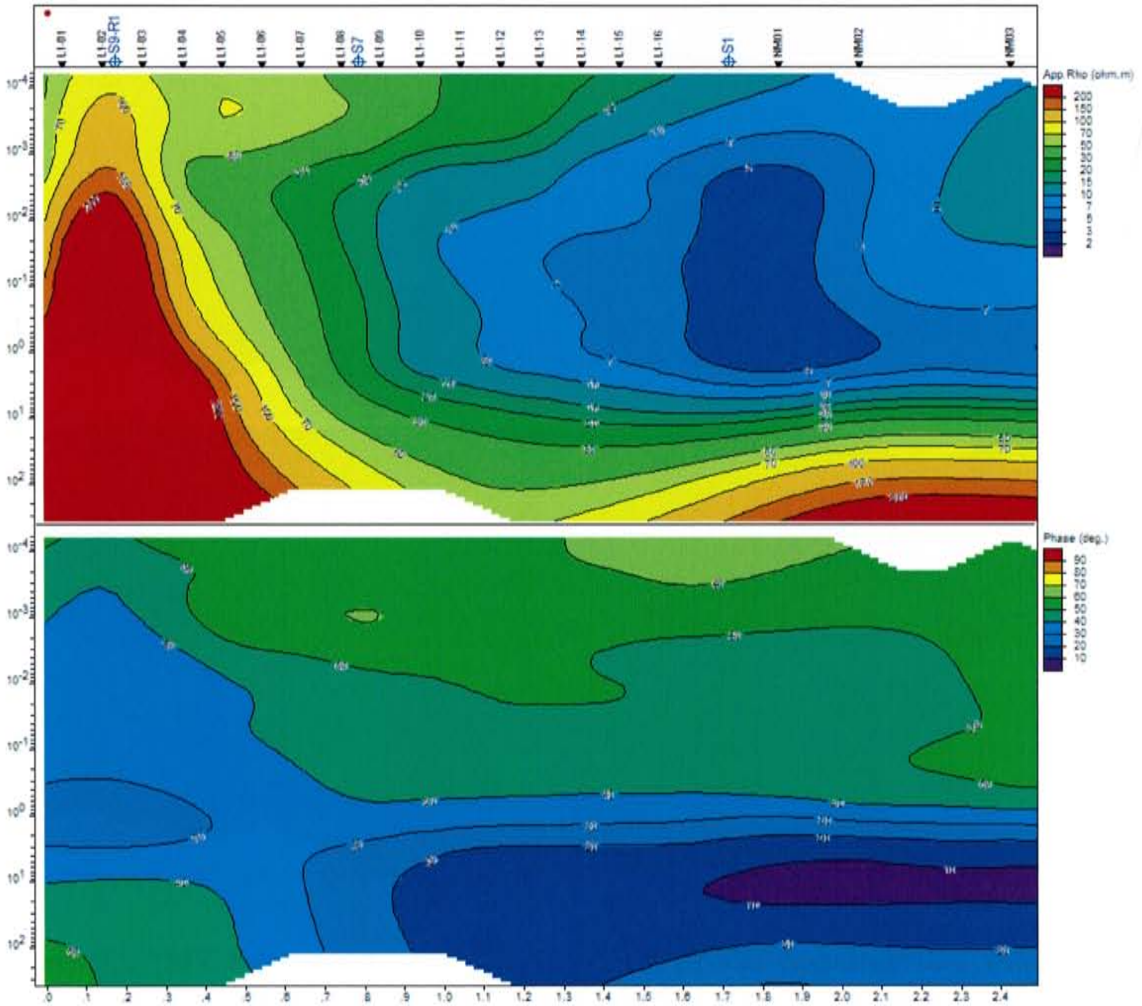

Figure 33. MT survey data on Line 1. (a) TE profile pseudosection with phase. (b) TM profile pseudosection with phase. Color scale is resistivity in Ohm-m. Vertical scale is period in seconds.

B.

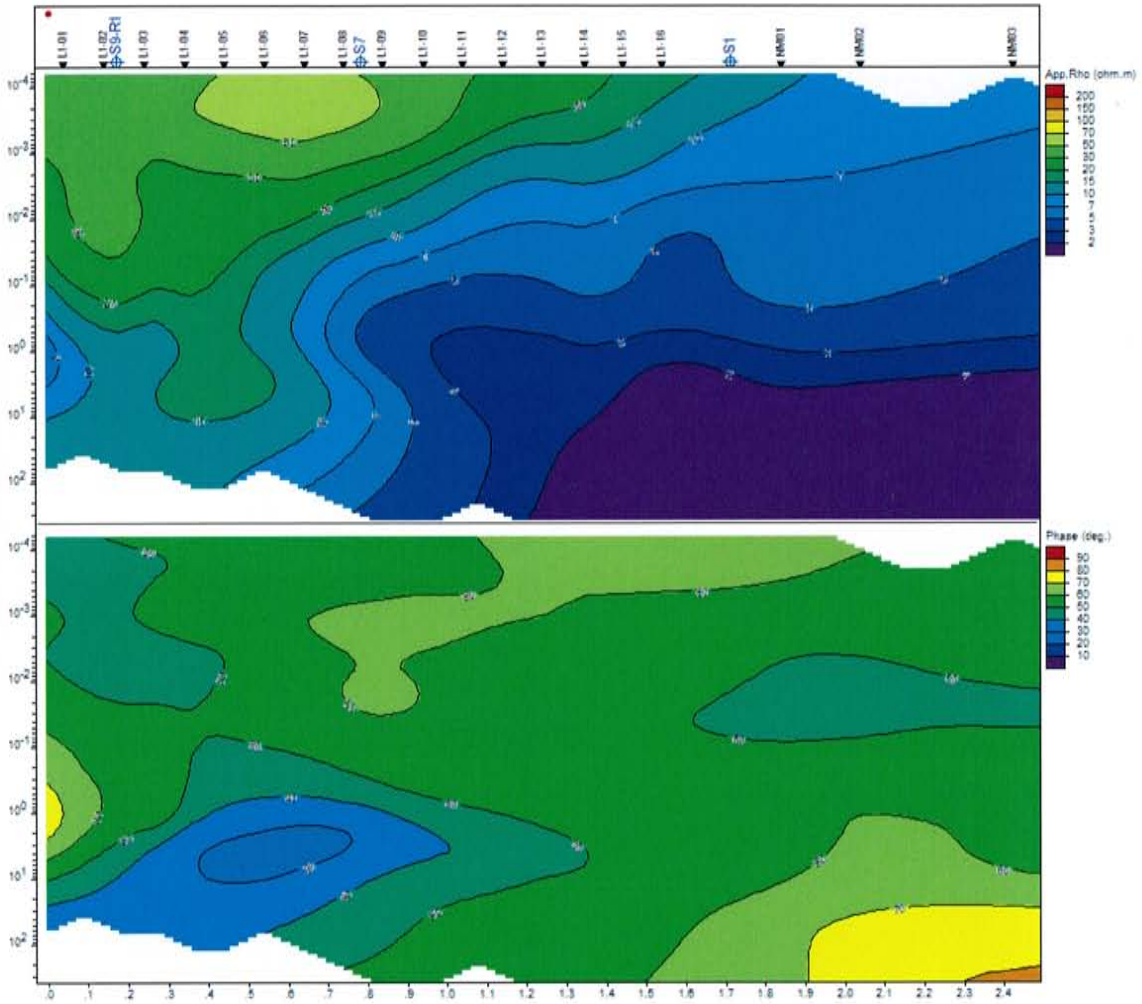

Figure 33. MT survey data on Line 1. (a) TE profile pseudosection with phase. (b) TM profile pseudosection with phase. Color scale is resistivity in Ohm-m. Vertical scale is period in seconds.

A.

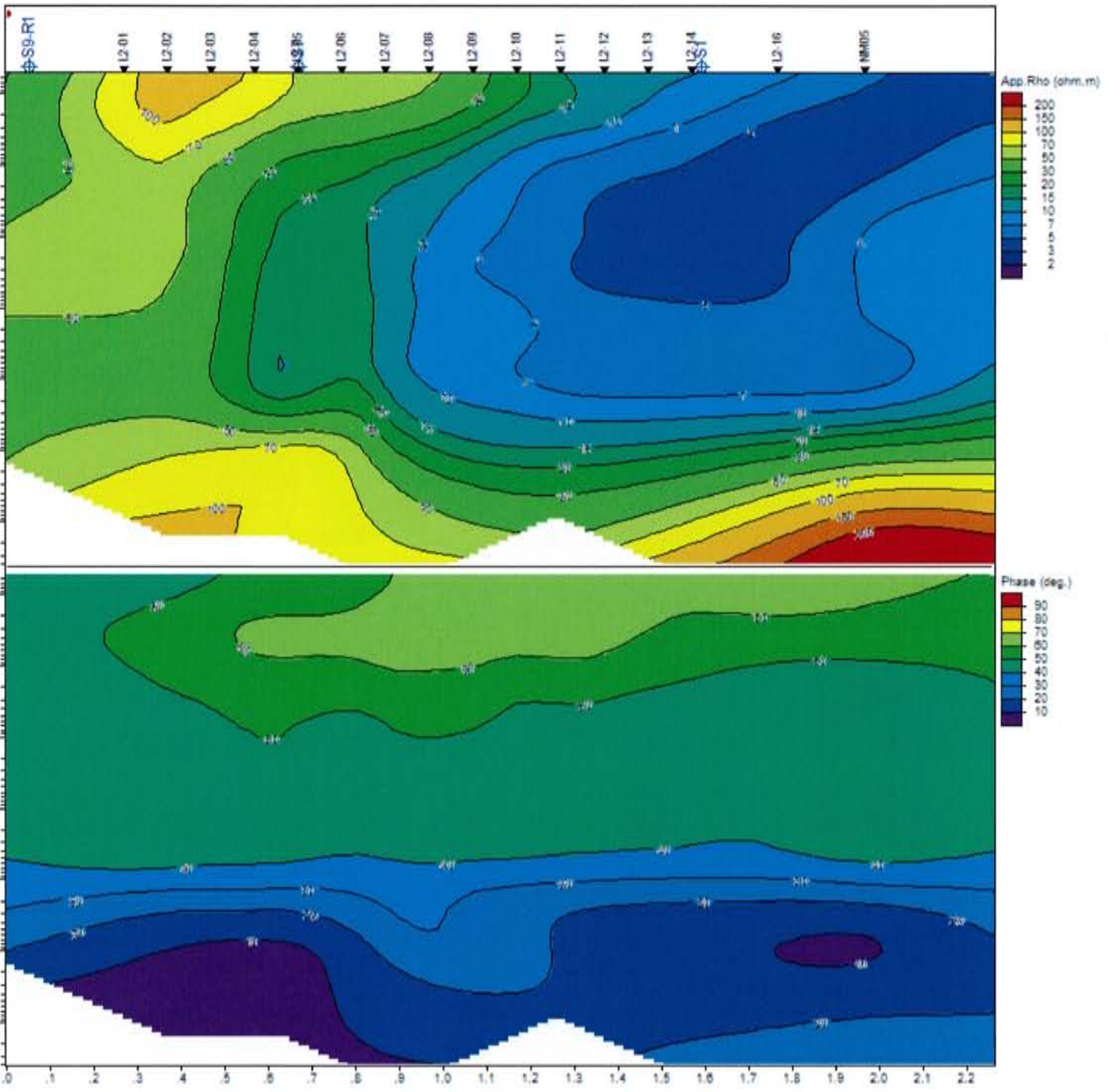

Figure 34. MT survey data on Line 2. (a) TE profile pseudosection with phase. (b) TM profile pseudosection with phase. Color scale is resistivity in Ohm-m. Vertical scale is period in seconds.

B.

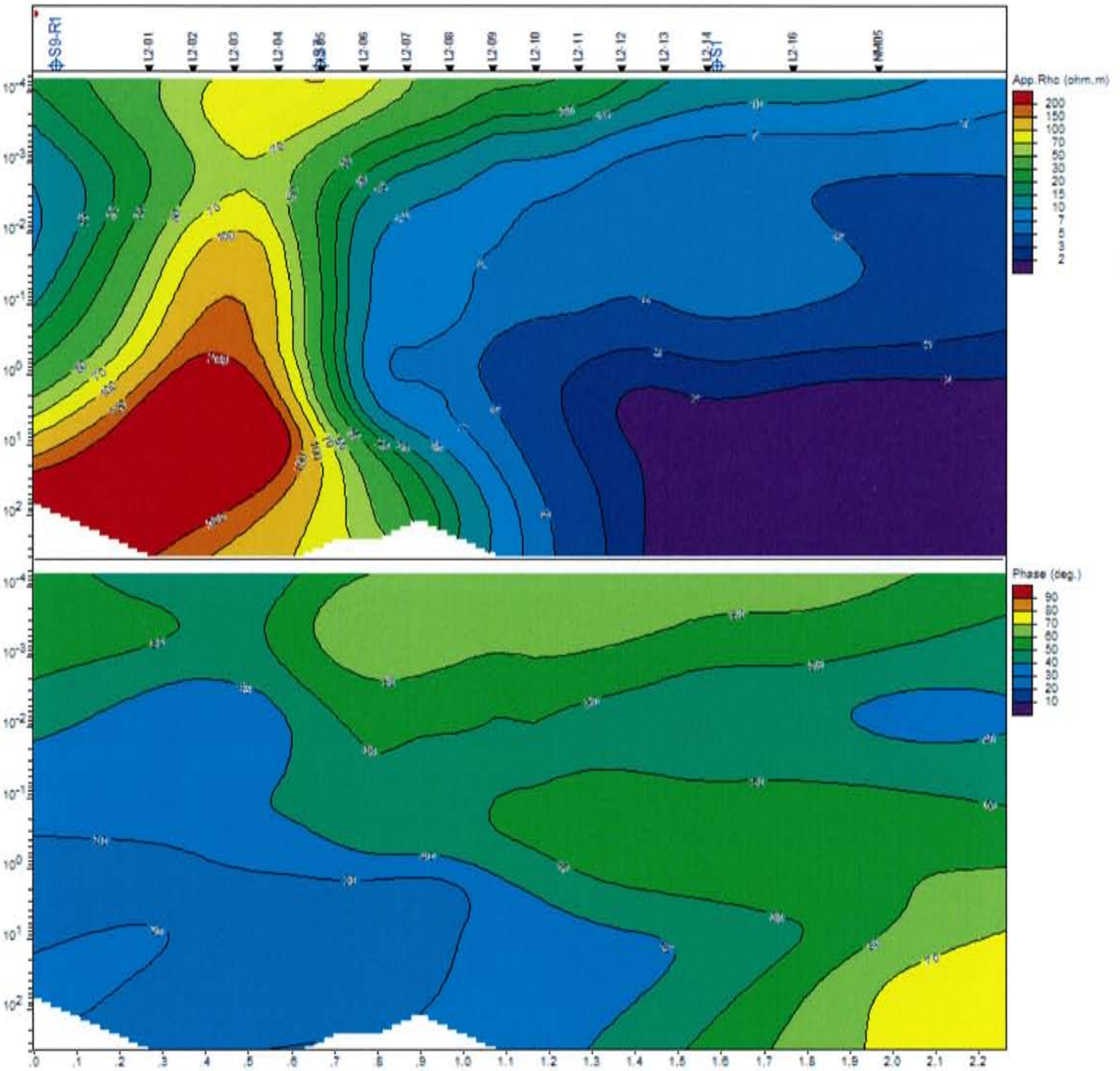

Figure 34. MT survey data on Line 2. (a) TE profile pseudosection with phase. (b) TM profile pseudosection with phase. Color scale is resistivity in Ohm-m. Vertical scale is period in seconds.

A.

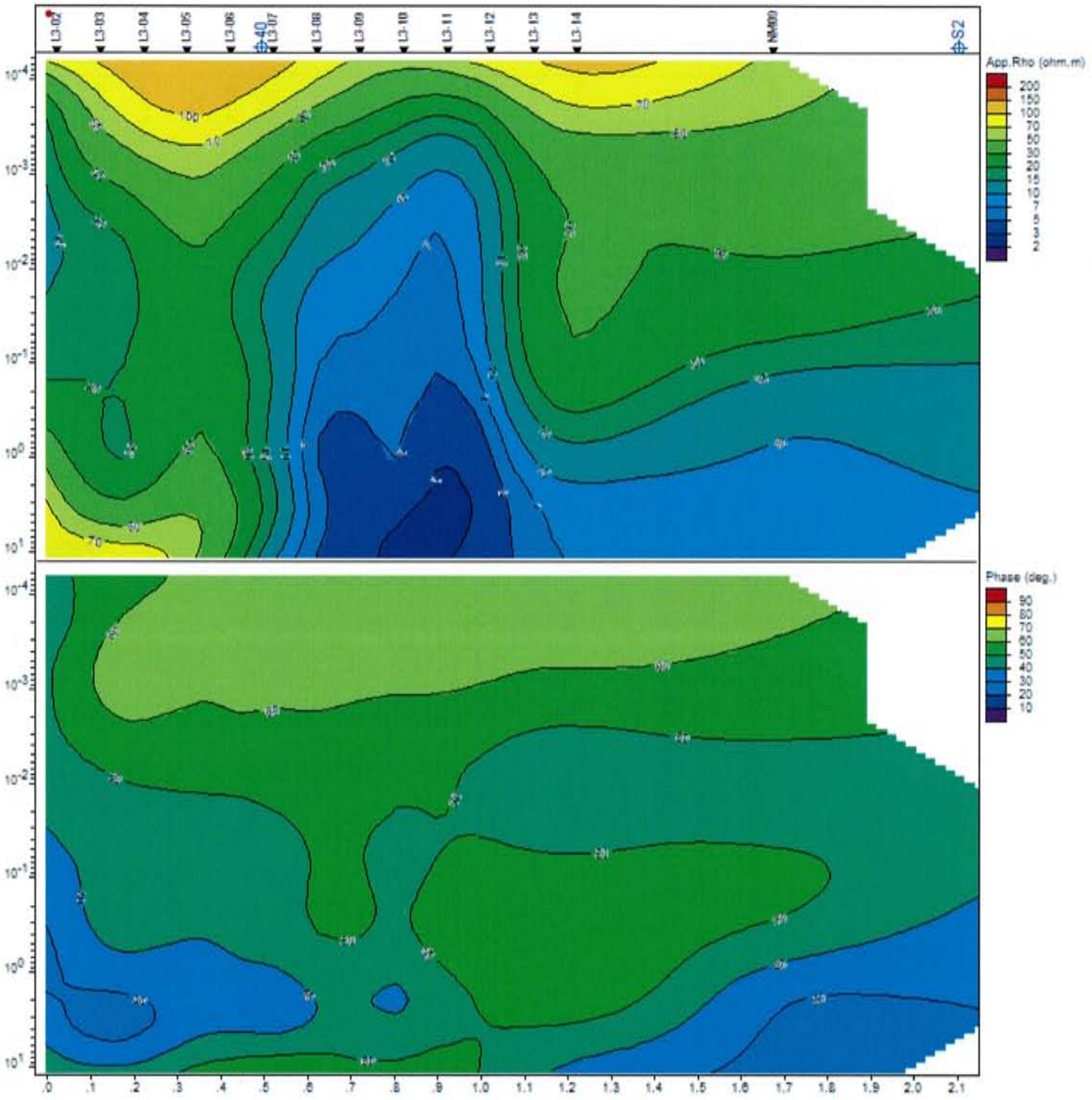

Figure 35. MT survey data on Line 3. (a) TE profile pseudosection with phase. (b) TM profile pseudosection with phase. Color scale is resistivity in Ohm-m. Vertical scale is period in seconds.

B.

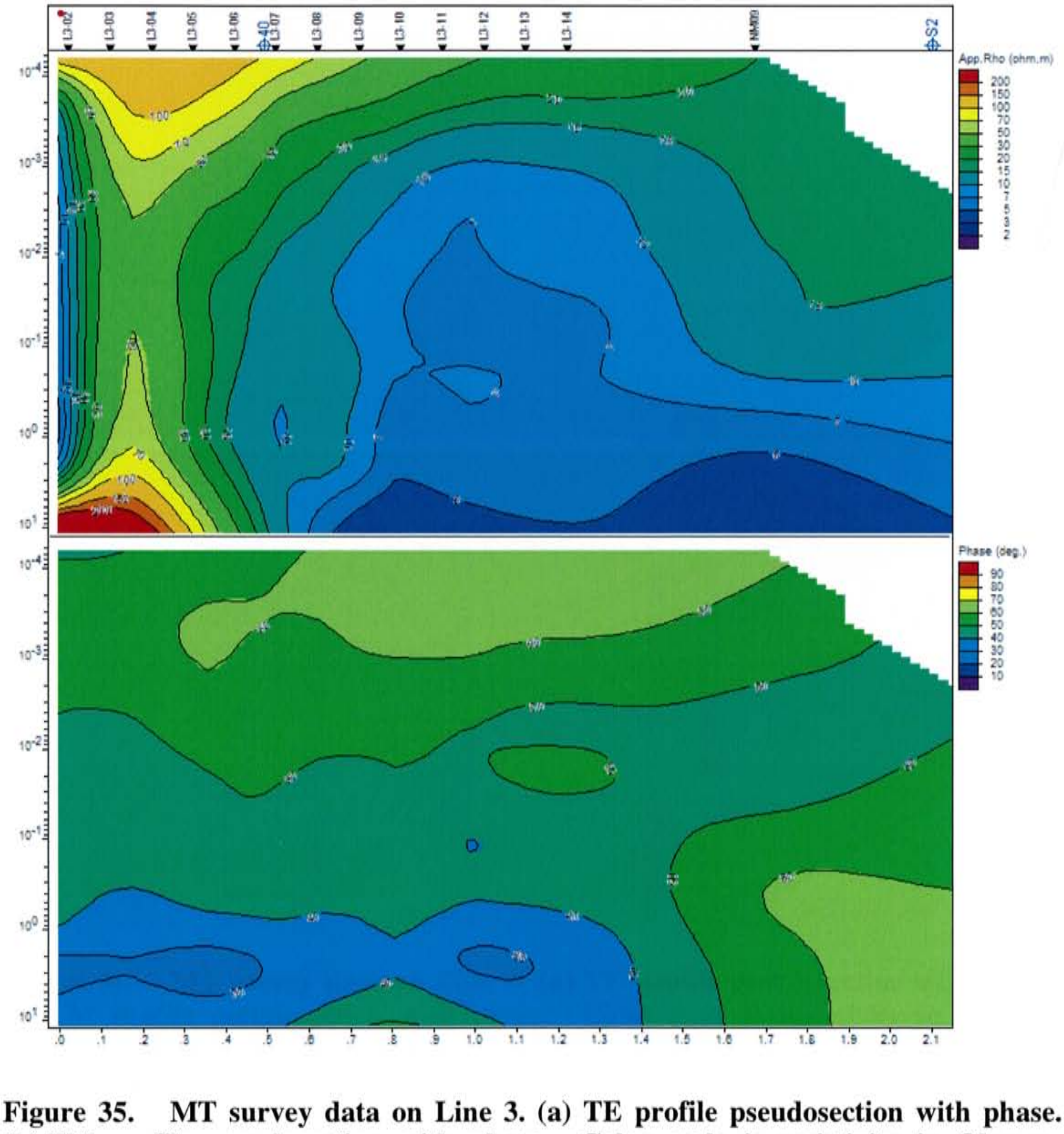

Figure 35. MT survey data on Line 3. (a) TE profile pseudosection with phase. (b) TM profile pseudosection with phase. Color scale is resistivity in Ohm-m. Vertical scale is period in seconds.

A.

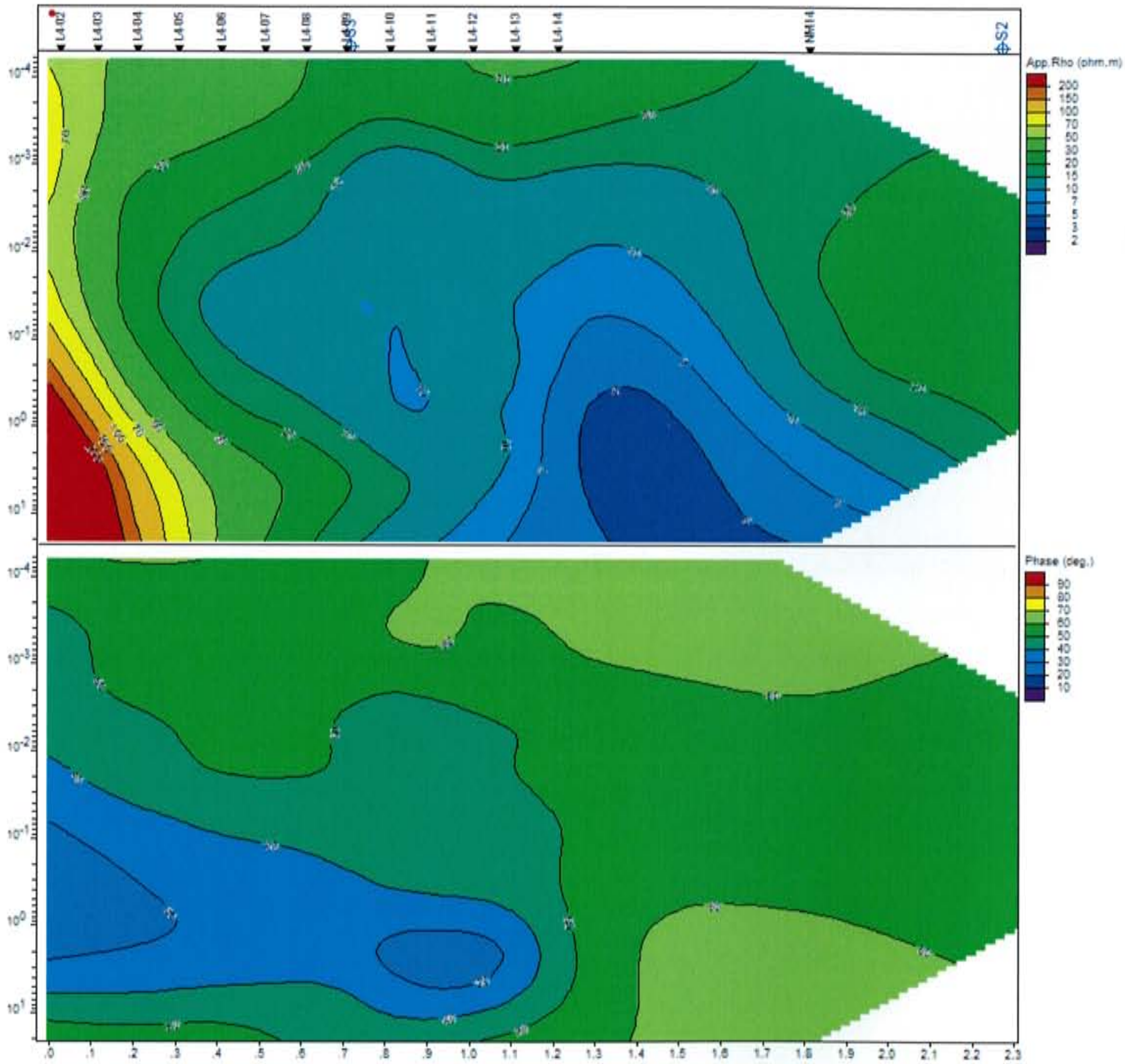

Figure 36. MT survey data on Line 4. (a) TE profile pseudosection with phase. (b) TM profile pseudosection with phase. Color scale is resistivity in Ohm-m. Vertical scale is period in seconds.

B.

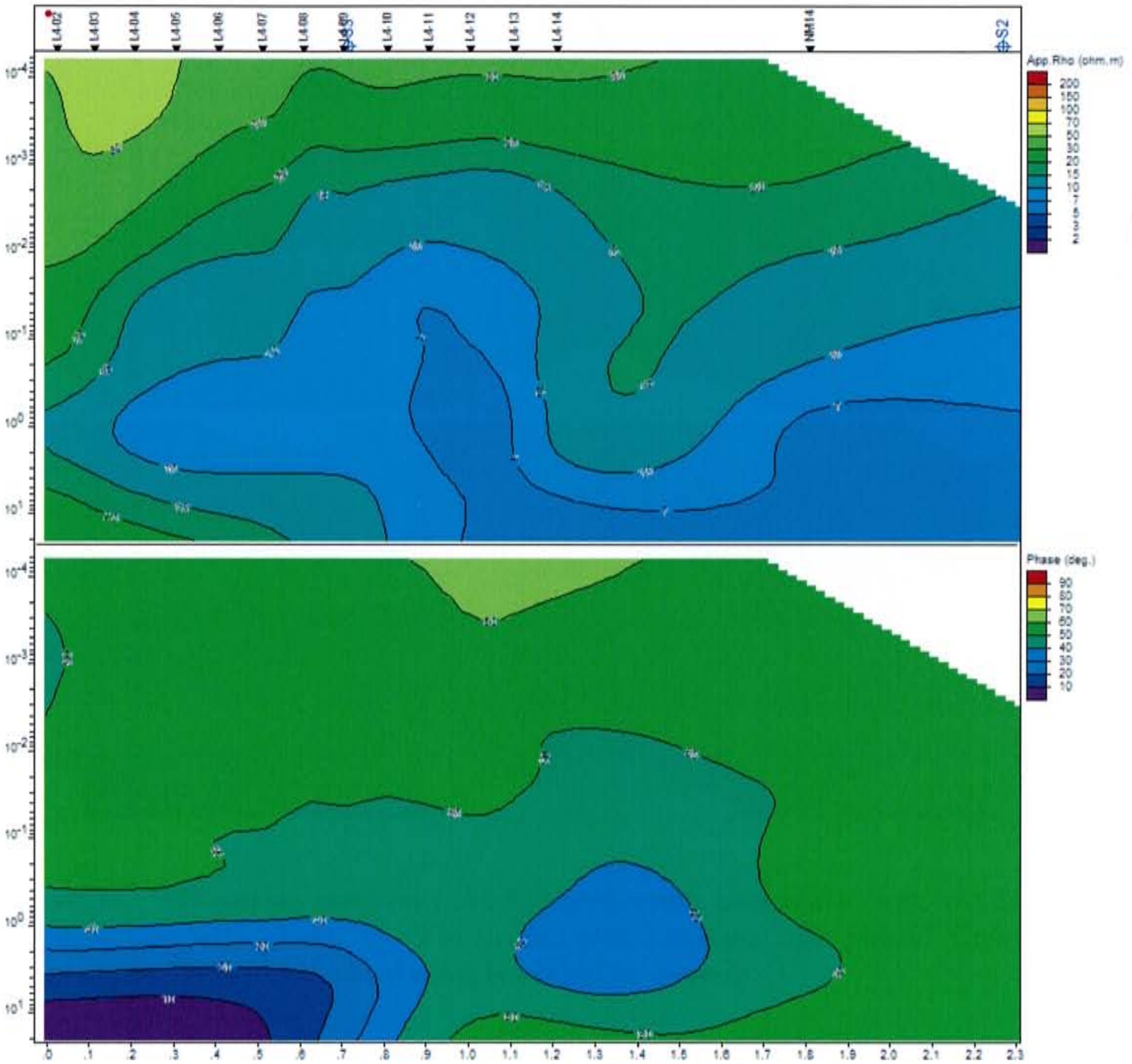

Figure 36. MT survey data on Line 4. (a) TE profile pseudosection with phase. (b) TM profile pseudosection with phase. Color scale is resistivity in Ohm-m. Vertical scale is period in seconds.

A.

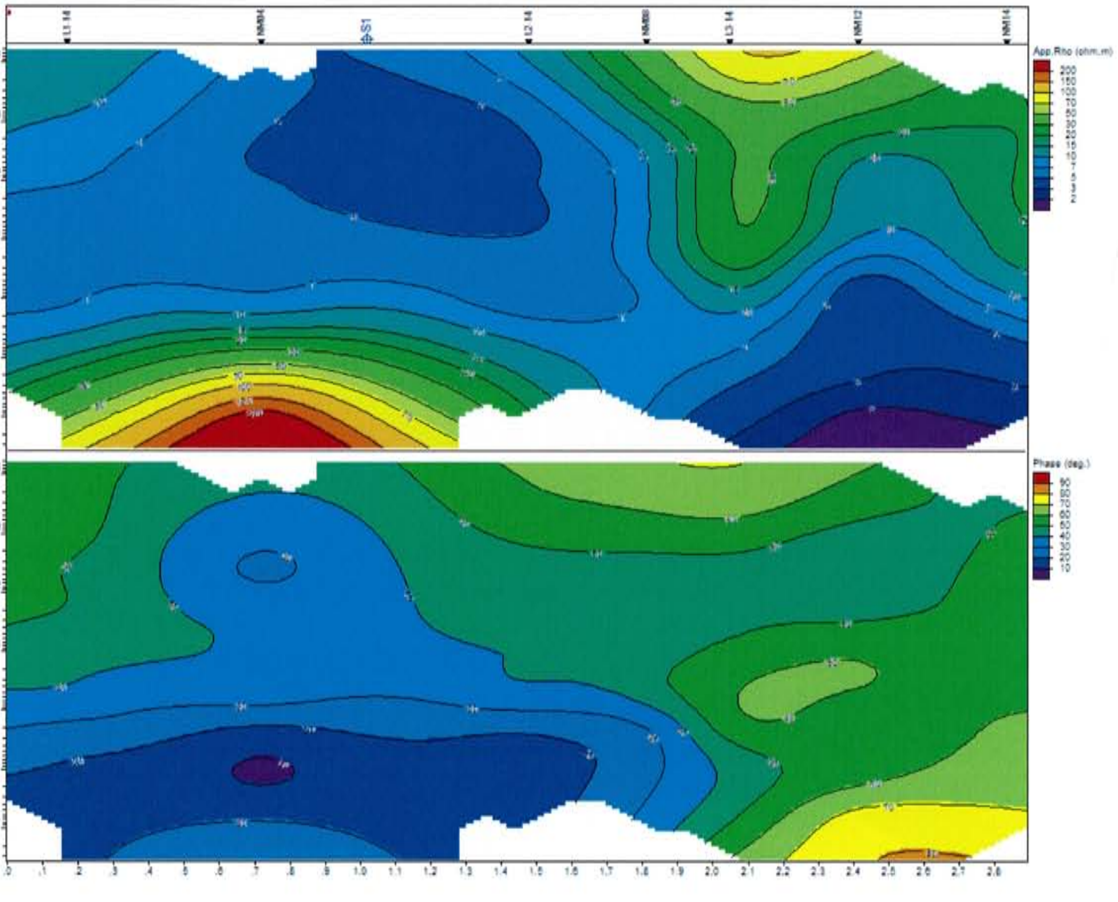

Figure 37. MT survey data on Line 5 (North-south composite line). (a) TE profile pseudosection with phase. (b) TM profile pseudosection with phase. Color scale is resistivity in Ohm-m. Vertical scale is period in seconds.

B.

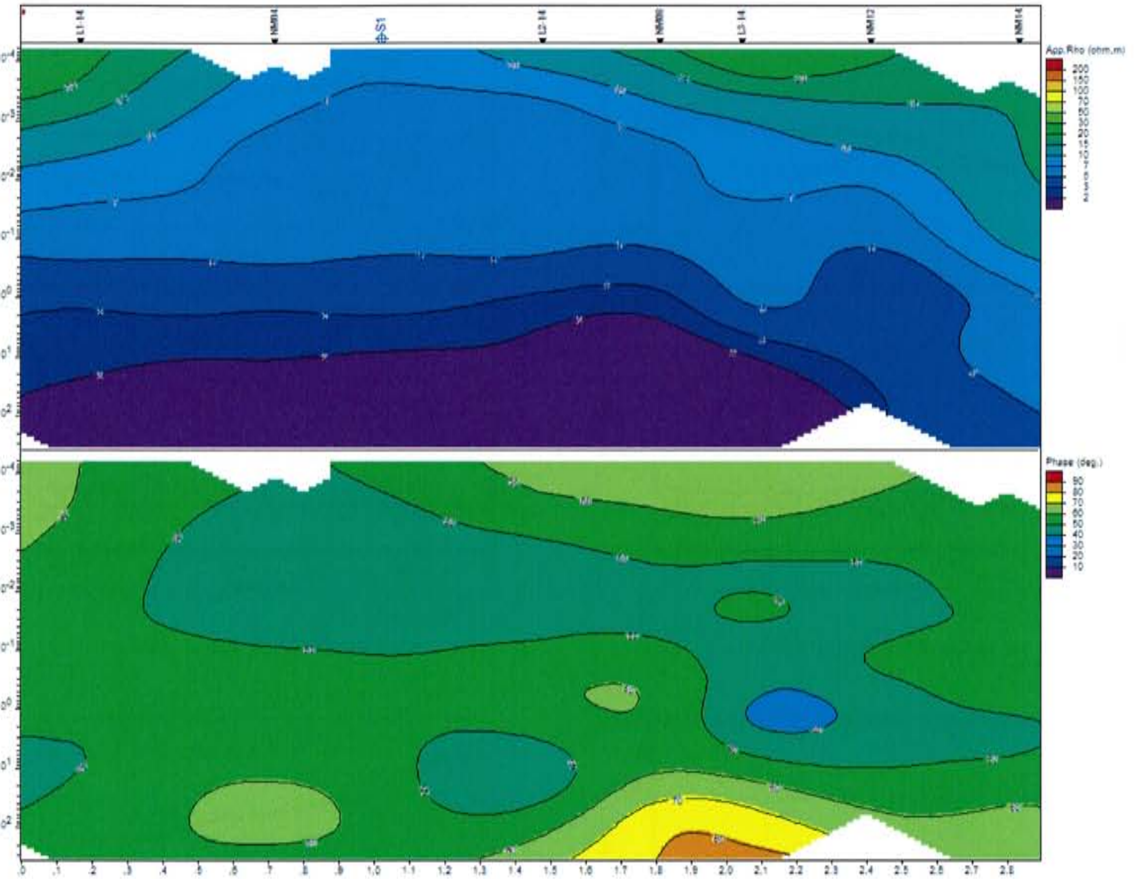

Figure 37. MT survey data on Line 5 (North-south composite line). (a) TE profile pseudosection with phase. (b) TM profile pseudosection with phase. Color scale is resistivity in Ohm-m. Vertical scale is period in seconds.

Appendix B. Magnetotelluric Data, smoothed model fit, phase plots, and polar diagrams. Red (XY) and Blue (YX).

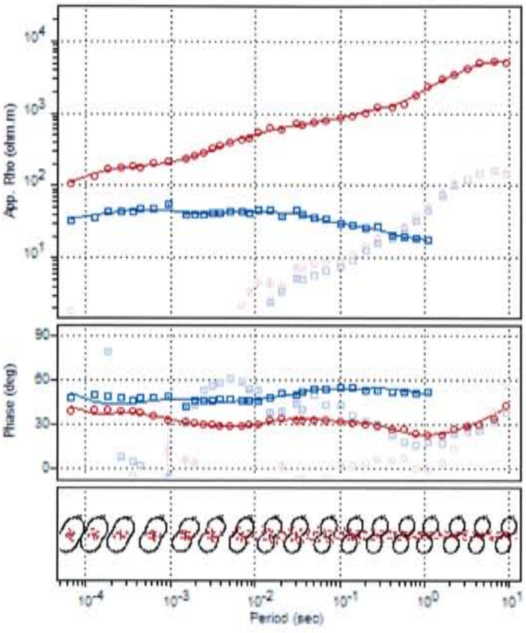

MT Line 1 Station 1

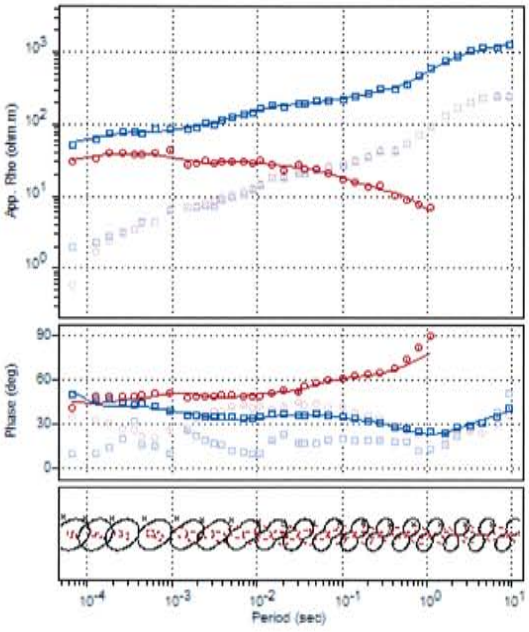

MT Line 1 Station 2

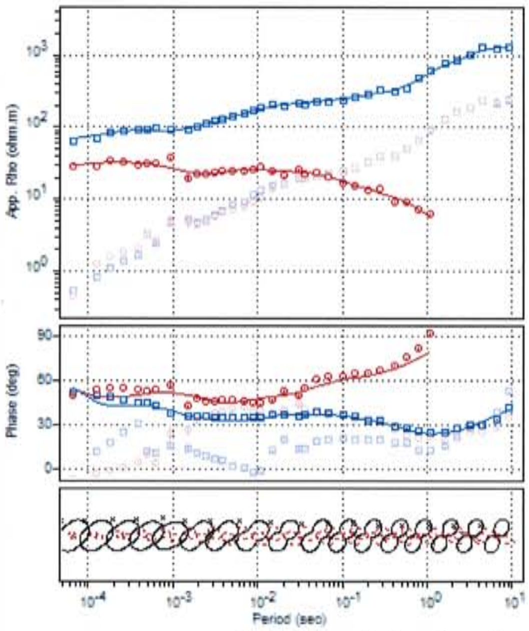

MT Line 1 Station 4

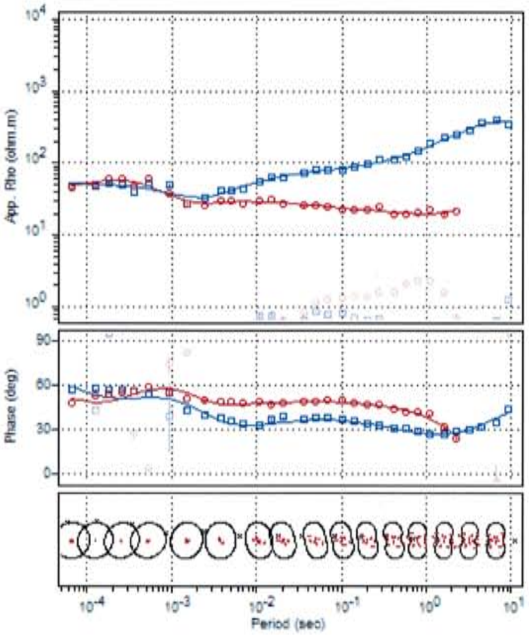

MT Line 1 Station 3

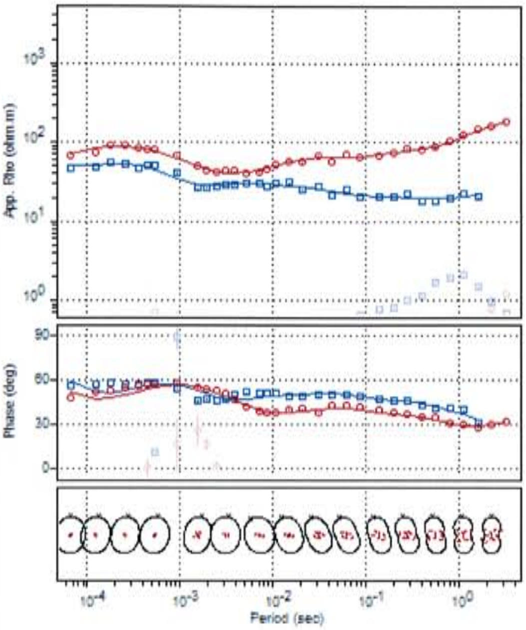

MT Line 1 Station 5

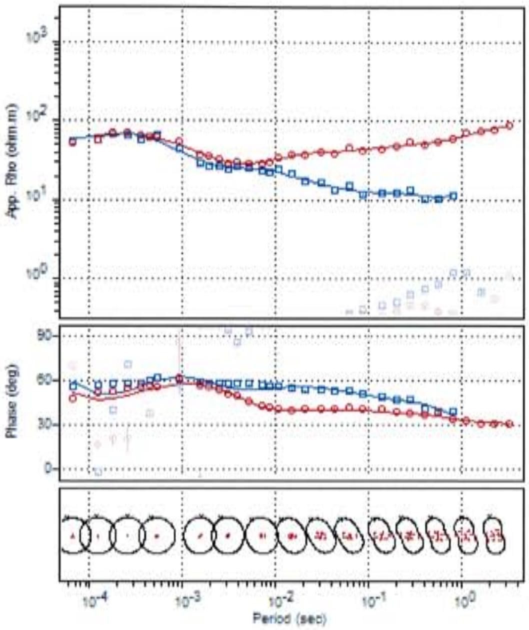

MT Line 1 Station 6

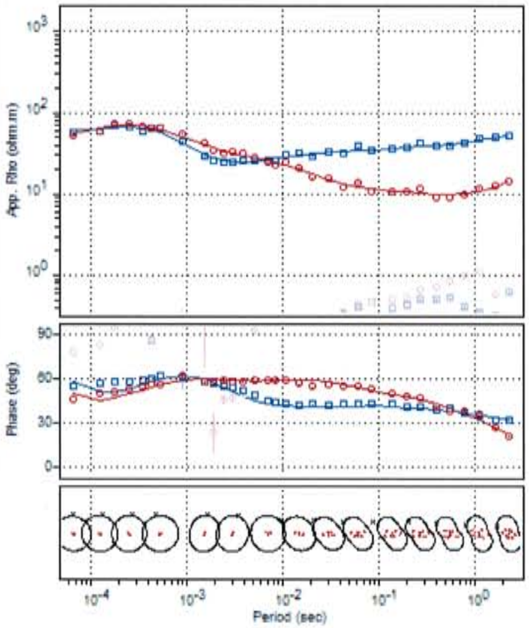

MT Line 1 Station 7

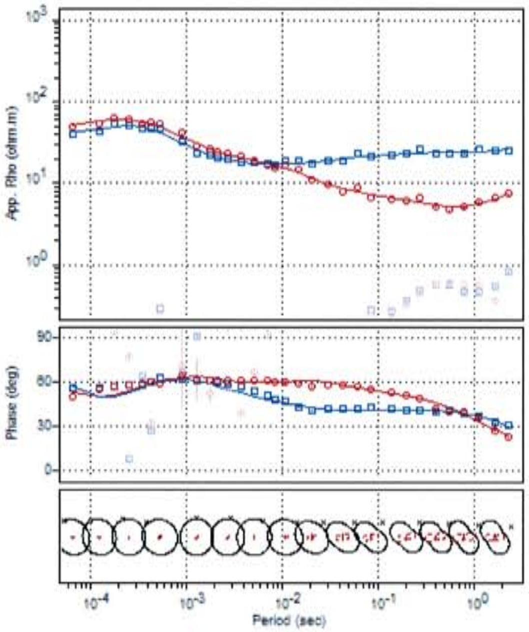

MT Line 1 Station 8

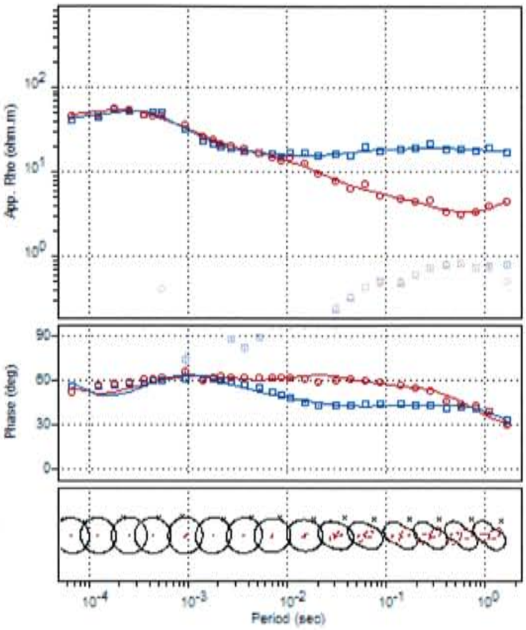

MT Line 1 Station 9

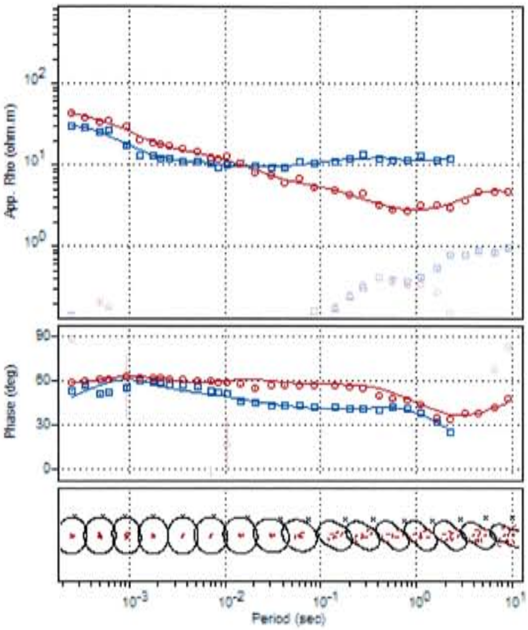

MT Line 1 Station 10

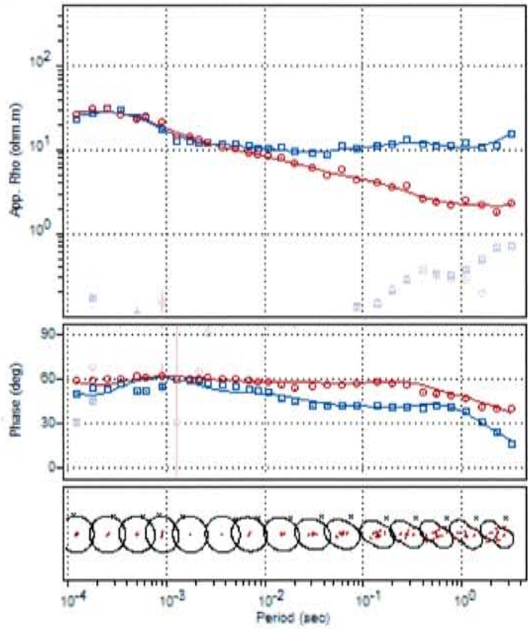

MT Line 1 Station 11

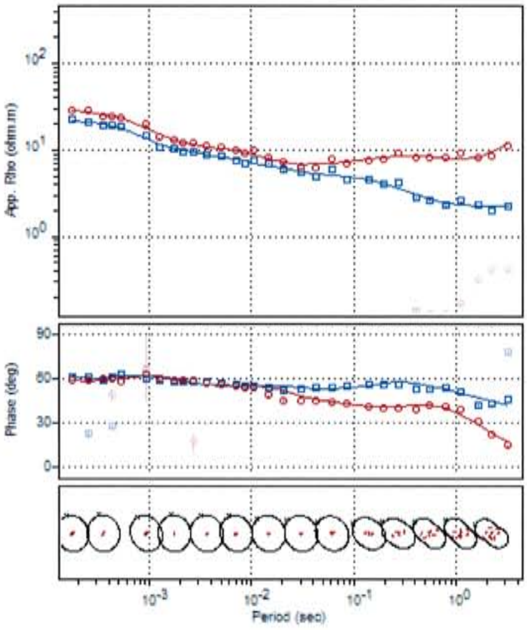

MT Line 1 Station 12

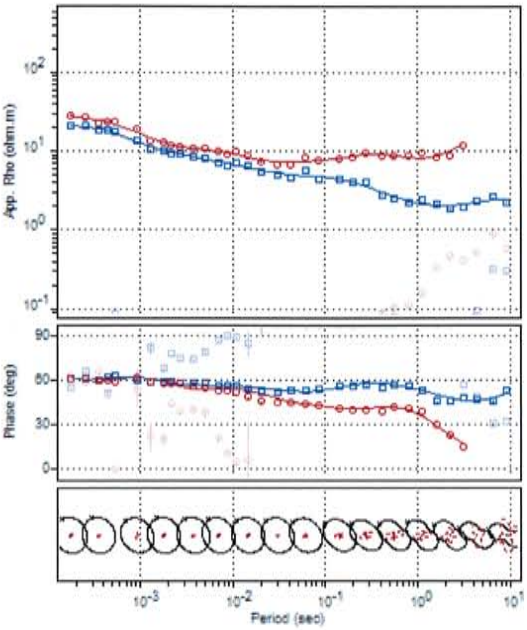

MT Line 1 Station 13

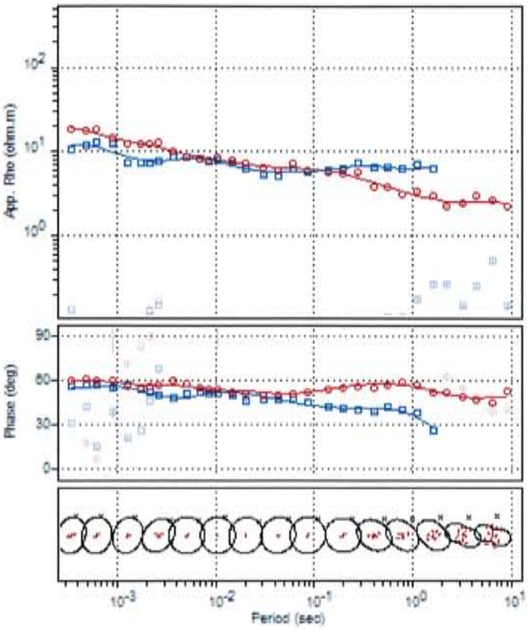

MT Line 1 Station 14

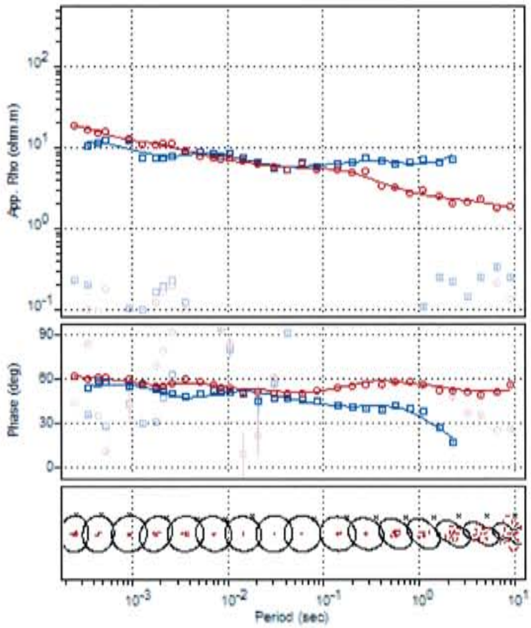

MT Line 1 Station 15

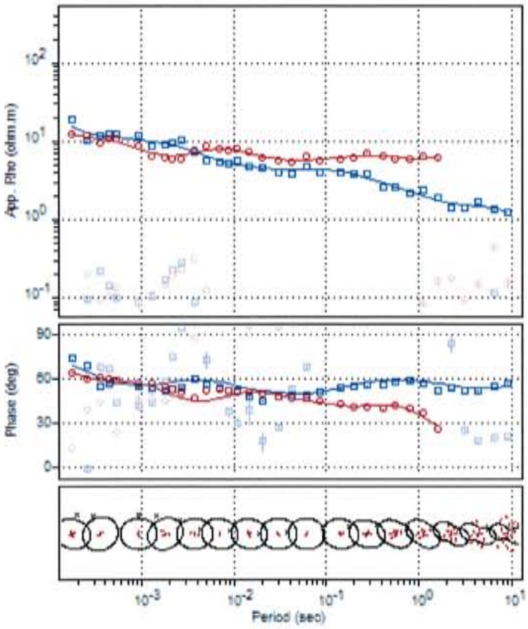

MT Line 1 Station 16

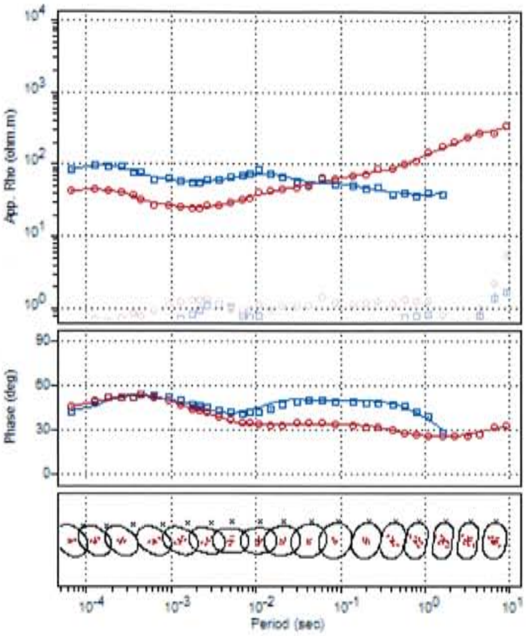

MT Line 2 Station 1

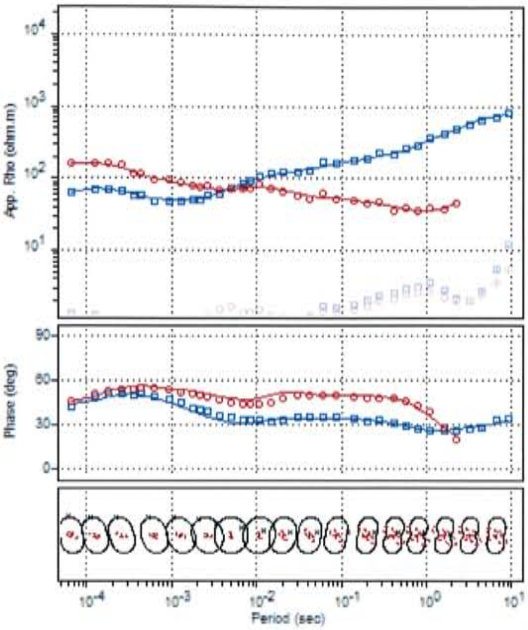

MT Line 2 Station 2

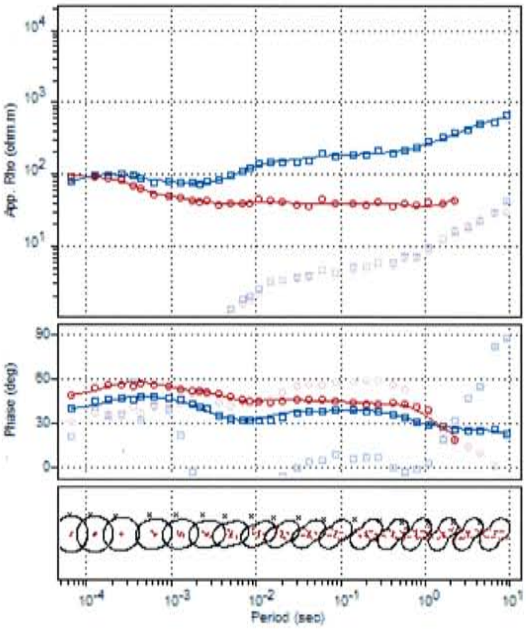

MT Line 2 Station 3

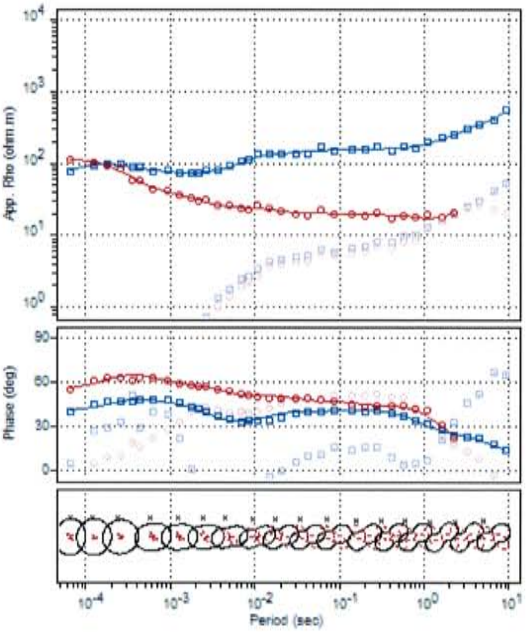

MT Line 2 Station 4

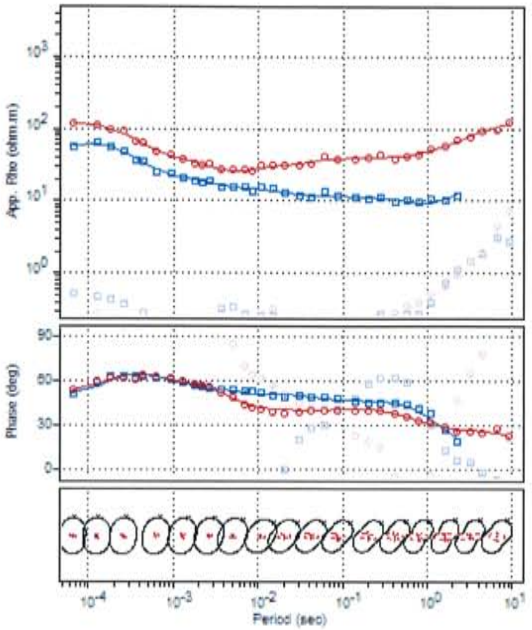

MT Line 2 Station 5

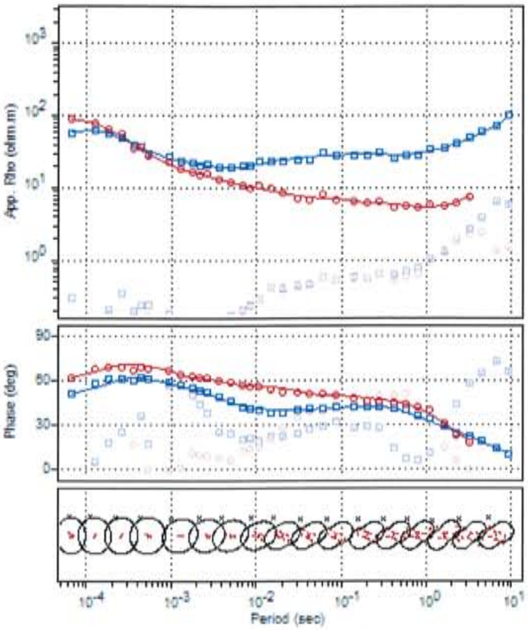

MT Line 2 Station 6

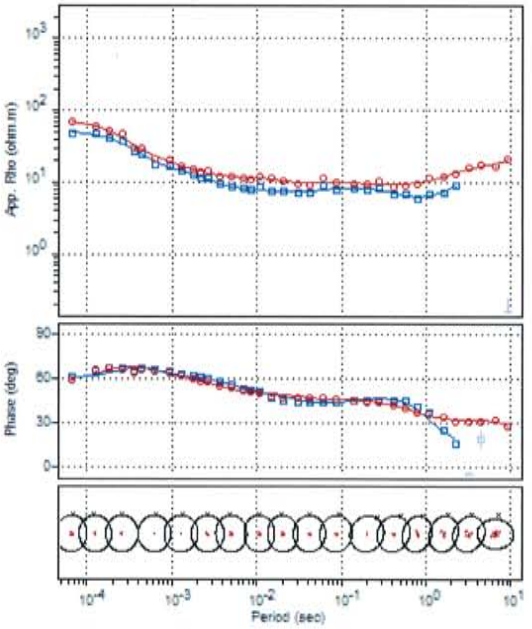

MT Line 2 Station 7

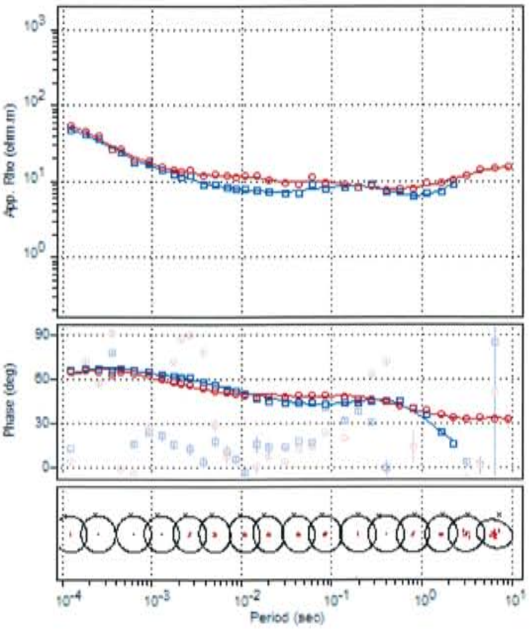

MT Line 2 Station 8

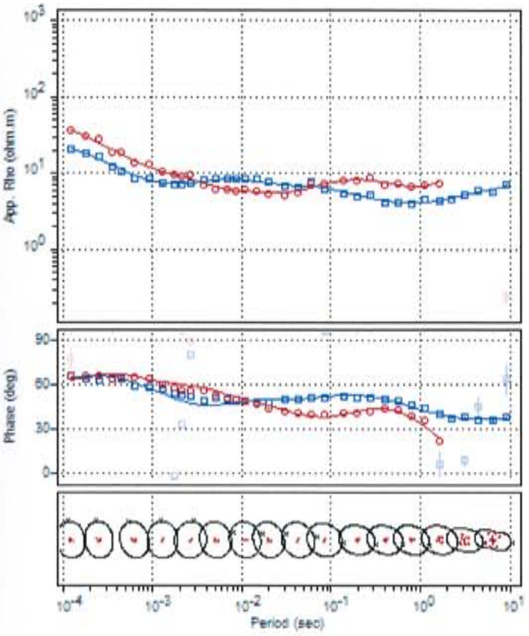

MT Line 2 Station 9

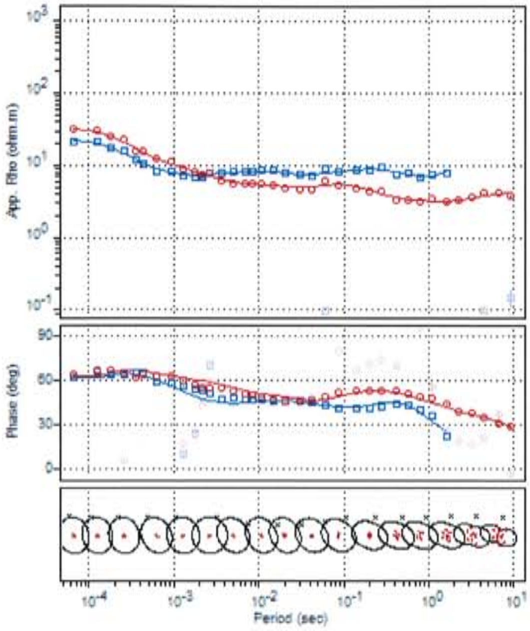

MT Line 2 Station 10

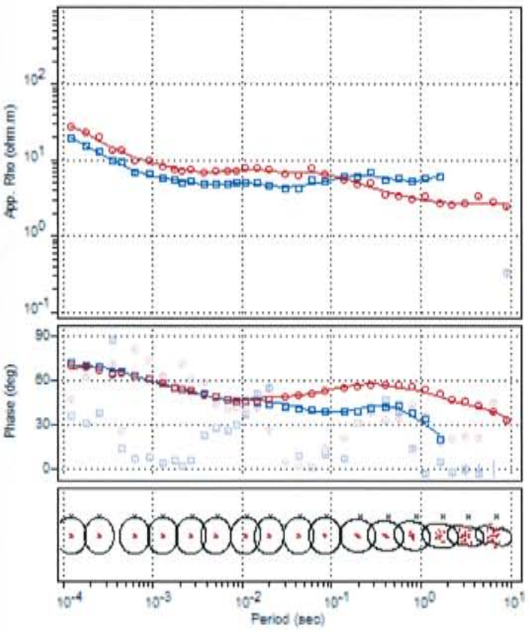

MT Line 2 Station 11

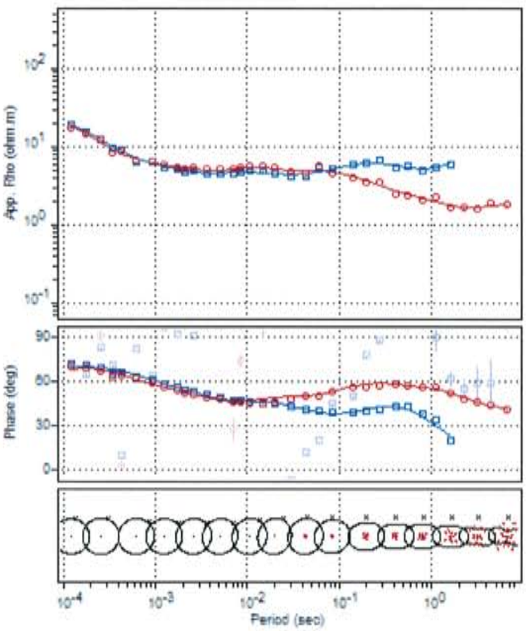

MT Line 2 Station 12

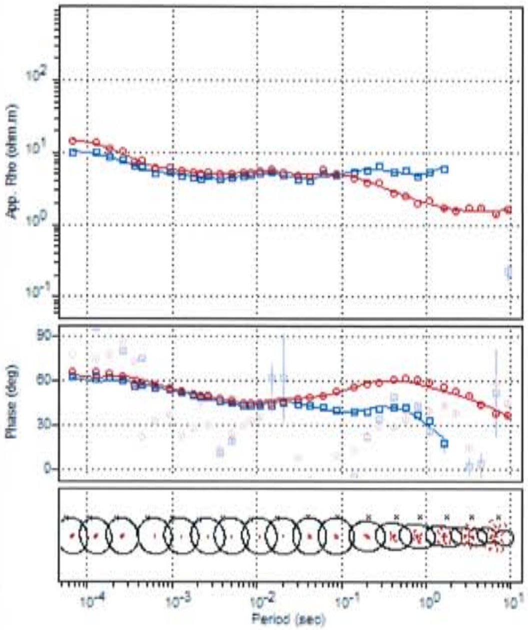

MT Line 2 Station 13

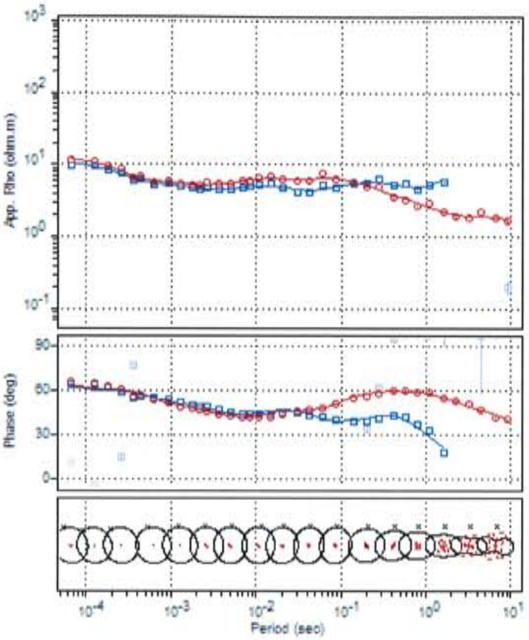

MT Line 2 Station 14

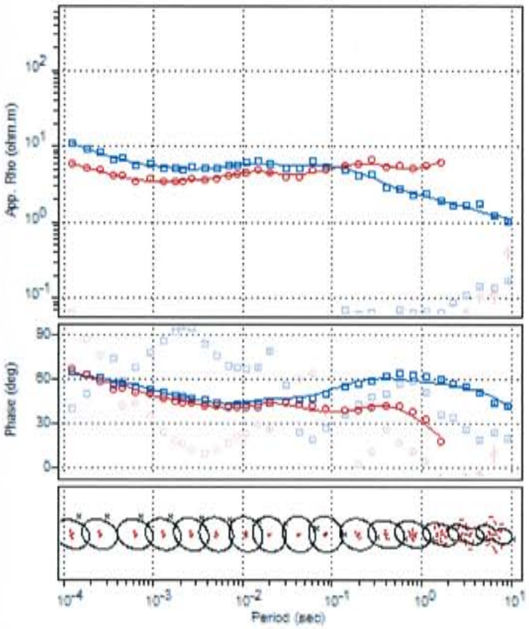

MT Line 2 Station 16

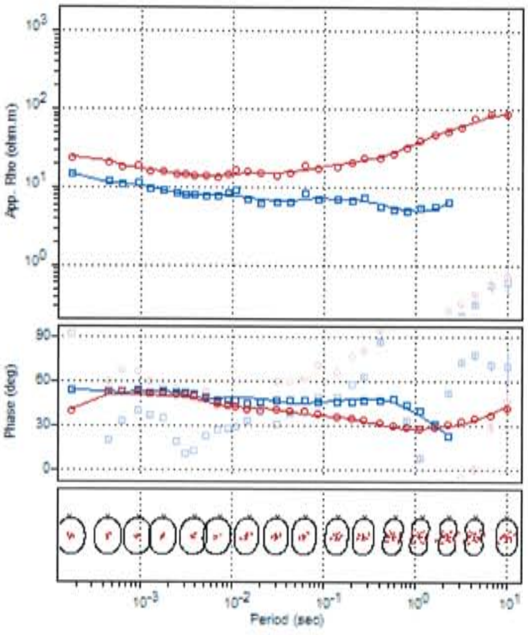

MT Line 3 Station 2

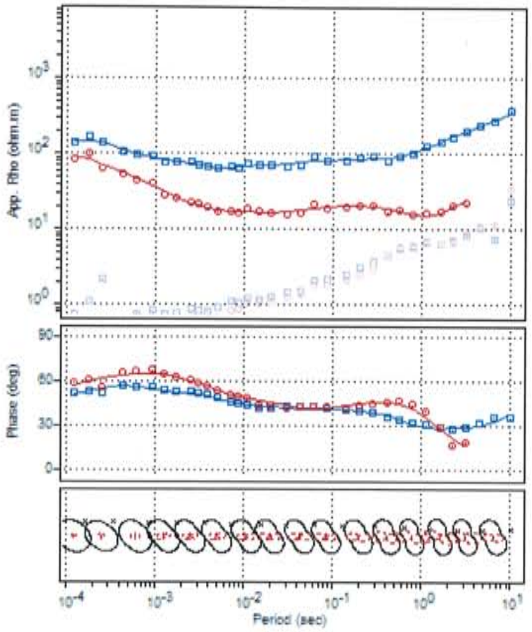

MT Line 3 Station 3

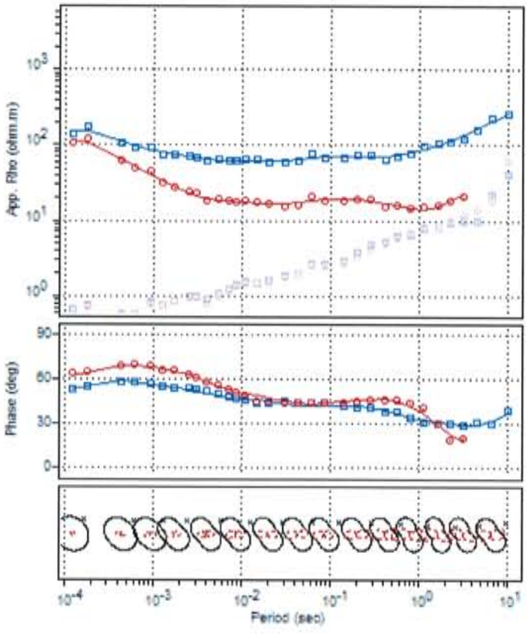

MT Line 3 Station 4

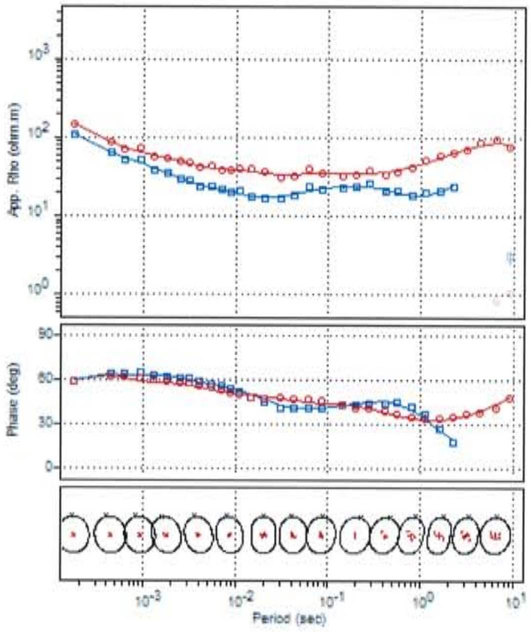

MT Line 3 Station 5

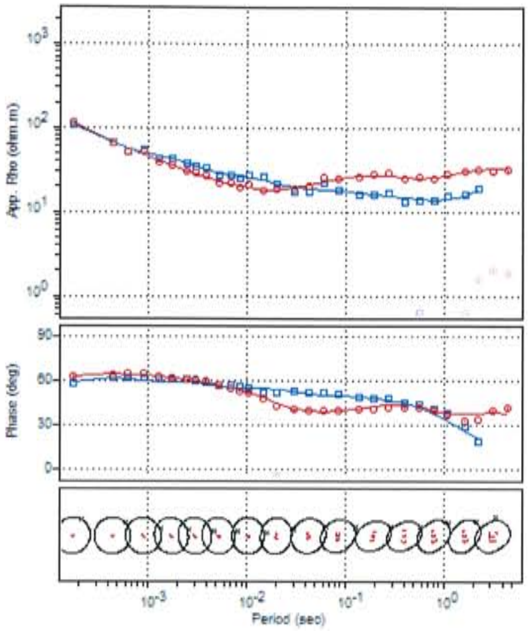

MT Line 3 Station 6

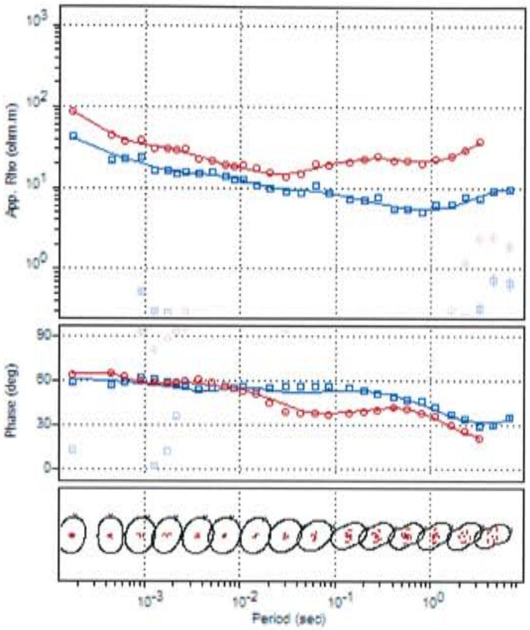

MT Line 3 Station 7

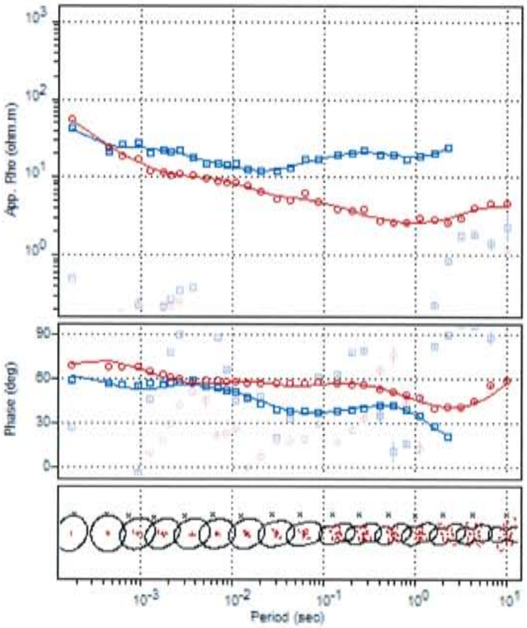

MT Line 3 Station 8

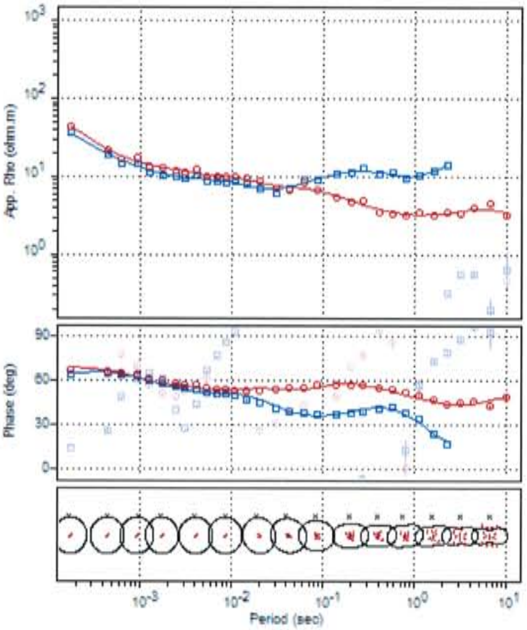

MT Line 3 Station 9

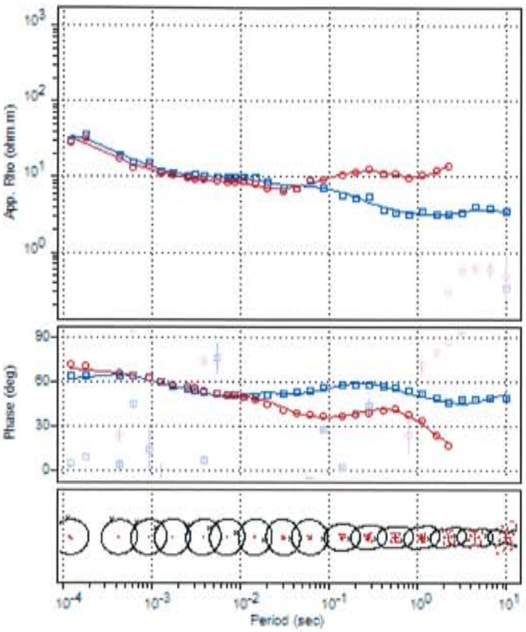

MT Line 3 Station 10

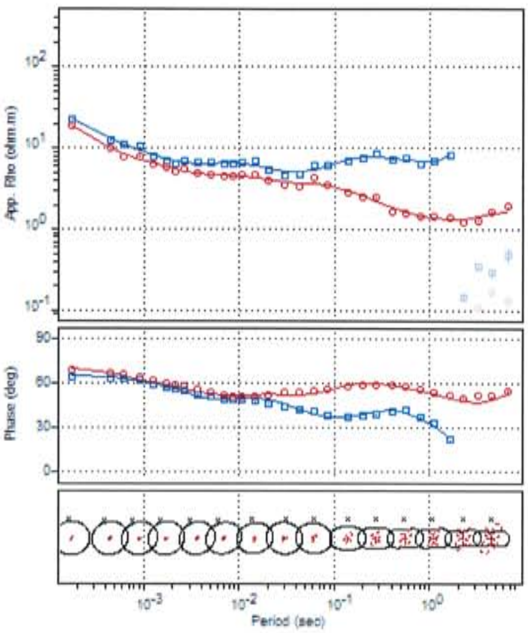

MT Line 3 Station 11

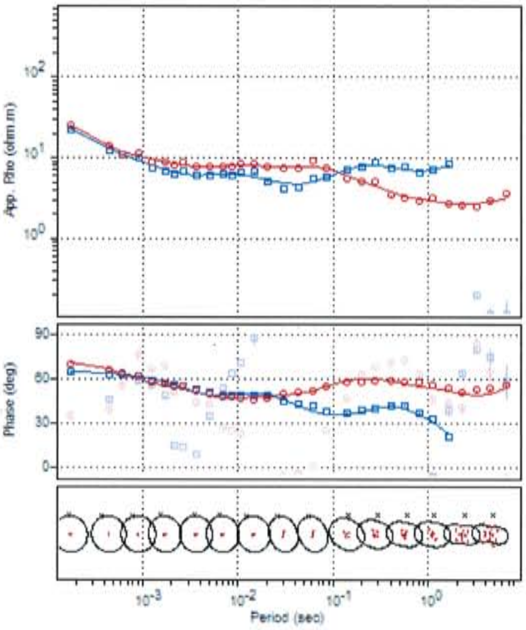

MT Line 3 Station 12

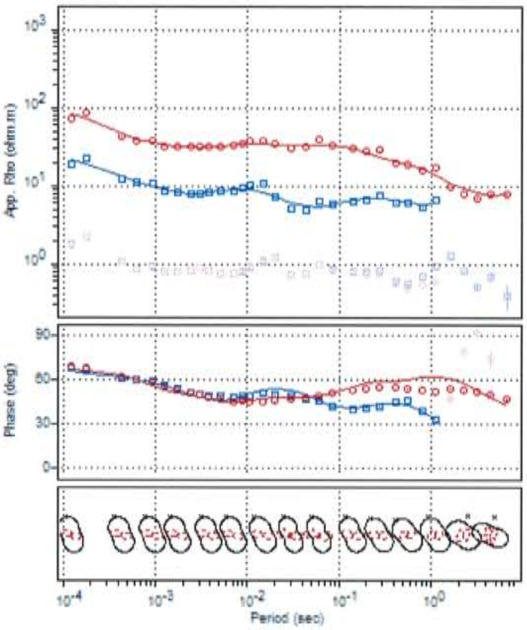

MT Line 3 Station 13

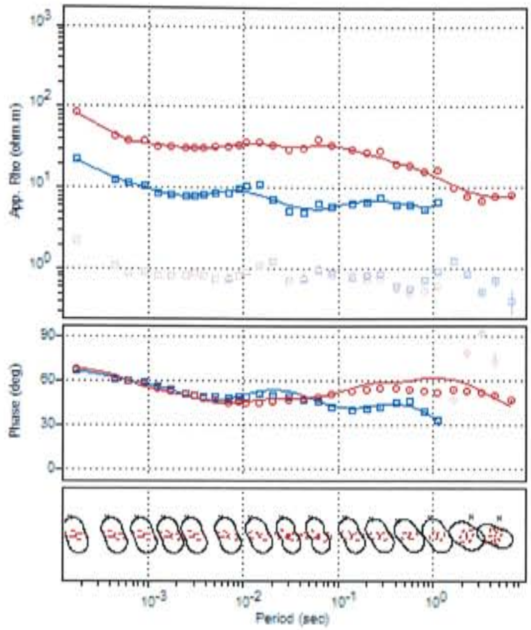

MT Line 3 Station 14

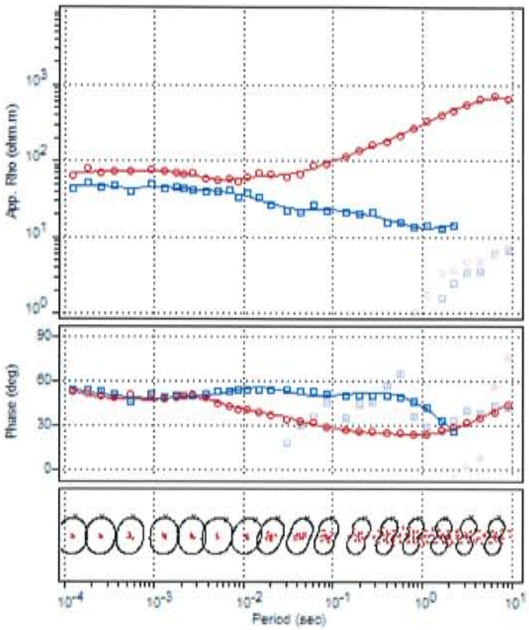

MT Line 4 Station 2

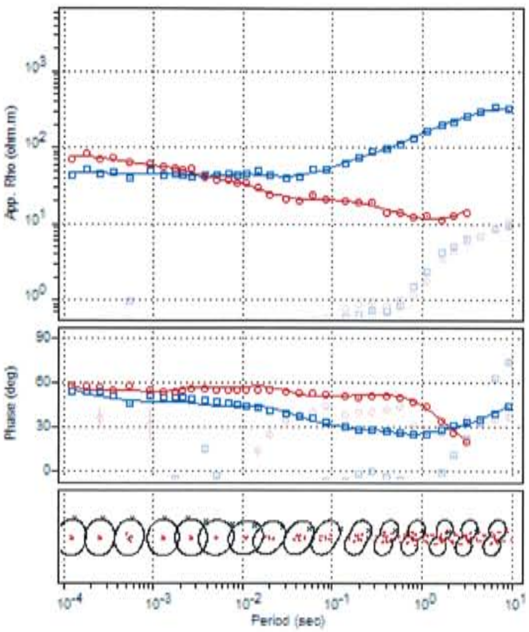

MT Line 4 Station 3

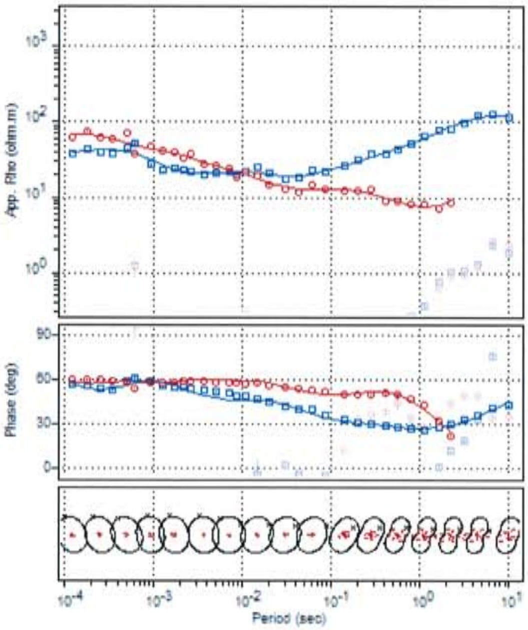

MT Line 4 Station 4

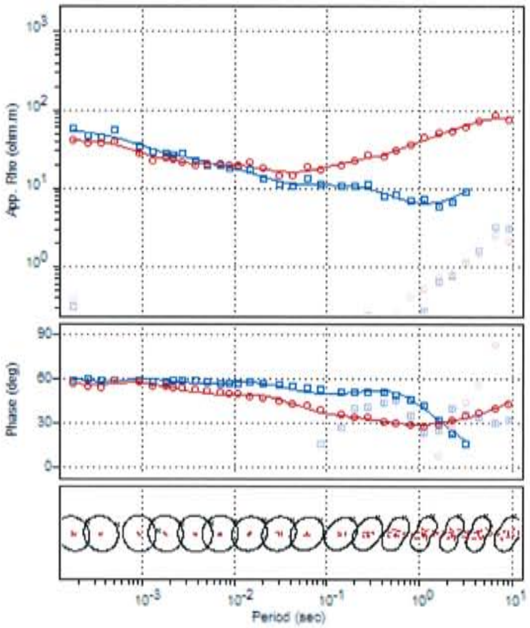

MT Line 4 Station 5

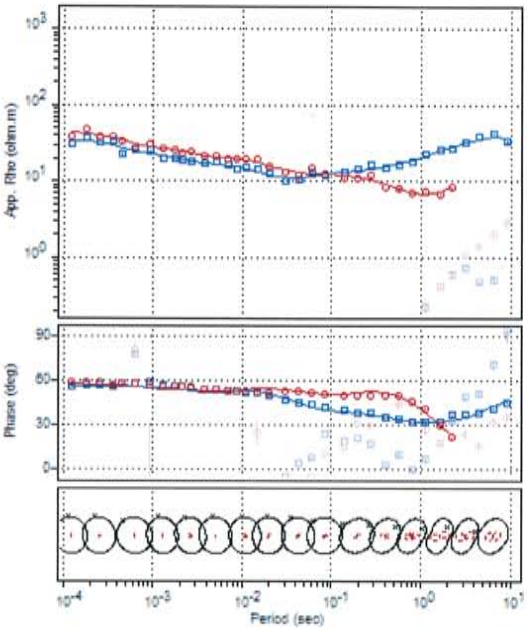

MT Line 4 Station 6

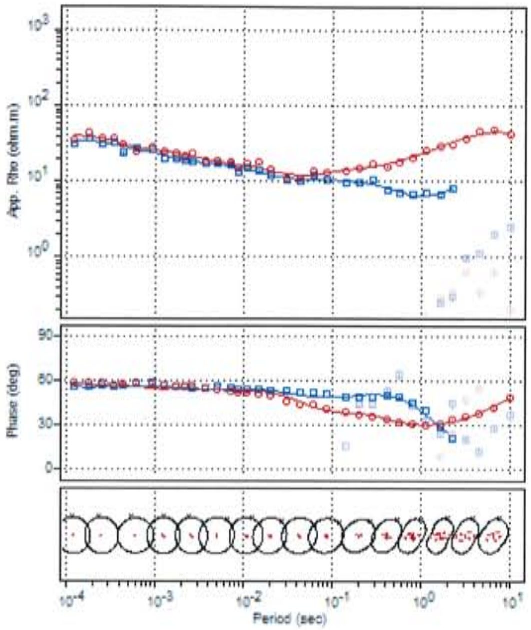

MT Line 4 Station 7

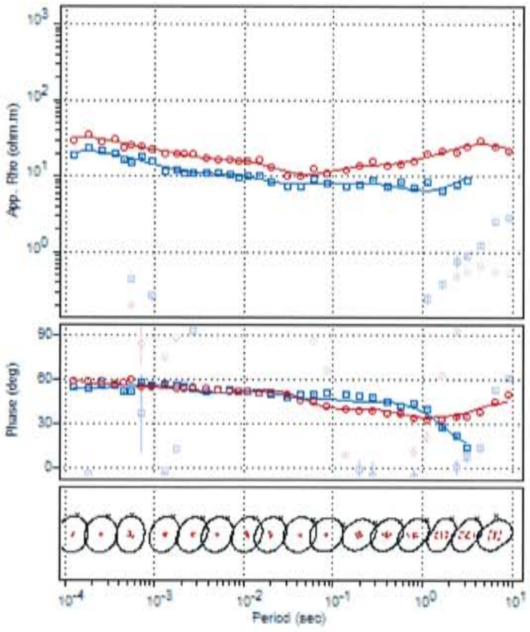

MT Line 4 Station 8

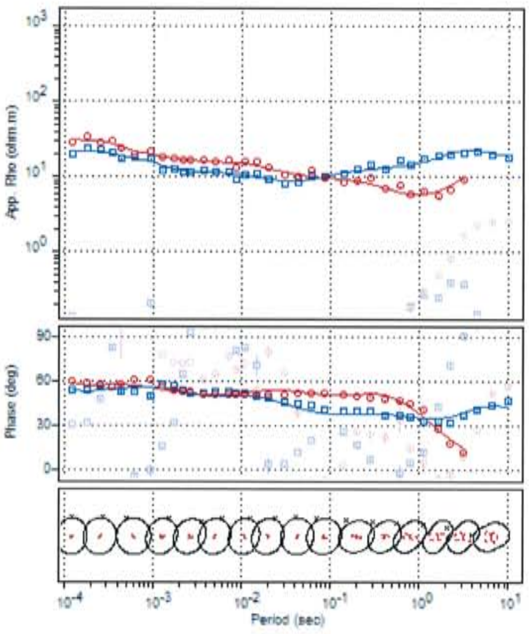

MT Line 4 Station 9

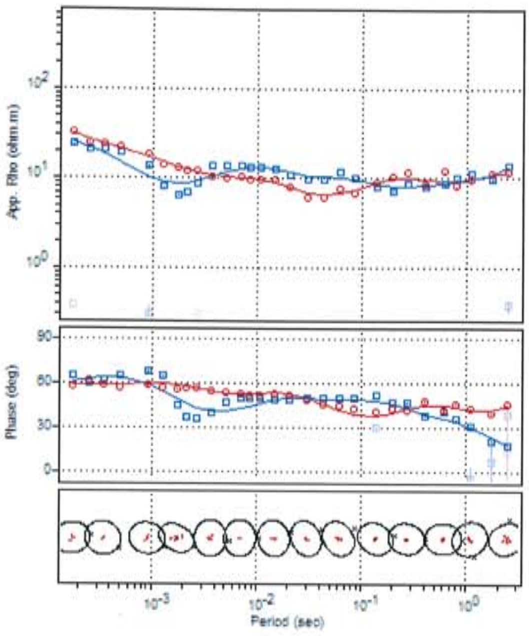

MT Line 4 Station 10

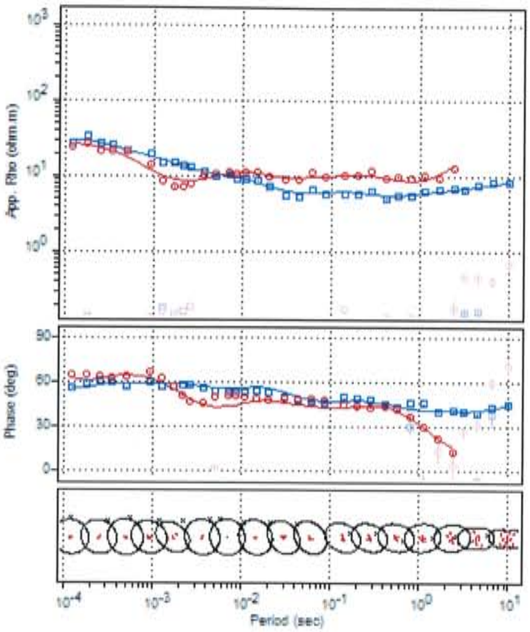

MT Line 4 Station 11

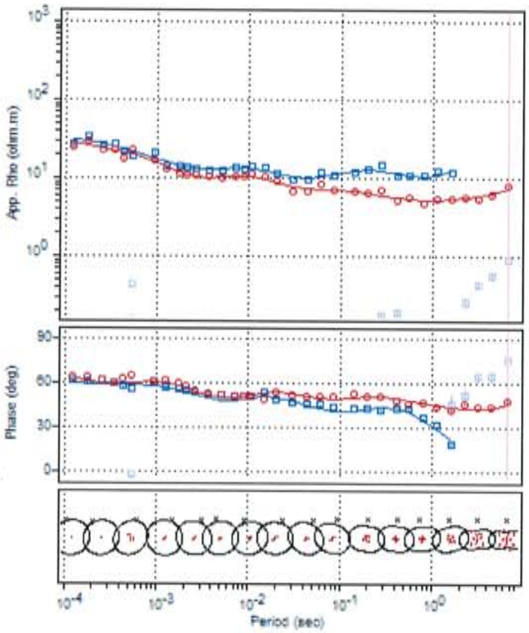

MT Line 4 Station 12

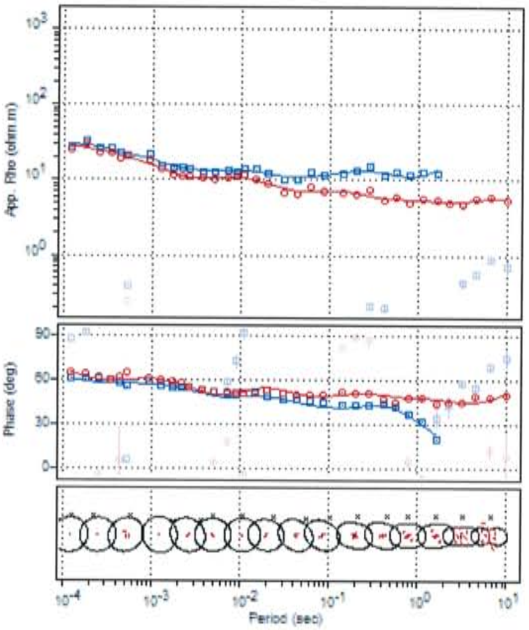

MT Line 4 Station 13

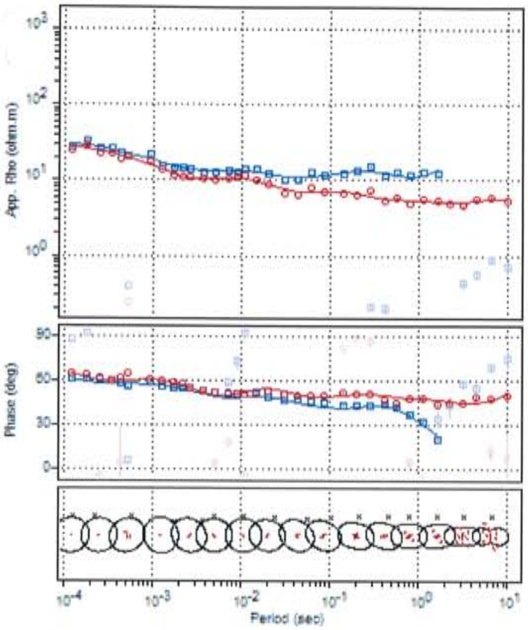

MT Line 4 Station 14

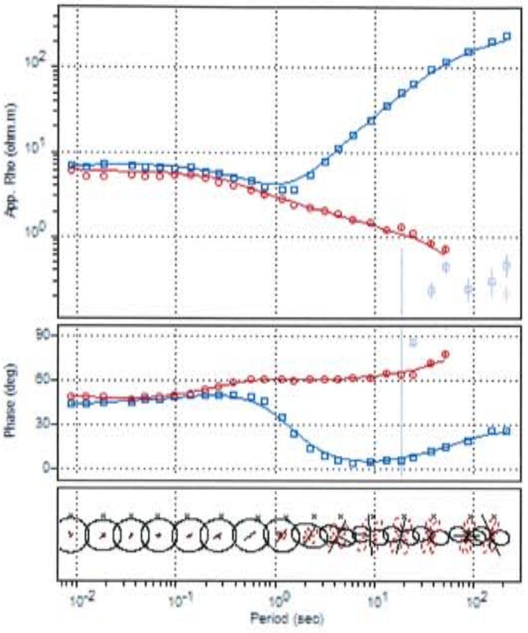

Stand-Alone Station NM-01

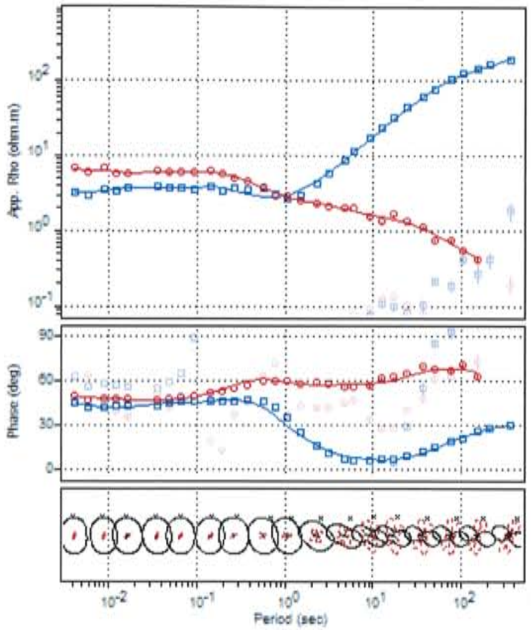

Stand-Alone Station NM-02

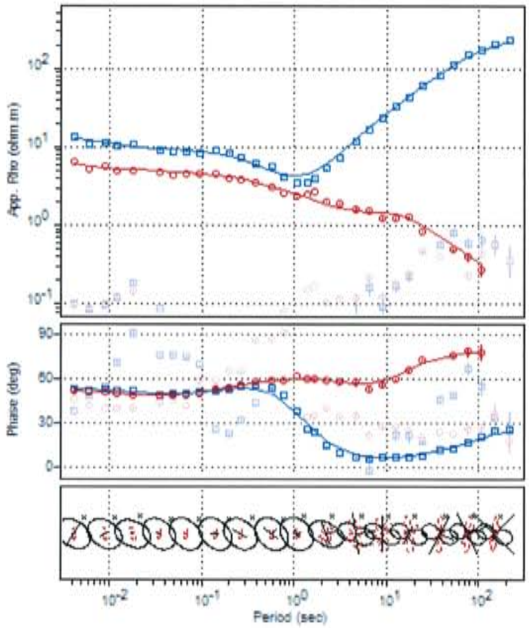

Stand-Alone Station NM-03

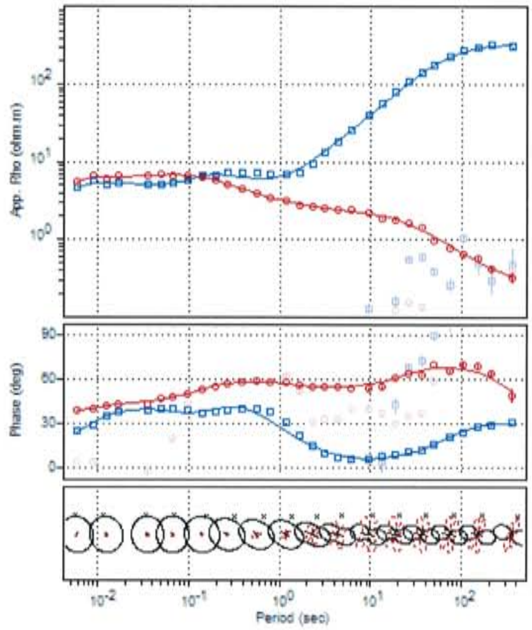

Stand-Alone Station NM-02

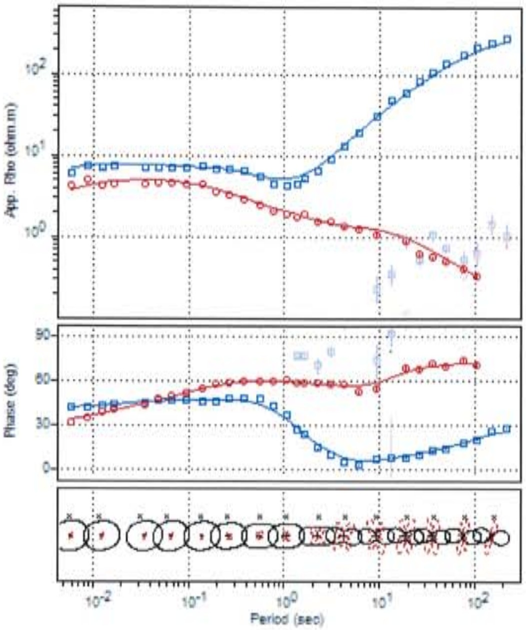

Stand-Alone Station NM-05

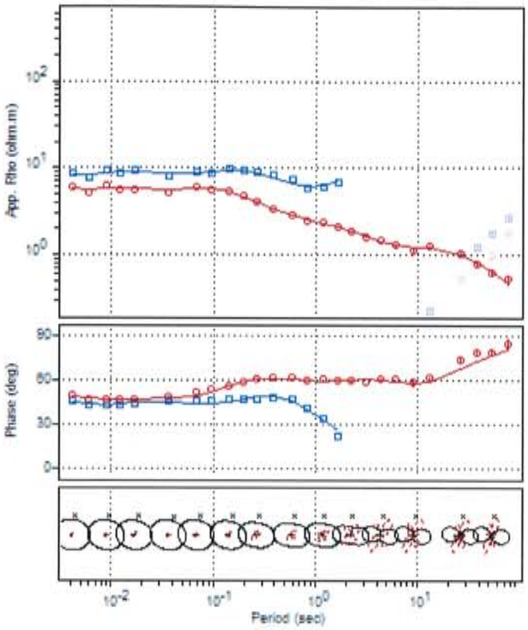

Stand-Alone Station NM-08

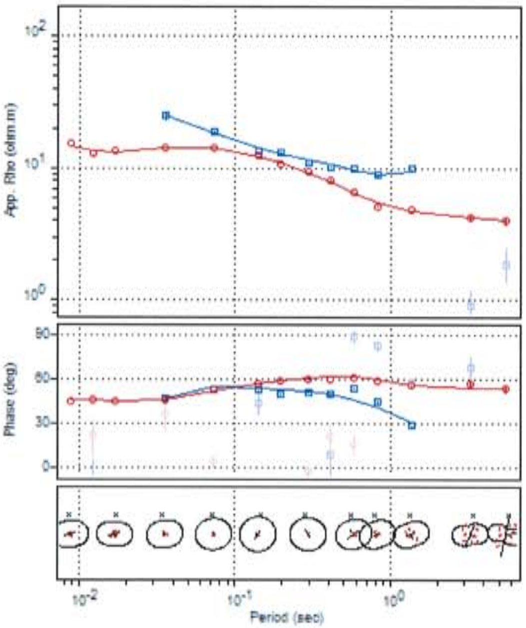

Stand-Alone Station NM-09

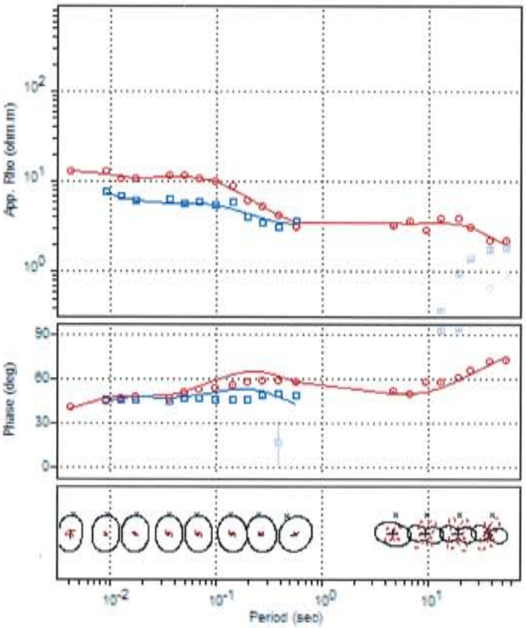

Stand-Alone Station NM-12

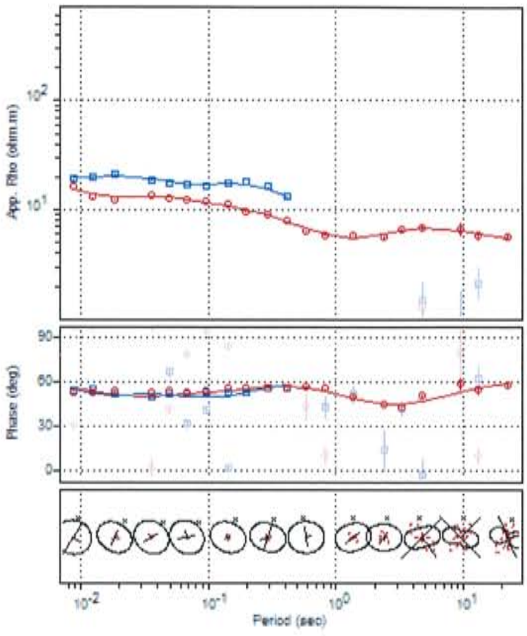

Stand-Alone Station NM-14

Appendix C. Gravity Values from A. Sanford's ongoing work up to date as of December 2006.

Station #	Observed	Lat N	Long W	Elevation	Terr	Theoretical	Anomaly
1.001	979118.22	34.0858	-107.0269	5769.8	1.0	979668.60	-203.3074
1.002	979166.71	34.0858	-107.0305	5786.0	0.9	979668.60	-203.9457
1.003	979113.30	34.0858	-107.0348	5810.2	0.9	979668.60	-205.9042
1.004	979109.98	34.0858	-107.0391	5835.4	0.9	979668.60	-207.7127
1.005	979107.44	34.0858	-107.0428	5854.6	0.9	979668.60	-209.1011
1.006	979105.05	34.0858	-107.0454	5872.2	0.9	979668.60	-210.4354
1.007	979101.84	34.0858	-107.0496	5894.5	0.9	979668.60	-212.3079
1.009	979097.56	34.0858	-107.0566	5928.6	0.9	979668.60	-214.5425
1.010	979095.29	34.0858	-107.061	5951.6	0.9	979668.60	-215.4330
1.011	979093.41	34.0858	-107.065	5971.0	0.9	979668.60	-216.1494
1.012	979092.22	34.0858	-107.0685	5986.9	0.9	979668.60	-216.3857
1.013	979091.08	34.0858	-107.0723	6003.2	0.9	979668.60	-216.5480
1.014	979090.18	34.0858	-107.0757	6020.3	0.9	979668.60	-216.4224
1.015	979089.85	34.0858	-107.0785	6030.6	0.9	979668.60	-216.1346
1.016	979088.62	34.0826	-107.0785	6055.9	0.9	979668.33	-215.5794
1.017	979089.17	34.086	-107.0785	6048.6	1.0	979668.62	-215.6517
1.018	979088.79	34.086	-107.0876	6064.6	1.0	979668.62	-215.0720
1.019	979088.70	34.0859	-107.0928	6081.2	1.1	979668.61	-214.0580
1.020	979089.25	34.0894	-107.0962	6089.0	1.1	979668.61	-213.1101
1.021	979089.95	34.0859	-107.1026	6104.7	1.3	979668.61	-211.1984
1.022	979090.13	34.0859	-107.1074	6122.7	1.4	979668.61	-209.8388
1.023	979088.98	34.0859	-107.1109	6152.9	1.4	979668.61	-209.1774
1.024	979087.92	34.0858	-107.1142	6183.0	1.5	979668.60	-208.3236
1.025	979089.25	34.0894	-107.114	6149.5	1.5	979668.90	-209.3042
1.026	979090.64	34.093	-107.1139	6109.5	1.4	979669.20	-210.7146
1.027	979091.44	34.0961	-107.114	6072.3	1.4	979669.46	-212.4052
1.028	979091.78	34.1005	-107.114	6025.1	1.3	979669.83	-215.3644
1.029	979092.18	34.1005	-107.1102	6003.5	1.3	979669.83	-216.1401
1.030	979092.68	34.1005	-107.1067	5990.1	1.2	979669.83	-216.6637
1.031	979092.76	34.1005	-107.1025	5984.5	1.1	979669.83	-217.0196
1.032	979092.97	34.1005	-107.0961	5968.8	1.0	979669.83	-217.8513
1.033	979092.85	34.1037	-107.1151	5990.1	1.3	979670.10	-216.6615
1.034	979093.33	34.1005	-107.0916	5958.5	1.0	979699.83	-218.1091
1.035	979093.85	34.1005	-107.1033	5950.0	0.9	979669.83	-218.1989
1.036	979094.56	34.1005	-107.0814	5941.7	0.9	979699.83	-217.9868
1.037	979095.11	34.1005	-107.0782	5936.2	0.9	979669.83	-217.7667
1.038	979095.91	34.1005	-107.0752	5927.7	0.9	979669.83	-217.4765
1.039	979097.02	34.1005	-107.0707	5917.1	0.9	979669.83	-217.0023
1.040	979098.32	34.1005	-107.0676	5906.3	0.8	979669.83	-216.4501
1.041	979099.65	34.1005	-107.0641	5895.2	0.8	979669.83	-215.7859
1.042	979101.10	34.1005	-107.0609	5886.1	0.8	979669.83	-214.8817
1.043	979103.17	34.1005	-107.0569	5873.0	0.8	979669.83	-213.5974
1.044	979105.63	34.1005	-107.0529	5858.4	0.8	979669.83	-212.0131
1.045	979108.63	34.1005	-107.048	5841.4	0.9	979669.83	-209.9328
1.046	979111.37	34.1005	-107.0434	5823.7	0.9	979699.83	-208.2544
1.047	979113.16	34.0978	-107.0406	5811.9	0.9	979669.60	-206.9463
1.048	979115.39	34.0976	-107.0374	5792.1	0.9	979669.59	-205.8871

Station #	Observed	Lat N	Long W	Elevation	Terr	Theoretical	Anomaly
1.049	979118.37	34.0976	-107.0342	5764.3	0.9	979669.59	-204.5746
1.050	979121.37	34.0961	-107.0309	5747.5	0.9	979669.46	-202.4567
1.051	979121.70	34.094	-107.0268	5748.6	1.0	979669.29	-201.7850
1.052	979092.20	34.1004	-107.1183	6043.6	1.4	979669.82	-213.6865
1.053	979091.79	34.1004	-107.125	6087.4	1.6	979669.83	-211.3093
1.054	979090.12	34.1004	-107.1315	6135.9	1.9	979669.82	-209.7703
1.055	979092.19	34.1044	-107.1315	6086.7	1.8	979670.16	-211.0860
1.056	979093.24	34.1075	-107.1315	6058.0	1.7	979670.42	-212.1169
1.057	979094.36	34.111	-107.1315	6032.6	1.6	979670.71	-212.9133
1.058	979095.74	34.1145	-107.1315	6008.7	1.5	979671.00	-213.3598
1.059	979095.07	34.1148	-107.136	6032.5	1.6	979671.03	-212.5273
1.060	979093.88	34.1148	-107.1404	6062.9	1.8	979671.03	-211.6940
1.061	979092.64	34.1146	-107.1442	6094.8	2.0	979671.01	-210.8039
1.062	979090.77	34.1146	-107.1493	6152.0	2.2	979671.01	-209.0430
1.063	979093.16	34.1185	-107.1492	6102.5	2.0	979671.34	-210.1484
1.064	979095.91	34.1226	-107.1492	6051.1	1.8	979671.68	-211.0246
1.065	979095.61	34.1228	-107.1468	6045.8	1.7	979671.70	-211.7592
1.066	979095.84	34.1149	-107.1256	5980.7	1.4	979671.04	-215.0727
1.067	979096.69	34.1149	-107.1195	5942.8	1.3	979671.04	-216.5959
1.068	979097.06	34.1149	-107.1138	5914.3	1.2	979671.04	-218.0354
1.069	979097.06	34.1149	-107.1087	5903.5	1.2	979671.04	-218.6831
1.070	979097.42	34.1149	-107.1046	5892.2	1.1	979671.04	-219.1009
1.071	979097.53	34.1149	-107.1008	5887.1	1.1	979671.04	-219.2968
1.072	979098.02	34.1149	-107.0958	5880.2	1.0	979671.04	-219.3207
1.073	979098.99	34.1149	-107.0914	5871.1	1.0	979671.04	-218.8965
1.074	979099.75	34.1149	-107.088	5865.5	1.0	979671.04	-218.4724
1.075	979101.10	34.1149	-107.0823	5857.1	1.0	979671.04	-217.6262
1.076	979102.17	34.1149	-107.078	5855.8	0.9	979671.04	-216.7342
1.077	979103.29	34.1149	-107.0738	5853.5	0.9	979671.04	-215.7521
1.078	979104.41	34.1149	-107.0696	5849.9	0.9	979671.04	-214.8481
1.079	979105.37	34.1149	-107.064	5854.1	0.9	979671.04	-213.6361
1.080	979106.11	34.1149	-107.0593	5861.8	0.9	979671.04	-212.4343
1.081	979107.49	34.1149	-107.0534	5871.0	0.9	979671.04	-210.5025
1.082	979108.13	34.1149	-107.0516	5870.6	0.9	979671.04	-209.8865
1.083	979108.56	34.1149	-107.0458	5886.2	0.9	979671.04	-208.5208
1.084	979108.76	34.1149	-107.043	5894.5	1.0	979671.04	-207.7230
1.085	979108.30	34.1168	-107.043	5905.8	1.0	979671.19	-207.6642
1.086	979104.34	34.1218	-107.0429	5980.7	1.0	979671.61	-207.5502
1.087	979106.62	34.126	-107.0427	5961.7	1.0	979671.96	-206.7614
1.088	979101.00	34.1293	-107.0428	6057.7	0.9	979672.24	-206.9996
1.089	979104.72	34.1293	-107.0476	5982.5	0.9	979672.40	-207.7901
1.090	979105.82	34.1293	-107.0516	5953.3	0.9	979672.24	-208.4415
1.091	979105.68	34.1293	-107.0561	5936.1	0.9	979672.24	-209.6131
1.092	979105.71	34.1293	-107.0602	5916.3	0.9	979672.24	-210.7708
1.093	979105.86	34.1293	-107.0653	5891.6	0.9	979672.24	-212.1023
1.094	979105.75	34.1293	-107.069	5880.7	0.9	979672.24	-212.8660
1.095	979106.17	34.1293	-107.074	5861.6	0.9	979672.24	-213.5917
1.096	979107.50	34.1293	-107.078	5831.4	0.9	979672.24	-214.0731
1.097	979107.28	34.1293	-107.083	5817.9	0.9	979672.24	-215.1028

Station #	Observed	Lat N	Long W	Elevation	Terr	Theoretical	Anomaly
1.098	979106.46	34.1293	-107.087	5817.7	0.9	979672.24	-215.9348
1.099	979105.04	34.1293	-107.092	5824.2	1.0	979672.24	-216.8649
1.100	979104.02	34.1293	-107.0959	5833.3	1.0	979672.24	-217.3391
1.101	979102.92	34.1293	-107.0998	5845.1	1.0	979672.24	-217.7313
1.102	979102.46	34.1293	-107.1043	5851.7	1.0	979672.24	-217.7955
1.103	979101.79	34.1293	-107.1095	5866.7	1.0	979672.24	-217.5658
1.104	979101.25	34.1292	-107.1138	5882.4	1.1	979672.23	-217.0557
1.105	979100.96	34.1292	-107.1177	5896.3	1.1	979672.23	-216.5120
1.106	979100.90	34.129	-107.1224	5912.7	1.1	979672.22	-215.5716
1.107	979100.83	34.129	-107.1262	5927.6	1.2	979672.22	-214.6479
1.108	979100.30	34.129	-107.1308	5949.4	1.2	979672.22	-213.8703
1.109	979099.63	34.129	-107.1356	5967.0	1.3	979672.22	-213.3847
1.110	979099.05	34.129	-107.1407	5981.1	1.3	979672.22	-213.1189
1.111	979098.21	34.129	-107.147	6009.0	1.4	979672.22	-212.1855
1.112	979097.64	34.1274	-107.1492	6021.0	1.6	979672.08	-211.7018
1.113	979096.77	34.1245	-107.1492	6034.5	1.7	979671.84	-211.4193
1.114	979098.26	34.1195	-107.1132	5906.0	1.2	979671.42	-217.7182
1.115	979100.26	34.1239	-107.1134	5887.7	1.1	979671.79	-217.2841
1.116	979102.36	34.133	-107.1136	5878.2	1.0	979672.55	-216.6157
1.117	979102.94	34.1373	-107.1135	5883.5	1.0	979672.91	-216.0778
1.118	979103.76	34.141	-107.1134	5882.5	1.0	979673.22	-215.6276
1.119	979104.10	34.1432	-107.1134	5880.2	1.0	979673.40	-215.6098
1.120	979103.74	34.1432	-107.1158	5882.5	1.0	979673.40	-215.8318
1.121	979103.32	34.1432	-107.1207	5890.5	1.0	979673.40	-215.7720
1.122	979102.87	34.1432	-107.1245	5907.0	1.0	979673.40	-215.2323
1.123	979102.46	34.1432	-107.1286	5922.4	1.0	979673.40	-214.7186
1.124	979101.68	34.1432	-107.1334	5935.3	1.0	979673.40	-214.7249
1.125	979100.26	34.1429	-107.1399	5954.9	1.0	979673.38	-214.9441
1.126	979099.45	34.1429	-107.1447	6002.5	1.0	979673.38	-212.8991
1.127	979098.40	34.1429	-107.1506	6030.0	1.1	979673.38	-212.1996
1.128	979097.33	34.1429	-107.1561	6057.5	1.2	979673.38	-211.5202
1.129	979096.92	34.1429	-107.1596	6074.2	1.2	979673.38	-210.9285
1.130	979096.22	34.1429	-107.1643	6098.1	1.3	979673.38	-210.0950
1.131	979095.52	34.1429	-107.1688	6122.7	1.4	979673.38	-209.2195
1.132	979095.10	34.1429	-107.173	6144.7	1.5	979673.38	-208.2199
1.133	979094.59	34.1429	-107.1782	6175.4	1.6	979673.38	-206.7886
1.134	979094.73	34.1429	-107.1842	6216.9	1.6	979673.38	-204.1594
1.135	979104.86	34.1432	-107.109	5867.8	1.0	979673.40	-215.6435
1.136	979105.41	34.1432	-107.104	5857.1	0.9	979673.40	-215.7853
1.137	979105.82	34.1432	-107.0987	5852.5	0.9	979673.40	-215.6512
1.138	979106.77	34.1432	-107.0923	5847.9	0.9	979673.40	-214.9771
1.139	979107.89	34.1433	-107.0862	5848.4	0.9	979673.41	-213.8355
1.140	979108.07	34.1433	-107.0804	5862.8	0.9	979673.41	-212.7918
1.141	979107.79	34.1433	-107.0756	5882.6	0.9	979673.41	-211.8842
1.142	979107.23	34.1433	-107.0687	5912.1	0.9	979673.41	-210.6748
1.143	979106.67	34.1433	-107.0644	5938.0	0.9	979673.41	-209.6813
1.144	979106.12	34.1433	-107.0602	5960.9	0.9	979673.41	-208.8578
1.145	979105.40	34.1433	-107.0559	5988.3	0.9	979673.41	-207.9343
1.146	979105.11	34.1433	-107.0516	6018.3	0.9	979673.41	-206.4249
1.147	979102.87	34.1433	-107.046	6074.6	0.9	979673.41	-205.2880

Station #	Observed	Lat N	Long W	Elevation	Terr	Theoretical	Anomaly
1.148	979104.72	34.1433	-107.0425	6058.4	1.0	979673.41	-204.3597
1.149	979104.92	34.1418	-107.0421	6047.6	1.0	979673.29	-204.6819
1.150	979103.36	34.138	-107.0417	6061.5	1.0	979672.97	-205.0900
1.151	979102.91	34.1331	-107.0429	6045.0	1.0	979672.56	-206.1194
1.152	979099.53	34.1311	-107.0428	6082.5	1.0	979672.39	-207.0828
1.156	979104.72	34.0813	-107.0434	5873.4	0.9	979668.22	-210.3170
1.157	979102.88	34.0764	-107.0434	5889.3	0.9	979667.81	-210.7934
1.158	979100.92	34.0714	-107.0437	5903.2	0.9	979667.40	-211.5014
1.159	979097.84	34.0714	-107.0485	5932.7	0.9	979667.40	-212.8120
1.160	979095.51	34.0714	-107.0522	5958.0	0.9	979667.40	-213.6245
1.161	979093.42	34.0714	-107.0568	5984.4	0.9	979667.40	-214.1210
1.162	979091.35	34.0714	-107.061	6010.0	0.9	979667.40	-214.6656
1.163	979089.27	34.0714	-107.0658	6042.2	0.9	979667.40	-214.8142
1.164	979087.84	34.0712	-107.07	6069.9	0.9	979667.38	-214.5660
1.165	979086.21	34.0712	-107.0742	6101.1	1.0	979667.38	-214.2746
1.166	979085.14	34.0712	-107.0785	6127.4	1.0	979667.38	-213.7172
1.167	979086.05	34.0745	-107.0788	6108.6	1.0	979667.65	-214.2108
1.168	979086.55	34.0783	-107.0839	6109.7	1.0	979667.97	-213.9627
1.169	979085.10	34.0755	-107.0871	6145.3	1.0	979667.74	-213.0432
1.170	979083.26	34.0715	-107.0913	6190.9	1.1	979667.40	-211.7135
1.171	979080.51	34.0677	-107.095	6243.6	1.3	979667.09	-210.7847
1.172	979077.64	34.0633	-107.0984	6295.7	1.5	979666.72	-209.9618
1.173	979075.14	34.0594	-107.1019	6344.4	1.6	979666.39	-209.1146
1.174	979073.17	34.0567	-107.1055	6386.5	1.8	979666.17	-208.1336
1.175	979072.61	34.0556	-107.1057	6396.8	1.8	979666.07	-207.9838
1.176	979070.43	34.0521	-107.1089	6447.8	2.1	979665.78	-206.5622
1.177	979067.17	34.0479	-107.1126	6512.7	2.4	979665.43	-205.2283
1.178	979065.33	34.0447	-107.1152	6549.7	2.6	979665.16	-204.3814
1.179	979063.97	34.0412	-107.1179	6583.3	2.9	979664.87	-203.1335
1.180	979074.29	34.0567	-107.0998	6351.6	1.6	979666.17	-209.3069
1.181	979075.85	34.0579	-107.0942	6311.8	1.5	979666.19	-210.2592
1.182	979075.87	34.057	-107.0887	6273.9	1.4	979666.19	-212.6125
1.183	979078.94	34.057	-107.0852	6246.4	1.3	979666.19	-211.2919
1.184	979080.82	34.057	-107.0804	6212.3	1.2	979666.19	-211.5572
1.185	979082.80	34.057	-107.0759	6177.2	1.2	979666.19	-211.6825
1.186	979084.99	34.057	-107.0717	6141.0	1.1	979666.19	-211.7638
1.187	979087.71	34.057	-107.0642	6087.5	1.1	979666.19	-212.2527
1.188	979089.22	34.0571	-107.0613	6062.8	1.1	979666.20	-212.2826
1.189	979089.81	34.0539	-107.0582	6053.8	1.1	979665.93	-211.9148
1.191	979089.71	34.0472	-107.0534	6056.1	1.1	979665.37	-211.3166
1.192	979088.71	34.0436	-107.0514	6069.5	1.1	979665.07	-211.2118
1.193	979087.76	34.0354	-107.0467	6090.4	1.1	979664.38	-210.2227
1.194	979088.15	34.0312	-107.0442	6087.6	1.3	979664.03	-209.4495
1.195	979089.00	34.0271	-107.0428	6081.3	1.3	979663.69	-208.6346
1.196	979090.70	34.0235	-107.0416	6059.1	1.3	979663.39	-207.9653
1.197	979089.05	34.0203	-107.0391	6089.7	1.3	979663.12	-207.5124
1.198	979091.32	34.0574	-107.0564	6025.8	1.0	979666.22	-212.4769
1.200	979097.68	34.0571	-107.0444	5938.9	0.9	979666.20	-211.4041
1.201	979099.36	34.0571	-107.0396	5914.4	0.9	979666.20	-211.1936
1.202	979100.91	34.0572	-107.0361	5900.6	0.9	979666.21	-210.4797

Station #	Observed	Lat N	Long W	Elevation	Terr	Theoretical	Anomaly
1.203	979102.02	34.0597	-107.0364	5882.5	0.9	979666.42	-210.6644
1.204	979104.45	34.0622	-107.0333	5864.3	1.0	979666.63	-209.4351
1.205	979106.97	34.0626	-107.0289	5845.4	1.1	979666.66	-207.9822
1.206	979111.33	34.0604	-107.0234	5791.2	1.1	979666.48	-206.6891
1.207	979112.35	34.056	-107.0186	5771.3	1.1	979666.11	-206.4948
1.208	979113.77	34.0528	-107.0138	5747.4	1.1	979665.84	-206.2407
1.209	979112.12	34.0502	-107.0126	5762.5	1.1	979665.62	-206.7676
1.210	979116.02	34.0475	-107.0098	5699.4	1.1	979665.40	-206.4265
1.211	979116.73	34.0436	-107.0076	5681.4	1.2	979665.07	-206.3701
1.212	979118.28	34.0382	-107.0065	5651.8	1.1	979664.62	-206.2440
1.213	979120.50	34.0349	-107.0031	5623.1	1.1	979664.34	-205.4695
1.214	979121.82	34.0316	-107.0012	5606.9	1.1	979664.07	-204.8953
1.215	979124.45	34.0279	-106.9997	5574.0	1.0	979663.76	-203.9794
1.216	979124.91	34.0247	-107.0014	5572.8	1.0	979663.49	-203.3238
1.217	979125.57	34.0206	-107.003	5575.4	1.0	979663.15	-202.1652
1.218	979124.50	34.0181	-107.0043	5589.9	1.1	979662.94	-202.0745
1.219	979122.42	34.0205	-107.0081	5610.0	1.1	979663.14	-203.1315
1.220	979119.50	34.0205	-107.0117	5645.0	1.1	979663.14	-203.9022
1.221	979113.52	34.0186	-107.0175	5723.1	1.2	979662.98	-205.0390
1.222	979103.56	34.0174	-107.0243	5850.9	1.2	979662.88	-207.1832
1.223	979095.37	34.0176	-107.0311	5976.0	1.3	979662.90	-207.8364
1.224	979088.52	34.017	-107.038	6096.6	1.3	979662.85	-207.3527
1.225	979084.44	34.0162	-107.0433	6167.1	1.4	979662.78	-207.0373
1.226	979079.48	34.0146	-107.0495	6250.2	1.6	979662.65	-206.6792
1.227	979076.67	34.0137	-107.0527	6296.7	1.7	979662.57	-206.5249
1.228	979073.11	34.0137	-107.0587	6365.6	1.8	979662.57	-205.8523
1.229	979069.30	34.0137	-107.0635	6408.2	1.9	979662.57	-207.0071
1.230	979065.92	34.0137	-107.0702	6458.4	2.2	979662.57	-207.0761
1.231	979065.07	34.0169	-107.07	6464.4	2.1	979662.84	-207.9337
1.232	979065.90	34.0206	-107.0698	6435.3	1.9	979663.15	-209.3584
1.233	979069.32	34.0266	-107.0698	6386.6	1.8	979663.65	-209.4609
1.234	979072.39	34.0295	-107.0686	6337.2	1.7	979663.89	-209.6964
1.235	979064.53	34.0228	-107.0734	6463.9	2.0	979663.33	-209.0968
1.236	979058.12	34.0184	-107.0787	6571.1	2.5	979662.96	-208.2092
1.237	979053.80	34.0154	-107.0829	6652.4	3.1	979662.71	-206.8021
1.240	979075.35	34.0322	-107.0668	6288.2	1.5	979664.12	-210.1011
1.241	979079.43	34.0348	-107.062	6223.4	1.4	979664.33	-210.2252
1.242	979083.16	34.0356	-107.0565	6172.2	1.3	979664.40	-209.7330
1.243	979085.30	34.0357	-107.052	6136.3	1.3	979664.41	-209.8047
1.244	979090.35	34.0352	-107.0418	6047.4	1.1	979664.37	-210.1951
1.245	979092.98	34.0357	-107.0379	6006.5	1.1	979664.41	-210.0601
1.246	979095.57	34.0372	-107.0332	5965.7	1.1	979664.54	-210.0427
1.247	979097.32	34.0396	-107.0298	5938.8	1.0	979664.74	-210.2068
1.248	979098.61	34.0427	-107.029	5925.4	1.0	979665.00	-209.9797
1.249	979097.53	34.046	-107.0327	5941.6	1.0	979665.27	-210.3640
1.250	979098.01	34.0498	-107.0352	5930.9	1.0	979665.59	-210.8435
1.251	979099.35	34.0537	-107.0362	5914.0	1.0	979665.92	-210.8433
1.252	979143.59	34.005	-106.9754	5347.2	1.1	979661.84	-196.4788
1.253	979146.32	34.0058	-106.9714	5296.1	1.1	979661.91	-196.8807
1.254	979147.11	34.0043	-106.966	5271.6	1.0	979661.79	-197.5348

Station #	Observed	Lat N	Long W	Elevation	Terr	Theoretical	Anomaly
1.255	979147.56	34.004	-106.9597	5250.7	0.9	979661.76	-198.3633
1.256	979152.39	34.005	-106.9498	5163.4	1.0	979661.84	-198.7532
1.257	979154.37	34.0073	-106.945	5122.9	1.1	979662.04	-199.3446
1.258	979155.84	34.0102	-106.94	5084.5	1.1	979662.28	-200.3701
1.259	979156.13	34.0124	-106.9365	5055.7	1.1	979662.46	-201.9914
1.260	979158.31	34.015	-106.932	5020.5	1.1	979662.68	-202.1400
1.261	979163.57	34.0187	-106.9254	4958.2	1.2	979662.99	-200.8760
1.262	979165.67	34.022	-106.9205	4916.4	1.2	979663.26	-201.5790
1.263	979167.91	34.0302	-106.9173	4862.1	1.2	979663.95	-203.2114
1.264	979169.25	34.0341	-106.9148	4824.2	1.2	979664.28	-204.2308
1.265	979171.68	34.0427	-106.9086	4779.8	1.2	979665.00	-205.4228
1.266	979173.85	34.0461	-106.9059	4738.5	1.2	979665.28	-206.0143
1.267	979181.96	34.0526	-106.899	4653.9	1.3	979665.82	-203.4420
1.268	979184.16	34.0564	-106.8978	4634.0	1.3	979666.14	-202.7335
1.269	979185.30	34.0597	-106.8983	4623.1	1.3	979666.42	-202.5232
1.270	979185.96	34.063	-106.903	4616.0	1.3	979666.69	-202.5651
1.271	979183.47	34.0627	-106.9074	4643.6	1.4	979666.67	-203.2746
1.272	979178.55	34.0594	-106.9114	4708.1	1.3	979666.39	-204.1499
1.273	979175.64	34.0592	-106.9167	4752.0	1.4	979666.37	-204.3100
1.274	979173.38	34.0549	-106.9264	4818.1	1.5	979666.02	-202.1457
1.275	979173.52	34.0539	-106.9312	4851.1	1.6	979665.93	-199.8428
1.276	979174.42	34.0539	-106.9363	4889.8	2.1	979665.93	-196.1215
1.277	979174.61	34.0536	-106.941	4930.7	2.5	979665.91	-193.0533
1.278	979171.91	34.0512	-106.9442	4974.5	2.5	979665.71	-192.9254
1.279	979165.91	34.0504	-106.9472	5059.9	2.5	979665.64	-193.7363
1.280	979160.45	34.0487	-106.9492	5137.1	2.5	979665.50	-194.4236
1.281	979156.52	34.0468	-106.9519	5183.4	2.4	979665.34	-195.5177
1.282	979187.18	34.0689	-106.9031	4613.4	1.3	979667.19	-201.9945
1.283	979187.11	34.0726	-106.9061	4618.9	1.3	979667.50	-202.0441
1.284	979187.71	34.0758	-106.9084	4615.2	1.4	979667.76	-201.8337
1.285	979187.87	34.0784	-106.9092	4618.9	1.4	979667.98	-201.6693
1.286	979187.39	34.0822	-106.91	4637.2	1.3	979668.30	-201.4695
1.287	979186.08	34.0861	-106.9107	4664.1	1.3	979668.63	-201.4924
1.288	979182.58	34.0902	-106.9116	4679.8	1.3	979668.97	-204.3937
1.289	979185.03	34.0935	-106.9124	4693.5	1.3	979669.24	-201.3981
1.290	979184.40	34.0974	-106.9132	4707.1	1.3	979669.57	-201.5387
1.291	979184.53	34.099	-106.9163	4705.2	1.3	979669.70	-201.6565
1.292	979183.59	34.1106	-106.9193	4721.4	1.3	979670.68	-202.5956
1.293	979183.08	34.1023	-106.9213	4732.6	1.4	979669.98	-201.6892
1.294	979182.49	34.1035	-106.9228	4742.9	1.3	979670.08	-201.8119
1.295	979182.21	34.1039	-106.9242	4748.5	1.3	979670.11	-201.7894
1.296	979180.51	34.1057	-106.9267	4767.0	1.3	979670.27	-202.5304
1.298	979176.10	34.1107	-106.9297	4853.4	1.3	979670.68	-202.1766
1.299	979176.11	34.1107	-106.9335	4870.0	1.3	979670.68	-201.1709
1.300	979176.30	34.1116	-106.9385	4896.9	1.3	979670.76	-199.4428
1.301	979176.22	34.1149	-106.9406	4906.8	1.3	979671.04	-199.2052
1.302	979176.81	34.1114	-106.9438	4920.0	1.3	979670.74	-197.5305
1.303	979177.01	34.1104	-106.949	4949.0	1.4	979670.66	-195.4074
1.304	979175.49	34.11	-106.9542	4997.4	1.3	979670.62	-194.0909
1.305	979176.14	34.1116	-106.9568	4999.2	1.3	979670.76	-193.4669

Station #	Observed	Lat N	Long W	Elevation	Terr	Theoretical	Anomaly
1.306	979174.35	34.1149	-106.9578	5030.7	1.3	979671.04	-193.6437
1.307	979176.61	34.114	-106.953	4981.6	1.4	979670.96	-194.1534
1.308	979177.40	34.1163	-106.9491	4946.0	1.3	979671.15	-195.7912
1.310	979179.77	34.1199	-106.9441	4868.5	1.2	979671.45	-198.4709
1.311	979178.53	34.1215	-106.9403	4851.0	1.3	979671.59	-200.7945
1.312	979178.15	34.1232	-106.9369	4827.8	1.3	979671.73	-202.7083
1.313	979177.70	34.1252	-106.9328	4808.4	1.3	979671.90	-204.4894
1.314	979178.78	34.1257	-106.9276	4778.1	1.3	979671.94	-205.2686
1.315	979180.38	34.1278	-106.9221	4752.3	1.4	979672.11	-205.2919
1.316	979182.33	34.1298	-106.9177	4729.1	1.3	979672.28	-205.0009
1.317	979184.63	34.1323	-106.9131	4706.7	1.4	979672.49	-204.1537
1.318	979187.02	34.1337	-106.9094	4684.1	1.4	979672.61	-203.1945
1.319	979190.48	34.132	-106.9034	4664.5	1.4	979672.47	-200.8598
1.320	979193.62	34.1281	-106.9006	4632.7	1.4	979672.14	-199.3006
1.321	979195.44	34.1257	-106.8966	4637.6	1.4	979671.94	-196.9858
1.322	979196.18	34.1207	-106.8937	4629.2	1.4	979671.52	-196.3311
1.323	979196.80	34.1221	-106.8929	4621.7	1.4	979671.64	-196.2782
1.324	979178.78	34.1067	-106.9229	4798.3	1.3	979670.35	-202.4667
1.325	979176.30	34.1107	-106.9238	4834.6	1.3	979670.68	-203.1042
1.326	979174.21	34.1152	-106.9259	4859.0	1.3	979671.06	-204.1074
1.327	979171.13	34.119	-106.9275	4897.8	1.3	979671.38	-205.1782
1.328	979172.13	34.123	-106.9291	4879.7	1.3	979671.71	-205.5986
1.329	979174.30	34.1281	-106.9307	4850.6	1.3	979672.14	-205.6010
1.330	979171.12	34.1326	-106.9325	4900.8	1.3	979672.52	-206.1467
1.331	979171.61	34.1366	-106.9334	4898.3	1.3	979672.85	-206.1415
1.332	979170.93	34.14	-106.9352	4921.1	1.3	979673.14	-205.7387
1.333	979172.08	34.1451	-106.9363	4922.5	1.3	979673.56	-204.9317
1.334	979172.87	34.1488	-106.9374	4927.0	1.3	979673.87	-204.1816
1.335	979174.95	34.1535	-106.9365	4901.6	1.3	979674.27	-204.0187
1.336	979177.75	34.1573	-106.936	4863.8	1.3	979674.58	-203.8042
1.337	979179.83	34.1623	-106.9353	4841.0	1.4	979675.00	-203.4105
1.338	979182.62	34.1676	-106.9341	4803.0	1.5	979675.41	-203.2017
1.339	979180.06	34.1676	-106.9388	4870.3	1.4	979675.45	-201.8669
1.340	979178.74	34.1676	-106.9434	4942.0	1.5	979675.45	-198.7864
1.341	979177.54	34.1676	-106.9486	5036.2	1.5	979675.45	-194.3363
1.342	979183.70	34.1705	-106.9335	4789.0	1.5	979675.69	-203.2462
1.343	979185.15	34.1746	-106.9329	4772.8	1.5	979676.03	-203.1113
1.345	979182.95	34.1779	-106.9382	4850.3	1.5	979676.31	-200.9393
1.346	979180.82	34.1778	-106.9428	4924.3	1.5	979676.30	-198.6224
1.347	979180.13	34.1779	-106.9468	4997.2	1.6	979676.31	-194.8483
1.348	979178.63	34.1788	-106.9514	5089.7	1.6	979676.39	-190.8755
1.349	979174.89	34.1796	-106.9561	5206.2	1.6	979676.45	-187.6949
1.350	979170.29	34.1804	-106.9614	5326.7	1.8	979676.52	-184.9343
1.351	979165.79	34.1812	-106.9656	5436.9	1.9	979676.59	-182.7915
1.352	979161.05	34.1815	-106.9697	5542.1	2.0	979676.61	-181.1467
1.353	979155.09	34.1797	-106.9729	5639.7	2.3	979676.46	-180.8019
1.354	979149.28	34.1784	-106.9754	5729.2	2.2	979676.35	-181.2348
1.355	979145.65	34.1778	-106.9775	5786.9	2.2	979676.30	-181.3537
1.356	979140.30	34.1784	-106.9806	5862.2	2.2	979676.35	-182.2375
1.357	979178.52	34.1752	-106.9508	5070.3	1.5	979676.08	-191.9476

Station #	Observed	Lat N	Long W	Elevation	Terr	Theoretical	Anomaly
1.358	979177.05	34.1697	-106.9519	5080.4	1.5	979675.62	-192.3510
1.359	979184.87	34.0531	-106.8931	4620.8	1.3	979665.86	-202.5893
1.360	979186.88	34.0539	-106.8883	4599.4	1.3	979665.93	-201.9297
1.362	979188.63	34.058	-106.8856	4588.9	1.3	979666.27	-201.1524
1.363	979188.63	34.0614	-106.8836	4595.0	1.3	979666.56	-201.0709
1.364	979190.00	34.0614	-106.8796	4592.4	1.3	979666.56	-199.8568
1.365	979191.01	34.0619	-106.8756	4590.3	1.2	979666.60	-199.1146
1.366	979191.44	34.0592	-106.8749	4588.7	1.2	979666.37	-198.5547
1.367	979189.25	34.0545	-106.8731	4587.3	1.1	979665.98	-200.4857
1.368	979174.23	34.0509	-106.9359	4880.1	2.0	979665.68	-196.7425
1.369	979174.37	34.0471	-106.9351	4866.5	1.8	979665.36	-197.3004
1.370	979172.22	34.0427	-106.9324	4883.2	1.5	979665.00	-198.3809
1.371	979171.87	34.0408	-106.9285	4855.5	1.4	979664.84	-200.3335
1.372	979171.52	34.0385	-106.9258	4840.2	1.4	979664.64	-201.4089
1.373	979170.75	34.0368	-106.9231	4835.8	1.3	979664.50	-202.4006
1.374	979169.94	34.0366	-106.9163	4819.4	1.2	979664.49	-204.2776
1.375	979168.83	34.0313	-106.9107	4821.5	1.2	979664.04	-204.8185
1.376	979169.07	34.0272	-106.9048	4809.2	1.2	979663.70	-204.9736
1.377	979172.89	34.0198	-106.8949	4749.0	1.3	979663.08	-204.0958
1.378	979174.79	34.0148	-106.8913	4714.9	1.3	979662.66	-203.8232
1.379	979177.42	34.011	-106.8874	4667.0	1.3	979662.35	-203.7487
1.380	979179.27	34.0082	-106.8845	4628.0	1.3	979662.11	-204.0039
1.381	979161.91	34.0181	-106.9215	4971.7	1.2	979662.94	-201.6262
1.382	979163.14	34.019	-106.916	4934.6	1.2	979663.01	-202.6966
1.383	979167.30	34.0203	-106.9088	4853.0	1.2	979663.12	-203.5397
1.384	979169.14	34.0214	-106.9025	4818.8	1.2	979663.24	-203.8680
1.385	979188.44	34.0501	-106.868	4588.3	1.1	979665.61	-200.8677
1.386	979187.47	34.0451	-106.866	4586.2	1.1	979665.20	-201.5456
1.387	979186.39	34.0396	-106.8666	4583.1	1.1	979664.74	-202.3517
1.388	979185.78	34.0371	-106.8672	4583.7	1.1	979664.53	-202.7167
1.389	979184.84	34.0324	-106.8663	4582.1	1.1	979664.13	-203.3597
1.390	979184.57	34.0294	-106.8649	4580.5	1.1	979663.88	-203.4749
1.391	979183.96	34.0242	-106.8624	4578.6	1.1	979663.45	-203.7642
1.392	979183.31	34.0187	-106.8622	4576.5	1.1	979662.99	-204.0804
1.393	979182.71	34.0135	-106.8663	4575.3	1.1	979662.55	-204.3178
1.394	979182.26	34.0094	-106.8695	4575.5	1.3	979662.21	-204.2631
1.395	979180.72	34.003	-106.8696	4583.9	1.3	979661.68	-204.7644
1.396	979181.18	33.9984	-106.8686	4571.2	1.3	979661.29	-204.6818
1.397	979181.18	33.9942	-106.8657	4569.5	1.2	979660.94	-204.4828
1.398	979181.62	33.989	-106.8602	4565.5	1.1	979660.51	-203.9483
1.399	979181.13	33.983	-106.8606	4564.1	1.1	979660.01	-204.0210
1.400	979180.35	33.9753	-106.8604	4564.0	1.1	979659.36	-204.1638
1.401	979179.84	33.9698	-106.8602	4561.8	1.1	979658.90	-204.3463
1.402	979179.27	33.9643	-106.8569	4558.2	1.1	979658.44	-204.6729
1.403	979178.16	33.9587	-106.8525	4559.1	1.1	979657.98	-205.2612
1.404	979177.71	33.9524	-106.8492	4554.2	1.1	979657.45	-205.4790
1.405	979176.71	33.9449	-106.851	4551.0	1.1	979656.82	-206.0447
1.406	979176.20	33.9406	-106.8512	4551.2	1.1	979656.46	-206.1837
1.407	979175.77	33.9348	-106.8513	4550.5	1.1	979655.98	-206.1714
1.408	979181.93	34.0055	-106.8774	4574.6	1.2	979661.89	-204.3712

Station #	Observed	Lat N	Long W	Elevation	Terr	Theoretical	Anomaly
1.410	979178.34	34.0038	-106.8865	4631.5	1.3	979661.74	-204.3062
1.411	979479.42	33.9994	-106.8874	4600.5	1.3	979661.38	-204.7679
1.412	979179.74	33.9959	-106.8868	4588.6	1.3	979661.08	-204.8692
1.413	979178.87	33.9876	-106.8852	4581.4	1.3	979660.39	-205.4776
1.414	979199.82	33.9824	-106.8863	4585.1	1.2	979659.96	-205.9713
1.415	979176.13	33.9764	-106.8807	4602.5	1.2	979659.45	-206.1164
1.416	979175.49	33.9717	-106.8775	4593.9	1.2	979659.06	-206.8796
1.417	979177.39	33.9678	-106.8732	4574.1	1.1	979658.74	-205.8915
1.418	979177.74	33.9629	-106.8737	4561.1	1.1	979658.33	-205.9120
1.419	979176.67	33.9588	-106.8722	4568.5	1.1	979657.98	-206.1957
1.420	979176.42	33.9538	-106.8704	4562.1	1.1	979657.57	-206.4121
1.421	979174.66	33.9472	-106.8696	4575.1	1.1	979657.02	-206.8412
1.422	979174.68	33.9428	-106.8705	4569.2	1.1	979656.65	-206.8077
1.423	979175.64	33.9381	-106.8721	4549.6	1.1	979656.26	-206.6309
1.424	979175.36	33.9345	-106.8714	4547.9	1.1	979655.96	-206.7123
1.425	979165.55	34.0176	-106.912	4877.1	1.1	979662.90	-203.7185
1.426	979165.34	34.0135	-106.9079	4859.3	1.1	979662.55	-204.6534
1.427	979166.58	34.0113	-106.9041	4826.5	1.1	979662.37	-205.1969
1.431	979174.48	34.1229	-106.9449	4949.2	1.2	979671.70	-199.1717
1.432	979173.87	34.1254	-106.9484	4982.7	1.2	979671.91	-197.9816
1.433	979171.47	34.1298	-106.9538	5057.4	1.2	979672.28	-196.2694
1.434	979170.82	34.1332	-106.9594	5106.6	1.2	979672.57	-194.2531
1.435	979169.71	34.1373	-106.9635	5172.1	1.3	979672.91	-191.6776
1.436	979167.60	34.1406	-106.967	5239.6	1.5	979673.19	-189.8153
1.437	979166.54	34.1439	-106.9712	5299.8	1.6	979673.46	-187.4408
1.438	979167.18	34.1444	-106.9795	5351.9	1.6	979673.50	-183.7177
1.439	979171.74	34.1455	-106.981	5345.0	2.0	979673.60	-179.2637
1.443	979170.74	34.1452	-106.9775	5304.3	1.6	979673.57	-193.0797
1.444	979169.80	34.145	-106.9732	5268.4	1.5	979673.55	-186.2563
1.445	979169.59	34.1452	-106.9675	5218.1	1.5	979673.57	-189.5000
1.446	979168.61	34.1463	-106.9635	5199.8	1.4	979673.66	-191.7697
1.447	979168.13	34.1466	-106.9593	5173.9	1.3	979673.69	-193.9283
1.448	979169.46	34.1474	-106.955	5125.0	1.4	979673.76	-195.4983
1.449	979170.75	34.1482	-106.9499	5066.6	1.3	979673.82	-197.8782
1.450	979171.93	34.1494	-106.9452	5005.6	1.3	979673.92	-200.4574
1.451	979172.61	34.1507	-106.9401	4949.6	1.3	979674.03	-203.2452
1.453	979199.10	34.123	-106.8892	4613.1	1.4	979671.71	-194.5693
1.454	979199.38	34.1254	-106.8887	4617.6	1.4	979671.91	-194.2203
1.455	979200.21	34.1288	-106.8873	4616.5	1.4	979672.20	-193.7409
1.456	979201.49	34.1329	-106.8846	4617.6	1.3	979672.54	-192.7882
1.457	979202.26	34.1375	-106.8815	4620.9	1.3	979672.93	-192.2553
1.458	979202.47	34.1441	-106.8804	4623.2	1.3	979673.48	-192.4600
1.459	979202.19	34.1485	-106.8819	4625.0	1.3	979673.85	-193.0005
1.460	979201.58	34.1526	-106.8841	4626.1	1.3	979674.19	-193.8878
1.461	979201.36	34.1565	-106.8853	4629.2	1.3	979674.52	-194.2485
1.462	979042.88	34.0943	-107.2292	6889.0	1.6	979669.31	-211.6289
1.463	979013.97	34.0855	-107.2167	7340.0	1.6	979668.57	-212.7517
1.464	979082.66	34.1419	-107.2432	6401.0	0.9	979673.30	-205.8033
1.465	979095.53	35.1565	-107.236	6244.0	0.9	979674.52	-203.5728
1.466	979106.04	34.1925	-107.2153	6199.0	0.9	979677.53	-198.7775

Station #	Observed	Lat N	Long W	Elevation	Terr	Theoretical	Anomaly
1.467	979115.84	34.2301	-107.2196	6059.0	0.7	979680.68	-200.7260
1.468	979121.43	34.2282	-107.177	5861.0	0.6	979680.53	-206.9527
1.470	979113.64	34.1977	-107.1003	5849.0	0.8	979677.97	-212.7062
1.471	979123.21	34.2153	-107.0612	5955.0	0.8	979679.44	-198.2533
1.478	979199.95	34.1587	-106.8882	4628.1	1.3	979674.70	-195.8587
1.479	979199.35	34.1562	-106.8897	4625.4	1.3	979674.49	196.4113
1.480	979196.61	34.1565	-106.8962	4621.1	1.3	979674.52	-199.4343
1.481	979194.06	34.1595	-106.9018	4626.9	1.3	979674.77	-201.8877
1.482	979193.08	34.1598	-106.9049	4628.1	1.3	979674.79	-202.8208
1.483	979191.33	34.1598	-106.9096	4639.7	1.4	979674.79	-203.7751
1.484	979188.12	34.1587	-106.914	4672.7	1.4	979674.70	-204.9136
1.485	979185.29	34.157	-106.9188	4707.2	1.3	979674.56	-205.6319
1.486	979182.34	34.1562	-106.9226	4749.7	1.4	979674.49	-205.8658
1.487	979179.85	34.1543	-106.9262	4787.6	1.3	979674.33	-206.0234
1.488	979177.24	34.1532	-106.9301	4828.6	1.3	979674.24	-206.0821
1.489	979174.94	34.1524	-106.9347	4874.8	1.3	979674.17	-205.5440
1.490	979198.63	34.1296	-106.8702	4690.0	1.2	979672.27	-191.1393
1.491	979186.34	34.1367	-106.87	4874.0	1.1	979672.86	-193.0774
1.492	979195.44	34.1439	-106.8701	4752.0	1.1	979673.46	-191.8978
1.493	979186.62	34.137	-106.8529	4872.0	0.9	979672.89	-193.1425
1.494	979179.49	34.1439	-106.8437	5007.0	0.8	979673.46	-192.8529
1.495	979183.62	34.1439	-106.8353	4963.0	0.8	979673.46	-191.3620
1.496	979176.02	34.1513	-106.8175	5161.0	0.6	979674.08	-187.9056
1.497	979181.65	34.1584	-106.8001	5130.0	0.6	979674.68	-184.7296
1.498	979182.12	34.1727	-106.8002	5127.3	0.6	979675.87	-185.6073
1.499	979187.00	34.2334	-106.7968	5111.0	0.7	979680.96	-186.7537
1.500	979184.46	34.2347	-106.8178	5112.0	0.7	979681.07	-189.3427
1.501	979188.03	34.233	-106.8239	5080.0	0.7	979680.93	-187.5495
1.502	979188.59	34.231	-106.8352	5090.0	0.8	979680.76	-186.1220
1.503	979178.17	34.2324	-106.827	5208.0	0.7	979680.88	-189.6818
1.504	979196.19	34.234	-106.8548	4962.0	0.9	979681.01	-186.3510
1.505	979211.68	34.244	-106.8727	4698.0	1.5	979681.85	-186.9241
1.506	979190.00	34.2069	-106.8181	4980.0	0.7	979678.74	-189.3898
1.507	979173.28	34.4234	-106.5178	5732.0	0.5	979696.91	-179.3259
1.508	979160.42	34.4215	-106.5115	5939.0	0.0	979696.75	-180.1103
1.510	979157.59	34.4156	-106.5123	5984.0	0.0	979696.26	-179.7453
1.511	979175.25	34.4263	-106.5186	5705.0	0.0	979697.16	-179.7191
1.522	979180.62	34.042	-106.8483	4721.0	0.9	979661.94	-200.2511
1.523	979175.74	34.0566	-106.818	4958.0	0.8	979666.16	-192.2367
1.524	979180.06	34.0566	-106.801	4985.0	0.7	979666.16	-186.3972
1.525	979181.76	34.0273	-106.848	4667.0	0.9	979663.71	-201.1211
1.526	979169.51	34.0275	-106.8182	4994.0	0.8	979663.72	-193.8743
1.527	979167.31	34.042	-106.7837	5147.0	0.6	979664.94	-188.3096
1.528	979176.88	34.042	-106.8006	4977.0	1.3	979664.94	-188.2362
1.529	979178.94	34.071	-106.8178	4997.0	0.7	979667.36	-188.0018
1.530	979171.06	34.071	-106.8003	5154.0	0.7	979667.36	-186.4650
1.531	979178.38	34.0218	-106.8531	4692.0	1.0	979663.25	-202.4418
1.532	979178.22	34.0218	-106.8481	4702.0	1.0	979663.25	-201.0020
1.533	979181.57	34.0218	-106.8577	4631.0	1.1	979663.25	-202.8606
1.534	979181.46	34.0148	-106.8508	4635.0	1.1	979662.66	-202.1456

Station #	Observed	Lat N	Long W	Elevation	Terr	Theoretical	Anomaly
1.535	979178.76	34.0076	-106.8596	4642.0	1.1	979662.06	-203.7140
1.543	979175.35	34.0608	-106.9228	4777.7	1.5	979666.51	-203.0923
1.544	979177.32	34.0655	-106.9222	4751.2	1.5	979666.90	-202.9249
1.545	979178.73	34.069	-106.9217	4740.8	1.5	979667.19	-202.6114
1.546	979178.73	34.0693	-106.9271	4764.9	1.6	979667.22	-201.0910
1.547	979180.41	34.069	-106.9314	4775.2	1.8	979667.19	-198.5681
1.548	979180.13	34.0693	-106.937	4851.0	2.2	979667.22	-193.9267
1.549	979179.01	34.0712	-106.9421	4955.3	2.5	979667.38	-188.6497
1.550	979172.25	34.0743	-106.9447	5087.1	3.2	979667.64	-187.0637
1.553	979175.91	34.0658	-106.9398	4955.4	2.5	979666.93	-191.2921
1.554	979175.35	34.0624	-106.9404	4952.0	2.6	979666.64	-194.6716
1.555	979174.97	34.058	-106.9388	4914.5	2.5	979666.27	-194.0329
1.557	979071.54	34.0553	-107.1112	6437.2	2.0	979666.05	-206.4056
1.558	979068.07	34.0553	-107.1155	6516.3	2.2	979666.05	-204.9311
1.559	979065.16	34.057	-107.1195	6570.1	2.3	979666.19	-204.6564
1.560	979065.34	34.059	-107.1221	6568.0	2.3	979666.36	-204.7696
1.561	979065.91	34.062	-107.1241	6563.5	2.4	979666.61	-204.6204
1.562	979065.25	34.0649	-107.1254	6587.9	2.4	979666.85	-204.0594
1.563	979066.10	34.068	-107.1268	6583.6	2.4	979667.11	-203.7266
1.564	979064.69	34.0704	-107.1303	6631.0	2.4	979667.31	-202.4943
1.565	979062.44	34.0723	-107.134	6663.9	2.5	979667.47	-202.8299
1.566	979060.09	34.0732	-107.1372	6700.5	2.7	979667.55	-202.8599
1.567	979059.24	34.0748	-107.1397	6702.9	2.9	979667.68	-203.4998
1.568	979059.53	34.0784	-107.1417	6718.5	3.0	979667.98	-202.4753
1.569	979059.06	34.0806	-107.1449	6747.3	3.4	979668.16	-201.0019
1.570	979063.09	34.0806	-107.1398	6658.5	2.7	979668.16	-202.9981
1.571	979067.60	34.0825	-107.1374	6575.8	2.6	979668.32	-203.7074
1.572	979071.82	34.0861	-107.1366	6494.8	2.4	979668.63	-204.8470
1.573	979075.48	34.0891	-107.1364	6431.9	2.4	979668.88	-205.2107
1.574	979080.55	34.0935	-107.1369	6348.9	2.3	979669.24	-205.5872
1.575	979084.49	34.096	-107.136	6271.6	2.2	979669.45	-206.5928
1.576	979087.59	34.0987	-107.1331	6195.9	2.1	979669.68	-208.3592
1.577	979118.73	34.0349	-106.9833	5690.4	1.2	979664.34	-203.1029
1.578	979120.89	34.0346	-106.988	5653.6	1.2	979664.32	-203.1251
1.579	979121.73	34.0344	-106.9937	5634.2	1.2	979664.30	-203.4320
1.580	979121.92	34.0346	-107.0007	5641.2	1.1	979664.32	-204.5583
1.586	979132.15	34.0332	-106.9672	5504.9	1.5	979664.20	-200.3670
1.587	979127.46	34.0338	-106.97	5567.5	1.4	979664.25	-201.4525
1.588	979122.39	34.033	-106.9731	5643.0	1.3	979664.18	-202.0271
1.589	979117.70	34.0338	-106.9767	5709.1	1.3	979664.25	-202.8193
1.590	979116.19	34.0346	-106.9786	5732.5	1.3	979664.32	-202.9926
1.591	979053.24	34.0789	-107.1493	6824.6	3.7	979668.02	-201.7432
1.592	979046.02	34.0778	-107.1532	6922.5	4.0	979667.93	-202.6992
1.593	979041.61	34.0773	-107.1559	6982.8	4.3	979667.89	-203.1505
1.594	979038.79	34.0762	-107.1587	7053.4	4.7	979667.80	-201.2439
1.595	979029.03	34.0745	-107.1625	7161.9	5.3	979667.65	-203.7539
1.606	979192.90	34.3504	-106.7368	5236.0	0.3	979690.78	-183.5229
1.607	979194.46	34.3556	-106.7338	5238.0	0.0	979691.21	-182.5797
1.638	979117.72	34.113	-107.0031	5926.8	2.3	979670.88	-195.3666
2.001	979181.28	34.0738	-106.9383	4753.3	2.3	979667.60	-198.9132

Station #	Observed	Lat N	Long W	Elevation	Terr	Theoretical	Anomaly
2.021	979181.00	34.0728	-106.9335	4782.3	1.9	979667.51	-196.7701
2.031	979182.09	34.0723	-106.9308	4757.3	1.8	979667.47	-198.2378
2.041	979181.65	34.0715	-106.9282	4741.4	1.7	979667.40	-199.6645
2.049	979182.09	34.0713	-106.942	4719.7	2.7	979667.39	-199.5094
2.050	979182.18	34.0713	-106.9447	4718.4	2.6	979667.39	-199.5974
2.051	979182.17	34.0712	-106.9256	4715.4	1.6	979667.38	-200.7789
2.061	979182.34	34.0706	-106.9231	4698.2	1.6	979667.33	-201.5904
2.071	979182.51	34.0701	-106.9205	4683.7	1.5	979667.29	-202.3483
2.081	979183.01	34.0695	-106.918	4670.4	1.5	979667.24	-202.5958
2.091	979183.32	34.069	-106.9156	4662.2	1.4	979667.19	-202.8359
2.101	979183.67	34.0684	-106.913	4651.5	1.4	979667.14	-203.0775
2.106	979174.20	34.0562	-106.9218	4784.9	1.4	979666.12	-203.5258
2.108	979172.70	34.0255	-106.8952	4759.6	1.3	979663.56	-204.1265
2.109	979186.14	34.0659	-106.9035	4621.3	1.3	979666.94	-202.3097
2.110	979187.61	34.0612	-106.8904	4600.7	1.3	979666.54	-201.7322
2.111	979188.08	34.0572	-106.889	4593.1	1.3	979666.21	-201.3836
2.112	979189.29	34.0583	-106.8826	4595.4	1.2	979666.30	-200.2376
2.114	979171.08	34.04	-106.9109	4703.2	1.3	979664.77	-210.3415
2.115	979166.68	34.0255	-106.9202	4898.0	1.2	979663.56	-201.8952
2.116	979160.34	34.018	-106.9281	4988.9	1.2	979662.93	-202.2061
2.120	979191.72	34.0691	-106.8851	4589.4	1.3	979667.20	-198.9608
2.121	979186.80	34.0421	-106.8806	4584.3	1.2	979664.95	-201.9787
2.122	979184.73	34.0247	-106.8785	4575.5	1.2	979663.49	-203.1219
2.123	979182.61	34.0087	-106.8775	4572.8	1.3	979662.15	-204.0165
2.124	979181.07	33.9933	-106.8762	4567.8	1.3	979660.87	-204.5696
2.125	979179.21	33.9788	-106.8744	4570.0	1.3	979659.65	-205.0862
2.126	979175.35	33.9344	-106.8714	4548.3	1.1	979655.95	-206.6900
2.127	979173.18	33.9239	-106.8659	4557.9	1.1	979655.07	-207.4077
2.130	979185.64	34.1213	-106.8452	4884.0	0.9	979671.57	-192.1384
2.131	979174.97	34.1343	-106.8112	5194.0	0.7	979672.66	-185.4529
2.132	979182.17	34.1689	-106.8727	5124.0	0.5	979675.56	-185.5489
2.133	979160.73	33.8859	-106.6949	5099.3	0.4	979651.90	-184.9135
2.134	979157.18	33.8871	-106.686	5060.8	0.3	979652.00	-190.9728
2.135	979155.05	33.8888	-106.6696	5007.0	0.3	979652.14	-196.4716
2.136	979151.18	33.8909	-106.6532	5012.7	0.3	979652.31	-200.1666
2.137	979149.95	33.892	-106.6401	5012.0	0.3	979652.41	-201.5387
2.138	979148.76	33.8945	-106.6237	5028.0	0.3	979652.62	-201.9776
2.139	979152.32	33.881	-106.6077	4983.0	0.3	979651.49	-199.9904
2.140	979176.01	34.1675	-106.9517	5107.0	1.5	979675.44	-191.6113
2.141	979142.54	34.0042	-106.981	5359.4	1.0	979661.78	-196.7802
2.142	979133.29	34.0145	-106.9963	5504.0	1.1	979662.64	-198.1179
2.143	979144.03	34.0058	-106.9743	5343.7	1.0	979661.91	-196.3656
2.144	979148.29	34.0038	-106.9559	5230.6	1.0	979661.74	-198.7222
2.145	979152.55	34.0062	-106.9513	5165.0	1.0	979661.94	-198.5975
2.146	979154.23	34.0463	-106.953	5219.0	1.5	979665.30	-196.5306
2.147	979150.37	34.0439	-106.954	5266.0	1.5	979665.10	-197.3709
2.149	979191.22	34.0619	-106.8771	4590.7	1.2	979666.60	-198.8806
2.154	979192.42	34.066	-106.8753	4592.1	1.2	979666.94	-197.9395
2.158	979193.86	34.0707	-106.8735	4592.2	1.2	979667.34	-199.8866
2.165	979195.07	34.074	-106.8727	4596.1	1.2	979667.61	-195.7188

Station #	Observed	Lat N	Long W	Elevation	Terr	Theoretical	Anomaly
2.168	979196.41	34.0806	-106.8726	4597.8	1.1	979668.16	-194.8789
2.174	979196.43	34.0837	-106.8748	4599.1	1.1	979668.42	-195.0403
2.180	979196.58	34.0871	-106.8775	4601.0	1.1	979668.71	-195.0608
2.186	979196.67	34.0906	-106.88	4603.4	1.2	979669.00	-195.0196
2.190	979197.36	34.0955	-106.8821	4605.0	1.2	979669.41	-194.6437
2.196	979191.94	34.0989	-106.883	4605.4	1.2	979669.70	-194.3242
2.201	979198.51	34.102	-106.8841	4606.1	1.2	979669.96	-193.9716
2.206	979198.89	34.1064	-106.8858	4608.0	1.2	979670.30	-193.8207
2.207	979199.22	34.1094	-106.8868	4609.5	1.3	979670.57	-193.5769
2.215	979199.04	34.1131	-106.8879	4611.4	1.3	979670.88	-193.9526
2.228	979198.87	34.1173	-106.8897	4610.6	1.4	979671.24	-194.4722
2.231	979197.72	34.113	-106.8901	4613.4	1.4	979670.88	-194.0943
2.232	979125.52	34.0174	-107.003	5579.1	1.1	979662.88	-201.6258
2.233	979120.95	34.0213	-107.0099	5626.6	1.1	979663.21	-203.6727
2.234	979087.81	34.0385	-107.0496	6086.3	1.1	979664.64	-210.6778
2.235	979088.62	34.0596	-107.064	6068.7	1.0	979666.41	-212.7878
2.236	979086.93	34.0783	-107.08	6089.1	1.0	979667.97	-214.8183
2.237	979092.46	34.0984	-107.0984	5987.4	1.1	979669.65	-216.9700
2.238	979093.90	34.1071	-107.1166	5969.5	1.3	979670.38	-217.1317
2.239	979095.74	34.1183	-107.142	6040.6	1.7	979671.32	-211.5645
2.240	979096.09	34.1296	-107.1622	6101.1	2.1	979672.27	-208.1316
2.241	979091.40	34.1384	-107.1866	6281.4	1.9	979673.00	-202.9439
2.242	979075.87	34.1284	-107.2082	6440.0	1.9	979672.17	-208.1239
2.243	979064.72	34.1167	-107.2442	6573.4	1.1	979671.19	-211.0932
2.249	979161.32	33.8855	-106.6965	5103.6	0.0	979651.87	-184.4022
2.250	979159.88	33.8742	-106.6975	5117.5	0.0	979650.92	-184.0559
2.251	979158.00	33.8594	-106.6994	5182.9	0.5	979649.69	-180.3189
2.252	979157.70	33.8558	-106.6828	5097.8	0.4	979649.39	-185.5229
2.253	979160.48	33.8454	-106.6701	5014.3	0.5	979648.52	-186.7841
2.254	979160.30	33.8336	-106.6601	4988.5	0.5	979647.54	-187.5278
2.256	979160.69	33.9061	-106.5205	5020.1	0.4	979653.58	-191.3893
2.264	979171.31	33.8619	-106.8752	4522.7	1.1	979649.90	-206.2661
2.265	979173.59	33.8457	-106.8791	4516.2	1.1	979648.55	-203.0252
2.266	979176.66	33.828	-106.8836	4515.0	1.0	979647.07	-198.6016
2.267	979180.26	33.8101	-106.8875	4508.6	0.0	979645.58	-194.8936
2.268	979180.34	33.7959	-106.895	4512.6	0.0	979644.40	-193.3904
2.269	979180.62	33.7845	-106.9023	4504.9	0.0	979643.45	-192.6226
2.270	979178.78	33.7718	-106.9058	4528.9	0.0	979642.39	-191.9652
2.271	979173.81	33.7618	-106.9182	4583.1	0.0	979641.56	-192.8515
2.272	979173.19	33.754	-106.9346	4610.1	0.0	979640.91	-191.2025
2.275	979211.15	34.4043	-106.8609	4760.0	0.0	979695.31	-198.6512